
**Pump-probe measurements of reaction
centers from *Rhodobacter sphaeroides*:
Towards the XXI century.**

Pablo Nahuel Dominguez



Munich 2014

**Pump-probe measurements of reaction
centers from *Rhodobacter sphaeroides*:
Towards the XXI century.**

Pablo Nahuel Dominguez

Dissertation

an der Fakultät für Physik
der Ludwig-Maximilians-Universität
München

vorgelegt von
Pablo Nahuel Dominguez
aus Mar del Plata.

München, den 6. May 2014

Erstgutachter: Prof. Dr. Wolfgang Zinth
Zweitgutachter: Prof. Dr. Josef Wachtveitl
Tag der mündlichen Prüfung: 28.07.2014

Abstract

In this thesis important reactions in the photosynthetic cycle of purple bacteria at room temperature are discussed. In particular, this study is focused on reaction centers from *Rhodobacter sphaeroides* where the primary conversion from light to chemical energy occurs. Namely, an electron is transferred from the initially excited special pair (P) via the bacteriochlorophyll (B) and bacteriopheophytin (H) to the ubiquinone (Q). The underlying kinetics evolve in the time scale from pico- to nanosecond ($1 \cdot 10^{-12}$ s - $1 \cdot 10^{-9}$ s) and can be examined using optical pump-probe experiments.

Accurate measurements performed by Holzapfel et al. in the 1990ies, using 10 Hz excitation rate, suggested that the electron transfer can be described by a stepwise rate model with four intermediate steps within a non-adiabatic electron transfer theory. Moreover, quantum chemical simulations of stepwise electron transfer models were able to describe the high quantum yield ($> 95\%$) of the reaction. In particular, the lifetime of the second intermediate state (1 ps) is shorter than the lifetime of the first intermediate state (3.5 ps).

Recently, experiments using modern laser systems with repetition rates of 1 kHz and above improved the accuracy of the measurements with contradicting results. Combined with new fitting algorithms using singular value decomposition and target analysis, some authors proposed reaction schemes beyond the simple step-wise model. Therefore the question about the primary reaction steps in photosynthesis is still open.

In this thesis a pump-probe experiment was built with high sensitivity in the near infrared spectral region. By performing experiments with high accuracy at low excitation rate and low excitation energy it was possible to confirm the reaction model proposed by Holzapfel et al. with four intermediate steps for times larger than 0.3 ps. The obtained time constants were 1.2 ± 0.3 ps, 3.5 ± 0.2 ps, 220 ± 20 ps together with a long-lasting component, in good agreement with previous publications. Moreover, measurements performed at higher excitation rate displayed significant deviations which can be attributed to the high exhaustion of the sample. In this case two new time constants were observed in the 10 ps and 1 ns range. In this context we showed that these kinetics result from non-physiological illumination conditions and do not play a significant role in the primary reactions of photosynthesis under natural conditions.

Kurzfassung

In dieser Arbeit werden wichtige Reaktionen des photosynthetischen Zyklus von Purpurbakterien bei Raumtemperatur diskutiert. Diese Studie konzentriert sich auf Reaktionszentren von *Rhodobacter sphaeroides* und die Primärkonversion von Licht in chemische Energie. Bei dieser Reaktion wird ein Elektron vom ursprünglich angeregten special pair (P) über ein Bakteriochlorophyll (B) und ein Bakteriophäophytin (H) zum Ubichinon (Q) übertragen. Die zugrundeliegenden Kinetiken laufen auf der Zeitskala von Piko- zu Nanosekunden ($1 \cdot 10^{-12}$ s - $1 \cdot 10^{-9}$ s) ab und können durch optischen Anrege/Abtastexperimente (engl. Pump-Probe) untersucht werden.

Exakte Messungen von Holzapfel et al. in den 1990ern mit einer Anregungsrate von 10 Hz hatten angedeutet, dass der Elektrontransfer (ET) durch ein stufenweises Ratenmodell mit vier Zwischenzuständen, im Rahmen einer nichtadiabatischen ET-theorie, beschrieben werden kann. Zusätzlich konnten quantenchemische Simulationen von stufenweisen ET-modellen die hohe Quantenausbeute der Reaktion (> 95 %) erklären. Insbesondere zeigte sich dabei, dass die Lebensdauer des zweiten Zwischenzustands (1 ps) kleiner ist als die des ersten angeregten Zustands (3.5 ps).

Vor kurzem wurden Messungen mit höherer Auflösung veröffentlicht, die mit modernen Lasersystemen und höheren Repetitionsraten (> 1 kHz) gemessen wurden. Zusammen mit neuen Auswertungsalgorithmen, die auf Singulärwertzerlegung mit Targetanalyse basieren, wurden von mehreren Autoren widersprüchliche Reaktionsschemen vorgeschlagen, die wesentlich vom einfachen Stufenmodell abweichen. Deshalb war die Frage nach den primären Reaktionsschritten in der Photosynthese wieder offen.

In dieser Arbeit wurde ein Anrege/Abtastexperiment mit hoher Sensitivität im nahinfraroten Spektralbereich entwickelt. Messungen mit hoher Auflösung bei niedriger Anregungsrate und niedriger Anregungsenergie haben das Reaktionsmodell mit vier Zwischenzuständen von Holzapfel et al. bestätigt. Die dadurch erhaltenen Zeitkonstanten, 1.2 ± 0.3 ps, 3.5 ± 0.2 ps, 220 ± 20 ps und eine langlebige Komponente, stimmen mit diesen vorherigen Publikationen überein und widersprechen einer Reihe von kürzlich veröffentlichten Daten. In diesem Zusammenhang zeigten Messungen mit höheren Anregungsraten deutliche Abweichungen, die auf eine höhere Belastung der Probe zurückzuführen sind. In diesem Fall treten zwei neue Zeitkonstanten im Bereich von 10 ps und 1 ns auf. Schließlich wurde gezeigt, dass die neuen Kinetiken aus nichtphysiologischen Belichtungsbedingungen resultieren und bei natürlichen Bedingungen irrelevant für die Primärreaktionen der Photosynthese sind.

Contents

Abstract	v
Kurzfassung	vii
1 Introduction	1
2 Theoretical background	5
2.1 Spectroscopy	5
2.1.1 Pump-probe techniques	6
2.1.2 Coherence and time zero artifacts	8
2.1.3 Time resolution	10
2.1.4 Empirical instrument response function	11
2.2 Linear optics	12
2.3 Non-linear optics	13
2.3.1 Two wave mixing	13
2.3.2 Non-collinear geometry	15
2.4 Dichroism	16
2.5 Rate models	17
2.5.1 Definition of the rate system for reaction centers	17
2.6 Singular value decomposition (SVD)	20
2.6.1 SVD-Filter	20
2.6.2 Number of significant singular values	21
2.7 Electron transfer theory	24
2.7.1 Non-adiabaticity	24
2.7.2 Marcus theory	26
2.7.3 Application to reaction centers	27
2.8 Fit algorithms and data analysis	28
2.8.1 Target analysis	29
2.8.2 Single value decomposition and target analysis	29
2.8.3 Consistency analysis for the target model	31
3 The photosynthetic purple bacteria <i>Rhodobacter sphaeroides</i>	35
3.1 The basic principles: light absorption and energy storage	35
3.2 Structure of the reaction center	38

3.3	Photochemical reaction and electron transfer	41
3.3.1	Chronology 1970-1990	41
3.3.2	Chronology 1990-2013	43
3.4	Recombination processes and chemical modification	50
3.5	Final remarks and status quo	52
4	Experimental set-up	53
4.1	Sample preparation	53
4.2	Pump-probe setup	55
4.2.1	Excitation pulse	57
4.2.2	Probe pulse	61
4.2.3	Sample focusing and stirring elements	62
4.2.4	Chopper and shutter	65
4.2.5	Spectrometer and detection	66
4.3	Software for measurement and data analysis	68
4.3.1	Acquisition software	68
4.3.2	Analysis software	69
4.4	Measurement specifications	70
5	Results and Discussion	71
5.1	Calibration dye IR132	71
5.2	Reaction centers	73
5.2.1	Measurements at 50 Hz	73
5.2.2	Measurements at 500 Hz	82
5.2.3	Measurements at 500 Hz with reducing agents	88
5.3	Final remarks and conclusions	94
6	Summary	97
7	Zusammenfassung	99
	List of Figures	103
	List of Tables	107
	Bibliography	109
	Lebenslauf	121

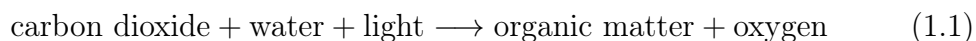
1 Introduction

The important role of photosynthesis for all living organisms influenced the lifestyle of mankind since antique ages. Using the irradiated energy available in the earth surface it is possible for many species to store electromagnetic energy into biologically suitable units. In our case, as human beings, we can mostly make an indirect use of the sunlight-energy. It is not surprising, for example, that improving the utilization of sunlight motivated most of the original nomadic civilizations to become sedentary and apply farming techniques. This optimization process is still present in our society, and many scientific disciplines are still gathering their knowledge by studying this ancient research topic.

The first reported examination of photosynthesis applying scientific methods was given by **van Helmont** (1640). His experiment consisted in planting a tree in a huge tub with earth and measuring the weight of plant and tub. He observed that the weight of the tree does not come from soil and (miss-)interpreted this result affirming that the tree mass should come from the applied water (for references see [Bla02]).

Many further investigations from **Joseph Priestley** (1771), **Jan Ingenhouz** (1779) and **Senebier** (1783) discovered the role of oxygen, carbon dioxide and sunlight in the growth process of a plant.

Finally was **De Saussure** (1804) who summarized the previous results and wrote the reaction equation of photosynthesis:



Even if equation (1.1) is more than 200 years old, the microscopic processes which lead to such a relation are still not fully known. In this thesis we will concentrate on the photosynthesis of bacterial organisms, which can be considered as a prototype reaction. The considered purple bacterium *Rhodobacter sphaeroides* has one of the best studied photosynthetic system.

The corner stone of every photosynthetic unit is the *reaction center*. This large protein complex is responsible for the primary conversion from light to chemical energy by generating a difference in electric potential between the two sides of an inner cell membrane. In particular, a photo-induced electron transfer, carried out by a series of electron acceptor-donor molecules, creates a product which stores part of the incoming energy. In secondary processes the stored energy is fixed by proton transfer reactions. The electron transfer evolves in the picosecond time

range ($1 \text{ ps} = 1 \cdot 10^{-12} \text{ s}$) and has very low recombination losses with a transport yield of almost 1.

One of the key problems of photosynthesis consists in producing an efficient and irreversible electron transfer in a short distance using only a few number of transfer molecules. This issue captured the attention of many distinguishable scientists, in particular from the theoretical chemist and (current) nobel prize winner in chemistry 2013, **Arie Warshel**.

Precise experimental information became available after the improvement of femtosecond technologies. In this context, colliding pulse modelocked (CPM) and Titanium-Sapphire laser systems had an important role. Measurements performed by Holzappel et al. [Hol89] in the 1990ies had the necessary time resolution, together with a high signal-to-noise ratio, to provide evidence of a simple stepwise reaction model. Namely, an electron is transferred from the photoexcited special pair P^* through the accessory bacteriochlorophyll B_A and bacteriopheophytin H_A to the ubiquinone Q_A .

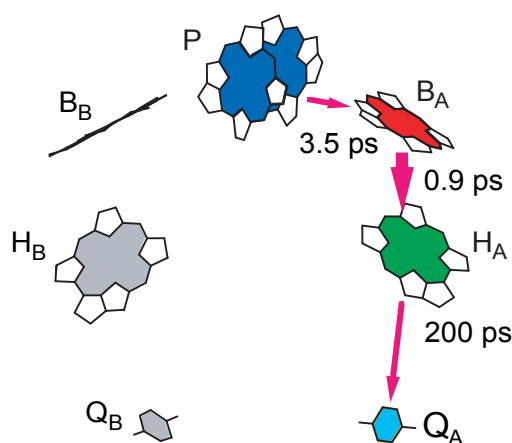


Figure 1.1: Sequential reaction scheme with four charge transfer states. The short lifetime of the accessory bacteriochlorophyll B_A avoids recombination losses.

Detailed simulations using evolutionary optimization algorithms have shown recently that this simple reaction scheme is able to explain the high quantum yield $\eta > 95\%$ and the good energy efficiency of the primary photosynthetic reaction [FZV08]. However new publications [Kak10, Zhu13] appeared recently with several discrepancies which cannot be explained within the scheme in figure 1.1. At this point, many alternative reaction principles were proposed and the fundamental question about the mechanisms of the primary reactions in photosynthetic reaction centers was reopened. In particular, the similar discussion given in the 1980ies motivated the idea that the improved experimental data "will allow theoreticians

to modify existing ideas and to develop new ones about how photosynthetic organisms so efficiently bring about the fastest biomolecular reactions known in photochemistry" [Bar88].

Goal of this thesis is to set up an experiment capable to repeat the measurement on reaction centers from *Rhodobacter sphaeroides* under different experimental conditions with the best precision available. This will allow us to address again the question regarding the validity of a stepwise sequential model under physiological conditions.

The chronological evolution of this project can be divided into four phases, each of them leading to important results:

The *first phase* consisted in the construction and calibration of an optical pump-probe experiment in the visible and near-infrared. A major effort was made to effectively use non-linear effects to produce a reliable excitation pulse at 865 nm. Meanwhile, it was also necessary to produce a probe beam over the full visible spectral range even for the region near the laser fundamental wavelength.

The *second phase* consisted in the first measurements of the reaction centers using the maximal repetition rate available of 500 Hz. Difficulties due to the low amount of sample available had to be overcome to avoid systematic errors, caused by the accumulation of the molecules in a product state.

The *third phase* consisted in measuring the reaction centers at 500 Hz with addition of reducing chemicals, like sodium-ascorbate and ortho-phenanthroline. In this way it was possible to improve the experimental conditions, thus rising the signal-to-noise ratio of the measurement.

The *fourth phase* consisted in measuring the reaction centers with a reduced excitation rate of 50 Hz. A larger time interval between two excitation pulses allows the molecules to relax to the ground state, avoiding accumulation effects. These correspond to the currently best experimental conditions available, which are similar to the irradiation properties present in nature.

2 Theoretical background

In this chapter all necessary physical and mathematical concepts will be discussed. These are available in the literature, with exception of section 2.8.3, and will be only presented shortly.

2.1 Spectroscopy

A photon traveling through a medium can generate a transition to an excited state, a process which is commonly named *absorption*. On the other hand a present excited state may decay by generating a photon; this process is called *emission*. The probability of such processes may vary with the configuration of the composing atoms (molecules) and with the energy of the photon. The comprehensive analysis of those events is referred to as (*light-*) *spectroscopy*, giving detailed information on their microscopic origin.

The intensity of a monochromatic wave with wavelength λ which propagates through an unsaturated material of length L can be expressed as [ZZ11]:

$$I(\lambda) = I_0 \cdot 10^{-\varepsilon(\lambda) \cdot C \cdot L} \quad (2.1)$$

The quantity C is the concentration of the sample contributing to the process and $\varepsilon(\lambda)$ is the *extinction coefficient* which characterizes its optical properties. The transmission coefficient of the sample is given by $T = I/I_0$ and is related to the absorption A in units of *optical density (OD)* as follows:

$$T = 10^{-\varepsilon(\lambda) \cdot C \cdot L} = 10^{-A(\lambda)} \quad (2.2)$$

In particular, the equality between the last two exponents is referred to as *Lambert Beer's law* or linear absorption regime. Briefly, this equation states that the absorption changes are linearly related to the variation of absorbing elements. It is not always valid since the sample saturates when the incoming radiation has many more photons than absorbing molecules. Moreover the formula (2.2) can be expressed using the *absorption cross-section* σ and the number of molecules per volume N .

$$A(\lambda) = \frac{1}{\log 10} \sigma(\lambda) \cdot N \cdot L \quad (2.3)$$

We can now discuss the experimental methods which are currently used to analyze static and dynamical properties of a given molecular system. Two main types of spectra are considered in this thesis:

- *continuous wave (CW)-spectrum*: contains information on equilibrium (ground state) properties. It is measured by continuously sending photons at low intensities. Since the dynamical processes are very fast (1 fs - 100 μ s), the averaged signal displays mostly the absorption of unexcited molecules.
- *broad band time resolved spectrum*: contains information on non-equilibrium properties at many different wavelengths measured at the same time. It can be performed using a laser pulse with short duration and large spectral broadening.

2.1.1 Pump-probe techniques

The experimental technique used in this thesis to measure ultrafast processes is the broad-band time resolved pump-probe spectroscopy (see figure 2.1). This uses two different short laser pulses: a strong *pump* or excitation pulse centered at a fixed excitation wavelength λ_{ex} and a weak *probe* or reference pulse with a very broad spectral shape, which is applied to the sample at a defined probing time. Both beams, derived from the same laser source, are focused in the sample and overlap along the length of the cuvette. When the pump beam is absorbed by the sample, it starts a dynamical process. Afterwards pump-induced changes in the absorption of the sample are registered and transmitted by the probe beam. The detected intensity I_d contains information about the dynamics of the photoexcited molecules. On the other hand, the excitation beam is blocked after leaving the sample and will not be detected. A spectrometer separates the different spectral channels. The detection consists of an electronic photon-detector with a response time much slower than the observed dynamical processes, thus giving an averaged signal. In this case the time resolution is achieved using a mechanical delay stage which varies the delay time Δt between both incoming pulses. Finally, to overcome the systematic errors due to fluctuations of the laser and subsequent components, every second pulse of the excitation beam is blocked and only the ground state transmission I_0 is recorded.

All things considered the detected intensity I_d after excitation depends on the probe field E_t and the component of the generated signal field E_s which propagates in the same direction [Muk95, Wei09]:

$$I_d(t) = \epsilon_0 n(\omega_s) c |E_t(t) + E_s(t)|^2 \quad (2.4)$$

$$= I_t(t) + I_s(t) + 2\epsilon_0 n(\omega_s) c \text{Re}[E_t^*(t) \cdot E_s(t)] \quad (2.5)$$

Moreover, the second term in (2.5) can be omitted when the excitation energies are low.

The computed difference in absorption signal displays the deviation from the ground state (g.s.) properties of the sample:

$$\Delta A(t) = A_{ex}(t) - A_{g.s.} = -\log \frac{I_d(t)}{I_0(t)} \quad (2.6)$$

Main characteristic signatures are:

- *ground state bleaching* (GSB): A negative signal at the excitation band. This reflects the lack of absorbing molecules after photoexcitation.
- *excited state absorption* (ESA): A positive signal, which may appear everywhere in the spectrum. It reflects the new absorption of excited molecules even in spectral regions far away from the excitation.
- *stimulated emission* (SE): A negative signal for wavelengths larger than the excitation. It reflects the emission of photons with lower energy after photoexcitation.
- *absorption of photoproducts*: An absorption signal originated from molecules whose conformation were changed in a previous exposition by the excitation pulse and have not relaxed to the original state. The formation of products can be irreversible (e.g. structural changes) or reversible (e.g. electron transfer) and can lead to accumulation effects.

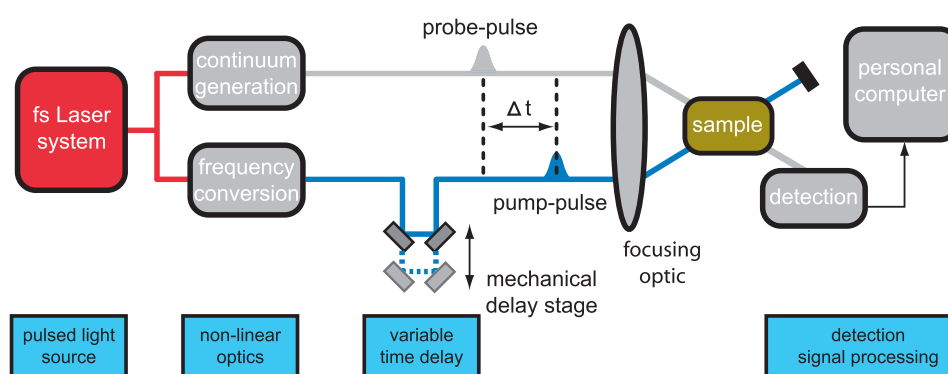


Figure 2.1: Schematic representation of a pump-probe experiment.

2.1.2 Coherence and time zero artifacts

In the following discussion we will combine sections 2.1 and 2.1.1 to explain the disturbing coherent phenomena appearing in the present measurements. Indeed this kind of detection has several undesired effects which overlap with the physical signal originated from the photochemical structural changes in the sample. We begin with the usual expression for the pump (p) and probe (t) fields:

$$E_p(t - \Delta t) = A_p(t - \Delta t) \exp\{i(\mathbf{k}_p \cdot \mathbf{r} - \omega_p(t - \Delta t))\} \quad (2.7)$$

$$E_t(t) = A_t(t) \exp\{i(\mathbf{k}_t \cdot \mathbf{r} - \omega_t t)\} \quad (2.8)$$

If we now define $\alpha(t) = \sigma N(t) \log^{-1}(10)$ as the *attenuation coefficient* of the sample, the electromagnetic field satisfies the following partial differential equation:

$$\frac{\partial E}{\partial z} = -\frac{\alpha}{2} E \quad (2.9)$$

For small absorption it is justified to approximate the solution of (2.9) using only the first order Taylor expansion:

$$E_{out}(t) = E_{in}(t) e^{-\alpha(t)L/2} \simeq E_{in} \left[1 - \alpha(t) \frac{L}{2} \right] \quad (2.10)$$

Changes in the *attenuation coefficient* can be expressed as $\alpha(t) = \alpha_0 + \Delta\alpha(t)$. The absorption change will depend on the intensity of the field $I_{in} \sim |E_t + E_p|^2$ and the impulse response function $h(t)$. If both beams have similar frequencies ($\omega_p \sim \omega_t$), then the same response function for both fields can be assumed.

$$\begin{aligned} \Delta\alpha(t) &= - \int dt' h(t - t') I_{in}(t') \\ &= -\epsilon_0 n(\omega_s) c \int dt' h(t - t') \left[|A_p(t')|^2 + |A_t(t')|^2 + 2 \text{Re}\{A_p^*(t') A_t(t') e^{i(\Delta\mathbf{k} \cdot \mathbf{r} - \Delta\omega t)}\} \right] \end{aligned} \quad (2.11)$$

Next, it is necessary to find an expression for the signal field in (2.5). This can be obtained using (2.10):

$$E_s(t) = -\frac{\alpha(t)L}{2} (E_t(t) + E_p(t - \Delta t)) \quad (2.12)$$

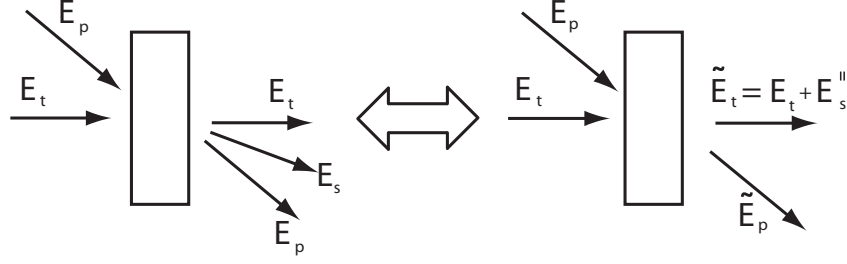


Figure 2.2: Generated signal field after a pump probe experiment. Only the component propagating in the \mathbf{k}_t direction is detected.

Putting everything together, we can compute the average detected intensity $\langle I_d \rangle$ from (2.5):

$$\langle I_d \rangle = \langle I_t \rangle - \alpha_0 \epsilon_0 n(\omega_s) c L \int dt \left(E_t^*(t) E_t(t) + E_t^*(t) E_p(t - \Delta t) \right) \quad (2.13)$$

$$- \epsilon_0 n(\omega_s) c L \int dt \Delta \alpha(t) \left(E_t^*(t) E_t(t) + E_t^*(t) E_p(t - \Delta t) \right) \quad (2.14)$$

The relevant contributions in (2.13) are those where the signal field propagates in the \mathbf{k}_t direction. This is mandatory because only the collimated probe beam is sent to the detection. Neglecting the simultaneous absorption of two probe photons, only three terms are to be considered:

$$\langle I_d \rangle = (1 - \alpha_0 L) \langle I_t \rangle + (\epsilon_0 n(\omega_s) c)^2 L (\gamma(\Delta t) + \beta(\Delta t)) \quad (2.15)$$

where

$$\gamma(\Delta t) = \int \int dt dt' |A_p(t' - \Delta t)|^2 |A_t(t)|^2 h(t - t') \quad (2.16)$$

$$\beta(\Delta t) = \text{Re} \int \int dt dt' A_p^*(t' - \Delta t) A_t(t') A_t^*(t) A_p(t - \Delta t) h(t - t') \quad (2.17)$$

The first term $I_0 = (1 - \alpha_0 L) \langle I_t \rangle$ is nothing else than the transmitted probe intensity recorded without excitation. Thus, the transmission coefficient is easily obtained:

$$T = 1 + \frac{(\epsilon_0 n(\omega_s) c)^2 L}{(1 - \alpha_0 L) \langle I_t \rangle} (\gamma(\Delta t) + \beta(\Delta t)) \quad (2.18)$$

The function $\gamma(t)$ depends only on the intensity of the fields, describing the absorption of the sample even when the pump and probe fields are not coherent. It displays the saturation of the absorption originated by the pump pulse, causing a signal change at early times.

The second function $\beta(t)$ is more complicated. It originates from the coherent coupling between probe and scattered pump in the \mathbf{k}_t direction and is symmetric around time zero (i.e. $\Delta t = 0$). Physically, the coherent coupling vanishes if the pump and probe beams do not have a spectral overlap.

Other more complicated forms of coherent artifacts at time zero were also reported in the literature [Lor02]. These higher order non-linear effects produce undesired signals in most regions of the spectrum.

2.1.3 Time resolution

In current experiments, the involved energies are very small and only the linear response function contributes to the signal. This can be interpreted as a superposition of causal exponential decays with a given amplitude:

$$h_i(t) = a_i \theta(t) e^{-t/\tau_i} \quad (2.19)$$

The symbol $\theta(t)$ represents the *heaviside function*, which is 1 for $t > 0$ and vanishing for $t < 0$. The pump and probe pulses used in the experiment are assumed to have gaussian shape¹ with different widths. The cross-correlation $G(t)$ is defined as the convolution between both field intensities and determines the *cross-correlation time* t_{corr} :

$$G(t) = \int dt' |A_p(t)|^2 |A_t(t' - t)|^2 = e^{-t^2/t_{corr}^2} \quad (2.20)$$

Under this assumption it is possible to explicitly compute (2.16) and (2.17):

$$\gamma_i(\Delta t) = h_i * G(\Delta t) = a_i \pi t_{corr} e^{t_{corr}/4\tau_i^2} e^{-\Delta t/\tau_i} \frac{1 + \operatorname{erf}\left(\frac{\Delta t}{t_{corr}} - \frac{t_{corr}}{2\tau_i}\right)}{2} \quad (2.21)$$

$$\beta_i(\Delta t) = a_i \frac{\pi t_{corr}^2}{4} e^{t_{corr}^2/4\tau_i^2} e^{-\Delta t^2/t_{corr}^2} \sim G(\Delta t) \quad (2.22)$$

where the operator $*$ stands for the convolution between two functions. At this point it is evident that the function $G(t)$ represents an intrinsic property of the experiment, thus it is usually called *instrument response function*. Moreover the *cross-correlation time* t_{corr} is the most important parameter at early times. It

¹The intensity profiles of the light pulses used in this experiment can be fitted using gaussian functions

defines the width of the time zero artifacts and therefore it is a lower bound for the minimal detectable kinetics.

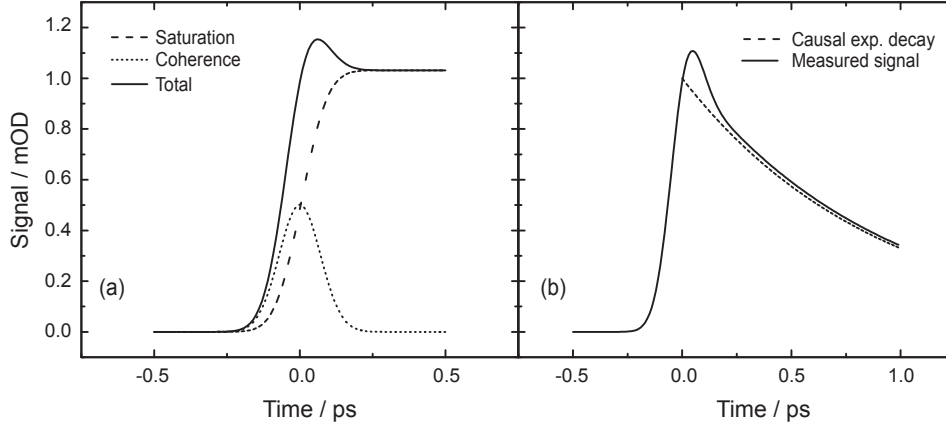


Figure 2.3: Calculated contribution from coherent artifacts in pump-probe signal for $\tau = \infty$ (a) and $\tau = 0.9$ ps (b) within a time resolution $t_{corr} = 100$ fs. The strong deformation of the total signal makes the detection of fast kinetics more difficult.

2.1.4 Empirical instrument response function

To summarize this section, the measured signal of a pure exponential decay using a pump-probe experiment is altered for delay times of order of t_{corr} . The previous computations show that the cross-correlation $G(t)$ can be used, assuming gaussian-shaped pulses, as the instrument response function. In realistic experiments however, the higher order non-linear coupling between pump and probe pulses produces coherent artifacts that are not exclusively gaussian functions. An empirical solution to this deviations can be compensated using higher derivatives of $G(t)$. The resulting empirical fit function is given by:

$$f^{(emp)}(t) = \sum_{k=0}^2 a_k^{gauss} \left(\frac{d}{dt} \right)^k G(t) + \sum_{i=1}^{N_{exp}} (h_i * G)(t) \quad (2.23)$$

or equivalently:

$$f^{(emp)}(t) = a_0^{gauss} G(t) + a_1^{gauss} G'(t) + a_2^{gauss} G''(t) + \sum_{i=1}^{N_{exp}} a_i \gamma_i(t) \quad (2.24)$$

In this case we used up to the 2nd derivative of $G(t)$ to approximate the coherent artifacts at time zero. The quantity N_{exp} indicates the number of exponential functions used in the analysis.

2.2 Linear optics

In this section we will consider an electromagnetic wave propagating in the z -direction for weak intensities. In this case the polarization of the media will be linear on the field, and the Maxwell equation can be written as follows:

$$\frac{\partial^2 \mathbf{E}}{\partial z^2} - (\chi_1 + 1)\epsilon_0\mu_0 \frac{\partial^2 \mathbf{E}}{\partial t^2} = 0 \quad (2.25)$$

The left side of (2.25) corresponds to the wave propagating term together with the first order susceptibility contribution χ_1 . This determines the refraction index $n^2 = (\chi_1 + 1)$ of the material. A general solution can be found in terms of the Fourier transform [ZZ11]:

$$\mathbf{E}(z, t) = \frac{1}{\sqrt{2\pi}} \int_{-\infty}^{\infty} \tilde{\mathbf{E}}(\omega) e^{i(\omega t - k(\omega)z)} d\omega \quad (2.26)$$

The (frequency dependent) wavenumber $k(\omega)$ is dependent on the refraction index $n(\omega)$ and the speed of light in vacuum c :

$$k(\omega) = n(\omega) \frac{\omega}{c} \quad (2.27)$$

If we now consider a light pulse with a spectral distribution centered at ω_0 , it is possible to expand (2.26) using the Taylor series up to second order:

$$\mathbf{E}(z, t) \simeq \frac{e^{i(\omega_0 t - k_0 z)}}{\sqrt{2\pi}} \int_{-\infty}^{\infty} \tilde{\mathbf{E}}(\omega_0 + \Omega) \cdot \exp\left(-iz \frac{\Omega^2}{2} k''(\omega_0)\right) \cdot \exp\left[i\Omega(t - zk'(\omega_0))\right] d\Omega \quad (2.28)$$

The propagation of a single spectral component is given by the *phase velocity* v_{ph} . This can be computed using the zero order contribution:

$$v_{ph} = \frac{\omega_0}{k_0} \quad (2.29)$$

The propagation of the entire wave package is given by the *group velocity*. This can be computed using the first order contribution:

$$v_{gr} = \left(k'(\omega_0)\right)^{-1} = \frac{d\omega}{dk}(\omega_0) = \frac{c}{n(\omega_0)} \quad (2.30)$$

The second derivative of the wave number $k''(\omega_0)$ generates a phase factor in (2.28). This property is called *temporal chirp*. In other words, the spectral components reach a given observation point at different times. If these propagate through a media with normal dispersion, then the blue wavelength components will have smaller phase velocity than the red components. Eventually, these components will be spatially separated from each other and the pulse duration will be increased. The field has a *positive chirp* if the red components propagate at the beginning of the beam, before the blue components. Analogously, the field has a *negative chirp* when the opposite happens. In the experiments it is desirable to use negative chirped pulses before reaching the sample, because the pulse duration will become shorter after traveling through a dispersive material, such as lenses and crystals.

2.3 Non-linear optics

The controlled utilization of non-linear effects has become an indispensable tool in laser physics. When the beam intensities are very high, for example in the case of ultrashort pulses, the polarizability of the medium is not linear in the fields anymore, and new exciting phenomena occur. In the following section, the main characteristics of two wave mixing will be explained.

2.3.1 Two wave mixing

The coupling of two different electromagnetic fields can be achieved using specific materials to generate new components having a wavelength which was not available before. It allows the experimenter to *tune* the beams and therefore change the measurement conditions from experiment to experiment. Even so, the selection of the outgoing fields is done using very few variable parameters. For this reason this process is named *parametric amplification*.

The Maxwell equation for the electromagnetic field in a polarizable medium can be written as [CS03, ZZ11]:

$$\frac{\partial^2 \mathbf{E}}{\partial z^2} - (\chi_1 + 1)\epsilon_0\mu_0 \frac{\partial^2 \mathbf{E}}{\partial t^2} = \mu_0 \frac{\partial^2 \mathbf{P}^{NL}}{\partial t^2} \quad (2.31)$$

The left hand side of (2.31) corresponds to the linear term discussed in section 2.2. On the other hand, the right side defines a new field source caused by the non-linear polarization vector \mathbf{P}^{NL} . This source term can generate new fields whose wavelengths may not have been available previously. The lowest order contribution is determined by the second order susceptibility tensor $\chi^{(2)}$:

$$P_i^{NL} = \epsilon_0 \chi_{ijk}^{(2)} E_j E_k \quad (2.32)$$

Furthermore, the non-linear effects will be stronger when the considered beam has a high intensity. For this reason it is usually better to use short laser pulses which have more power than a continuous wave at the same energy. If a 150 fs pulse with 100 μJ is focused into a spot having 300 μm diameter, the resulting intensity is of order *tera watt per square centimeter* (TW/cm^2).

An incoming signal field E_s , having the desired wavelength, is used to *seed* the process. Furthermore, a very intense *pump* field E_p provides the necessary energy. In the parametric process the seed pulse is amplified at the expense of the pump pulse. In this the amplification process, a new outgoing field E_i called *idler* is present because of energy conservation:

$$\hbar\omega_p = \hbar\omega_s + \hbar\omega_i \quad (2.33)$$

Clearly the pump beam must have a wavelength λ_p shorter than $\lambda_{s/i}$. Moreover the amplification process will be more efficient when the momentum conservation is also satisfied:

$$\hbar\mathbf{k}_p = \hbar\mathbf{k}_s + \hbar\mathbf{k}_i \quad (2.34)$$

The last expression is denoted as *phase matching condition*: $\Delta\mathbf{k} = \mathbf{k}_p - \mathbf{k}_s - \mathbf{k}_i = 0$. For this to be implemented, it is necessary to use a birefringent crystal, in the present case *beta barium borate* (BBO). This material has a crystallographic *optical axis* (*o.a.*) which defines two different directions, corresponding to the *ordinary* and *extraordinary* beams. Each direction has a well defined, but not equal, refractive index n_o and n_e .

The currently used geometry has a seed beam polarized perpendicular to the plane defined by the optical axis and the pump beam. Therefore the seed field has a ordinary refractive index n_{os} , whereas the pump beam has a corresponding quantity $n_{ep}(\theta)$ which can be computed by the following geometrical equation:

$$\frac{1}{n_{ep}^2(\theta)} = \frac{\sin^2(\theta)}{n_{ep}^2} + \frac{\cos^2(\theta)}{n_{op}^2} \quad (2.35)$$

In this case, θ is the angle between the pump field and the optical axis of the crystal. Using this kind of birefringent materials, it is possible to fulfill the phase matching condition using only θ as variable parameter. A Type II phase matching is achieved when the idler propagates in the extraordinary direction. Thus equation (2.34) can be rewritten for the special case of a Type II BBO:

$$n_{ep}(\theta)\omega_p = n_{os}\omega_s + n_{ei}\omega_i \quad (2.36)$$

Analogously, the generated idler field can use the present pump field to do the parametric amplification and generate a seed field. For this reason the amplification process is initially exponential in the crystal length.

2.3.2 Non-collinear geometry

For pump and seed pulses in the visible spectral region propagating in the same direction, the parametric amplification will have a decreased efficiency due to the *group velocity mismatch* (GVM) between these two interacting beams. For long propagation lengths the temporal and spatial overlap will not be guaranteed anymore and the parametric amplification is stopped. Analogously the GVM between seed and idler will broaden the temporal width of the seed beam while limiting the amplification bandwidth.

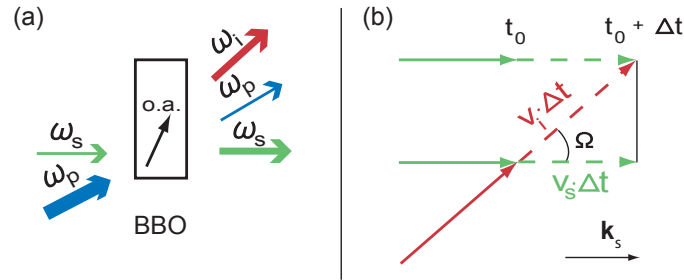


Figure 2.4: Schematic representation of the parametric amplification process (a) and the non-collinear angle Ω necessary to reduce the negative effects of the GVM (b). During the parametric process the pump photons are absorbed and the number of seed photons is increased. In same amount the idler photons are generated. The non-linear crystal BBO has an inclined optical axis (o.a.) to ensure the phase matching condition.

A solution to this dilemma is given by a non-collinear geometry [Hac95, WPR97, Ric00], together with an extended pump beam. The propagation vectors \mathbf{k}_s and \mathbf{k}_i will define an angle Ω . In this case a new condition between the corresponding group velocities v_g must be fulfilled to minimize the GVM-effects:

$$v_{gs} = v_{gi} \cdot \cos(\Omega) \quad (2.37)$$

In other words, the (usually) faster idler beam will have to travel a longer distance than the slower seed beam while propagating with the same velocity in the \mathbf{k}_s direction.

2.4 Dichroism

Polarization analysis is a very important tool for studying structural properties of molecular systems. Many organic and inorganic compounds have a different optical response for each polarization state of the interacting light field. This phenomenon is called *dichroism*.

We consider two different linearly polarized fields for exciting (\mathbf{E}_p) and probing (\mathbf{E}_t) the sample. The detected photochemical signal will depend in a non-trivial way on the angle α between both polarization vectors. Furthermore the measurements are done in the liquid phase where the molecules are randomly oriented. The referenced pump-probe signal provides information about the difference in absorption cross-section $\Delta\sigma_i = \sigma_i - \sigma_0$ for different absorbing states, where σ_0 refers to the ground state of the system. In the specific case of reaction center from *Rhodobacter sphaeroides* these correspond to four different charge transfer states. The averaged absorption cross-section may be computed as described in [Hol]:

$$\Delta\sigma_i(\alpha, \gamma_i, \lambda) = \frac{3}{5} \Delta\bar{\sigma}_i(\lambda) \cos^2 \alpha (1 + 2 \cos^2 \gamma_i(\lambda)) + \frac{3}{5} \Delta\bar{\sigma}_i(\lambda) \sin^2 \alpha (2 - \cos^2 \gamma_i(\lambda)) \quad (2.38)$$

The quantity $\gamma_i(\lambda)$ defines the angle between the primary excited dipole moment and the absorbing dipole moment at the wavelength λ . The value $\Delta\bar{\sigma}_i(\lambda)$ corresponds to the effective cross-section when measuring with completely unpolarized pump and probe fields.

Three main types of dichroic measurements can be identified:

- Parallel measurements ($\alpha = 0^\circ$): The angle between pump and probe is set to zero. The predominant signal corresponds to molecules whose dipole moment is parallel to the excitation.
- Perpendicular measurements ($\alpha = 90^\circ$): Both pump and probe fields are orthogonal. The predominant signal corresponds to molecules whose dipole moment is perpendicular to the excitation.
- Magic angle measurements ($\alpha = 54.73^\circ$): In this case, all polarization effects vanish ($\cos^2 \alpha = \frac{1}{3}$). The measured signal corresponds to $\Delta\bar{\sigma}_i(\lambda)$, independently from the orientation of the absorbing dipole moments.

A simple test can be performed to verify the integrity of the dichroic measurements. At the excitation wavelength λ_{ex} , the signal of all charge transfer states comes from the primary excited dipole moment, in this case from the *special pair*. Therefore, within this absorption band, all present states have a relative angle

$\gamma_i = 0$. In this case more photons will be absorbed if the dipole moment is aligned parallel to the pump field. By setting this in (2.38) we conclude that the measured signal at the excitation wavelength λ_{ex} should satisfy:

$$\frac{\Delta A^{\parallel}(\lambda_{ex})}{\Delta A^{\perp}(\lambda_{ex})} = \frac{\sum_i 3\Delta\bar{\sigma}_i(\lambda)N_i(t)}{\sum_i \Delta\bar{\sigma}_i(\lambda)N_i(t)} = 3 \quad (2.39)$$

Using parallel and perpendicular configurations it is possible to reconstruct the dichroic properties of the sample. Special attention should be given to use the correct quantity for this propose, namely the difference in absorption cross-section $\Delta\sigma_i$. They are not proportional to the measured ΔA if more than one transition is present in the considered absorption band. A possible method for their computation is given in section 2.5. At his point, the dichroic angles can be computed using the quotient between both absorption cross-sections:

$$\cos^2(\gamma_i) = \frac{2s_i - 1}{s_i + 2}, \quad s_i := \frac{\Delta\sigma_i^{\parallel}}{\Delta\sigma_i^{\perp}} \quad (2.40)$$

2.5 Rate models

Rate models are used to describe transitions between a finite number of molecular states while neglecting quantum mechanical effects. This is not always the best method to solve the physical problem, because quantum states cannot generically be treated as a finite set of discrete vectors. Moreover, coherent effects cannot be simulated using rate equations. In the specific case of non-adiabatic electron transfer, this analysis is appropriate because there is only a finite number of acceptor cofactors and their mixed states play no role in the transfer mechanism (see section 2.7).

2.5.1 Definition of the rate system for reaction centers

In reaction centers of purple bacteria there are four different pigments which contribute to the primary electron transfer, namely the special pair P, the accessory bacteriochlorophyll B, the bacteriopheophytin H and the ubiquinone Q_A (see section 3.3). They can have a number p of possible product states $\{S_j\}_{j=1}^p$ (excited states, charge transfer states, etc). Thus, the corresponding population vector is defined as follows:

$$\mathbf{N}(t) := (N_1(t), \dots, N_p(t))^t \quad (2.41)$$

We will consider an ensemble of N different molecules, each of them having the same dynamics. The general model assumes the transfer of only one electron

per transition, therefore the components of the vector can be described using the oxidation properties of the pigments:

N_1	Molecules in the initial state where all pigments are in the equilibrium state, except for the excited primary electron donor (P^*).
\dots	\dots
N_p	Molecules in the final state where all intermediate pigments are in the equilibrium state, except for the oxidized primary electron donor (P^+) and reduced final electron acceptor (Q_A^-).

Conservation of the number of electrons implies:

$$\sum_{i=1}^p N_i = N \quad (2.42)$$

Directly after the excitation, all excited reaction centers will have only the first state N_1 populated, corresponding to P^* . To compute the time evolution for the i -th state N_i it is necessary to solve a system of ordinary differential equations:

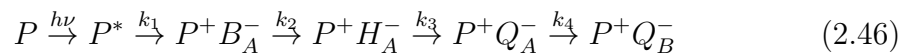
$$\frac{dN_i(t)}{dt} = - \sum_{j=1}^p \hat{K}_{ij} N_j(t) \quad i \in \{1, \dots, p\} \quad (2.43)$$

$$\mathbf{N}(t=0) = (N, 0, \dots, 0)^t \quad (2.44)$$

The rate matrix \hat{K} is assumed to be time independent, and contains information about the forward and backward recombination rates as well as the relaxation time of each state. For a *sequential model*, where the electron has only four forward rates, the general rate matrix is given by:

$$\hat{K} = \begin{pmatrix} k_1 & 0 & 0 & 0 \\ -k_1 & k_2 & 0 & 0 \\ 0 & -k_2 & k_3 & 0 \\ 0 & 0 & -k_3 & k_4 \end{pmatrix} \quad (2.45)$$

This model can be applied to the electron transfer in reaction centers from *Rhodobacter sphaeroides* to test the following sequence of charge transfer states:



The general solution to (2.43) is given by:

$$N_i(t) = \sum_j \hat{N}_{ij} e^{-\Lambda_j t} \quad (2.47)$$

where Λ_j is the j -th eigenvalue of the rate matrix. These coincide with the rate constants k_i for the sequential model. In other words, the decay constants are the reciprocals of the eigenvalues of the rate matrix.

The auxiliary matrix \hat{N} depends on the rate model and initial conditions. For rate constants $k_1 = (3.5 \text{ ps})^{-1}$, $k_2 = (0.9 \text{ ps})^{-1}$, $k_3 = (200 \text{ ps})^{-1}$, $k_4 = 0$ it is given by:

$$\hat{N}_{ij} = \begin{pmatrix} 1 & 0 & 0 & 0 \\ 0.3461 & -0.3461 & 0 & 0 \\ -1.3701 & 0.3477 & 1.0224 & 0 \\ 0.0239 & -0.0015 & -1.0224 & 1 \end{pmatrix} \quad (2.48)$$

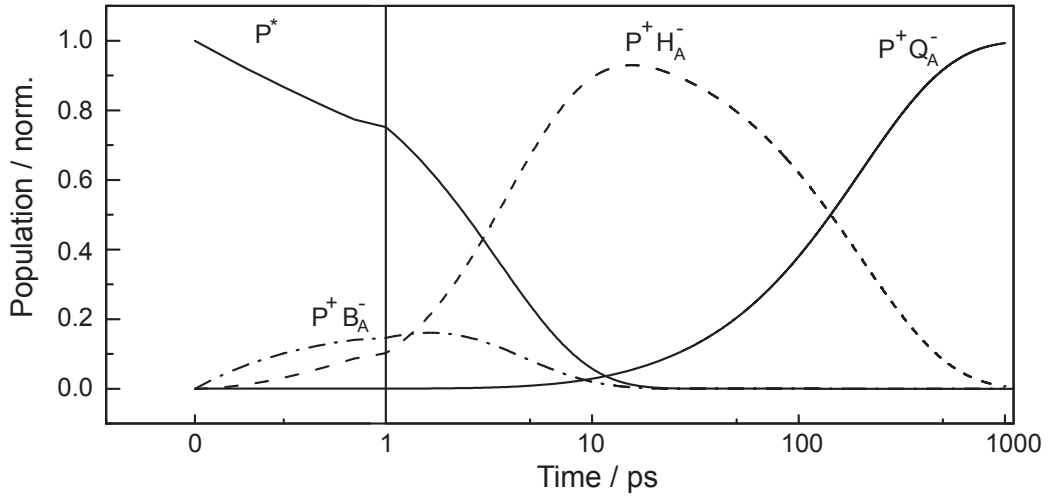


Figure 2.5: Evolution of the charge transfer states for a sequential model. The time scale is linear in the range [0,1] ps and logarithmic afterward. The population of the first intermediate $P^+B_A^-$ is very small, thus very difficult to detect.

2.6 Singular value decomposition (SVD)

In this section we will deal with an important mathematical tool which can improve the analysis of time resolved data. For this, it is necessary to represent the transient absorption spectra as a matrix M with a number of T rows, corresponding to the time steps, and Λ columns, which correspond to the spectral channels:

$$M_{\alpha\beta} = \Delta A(t_\alpha, \lambda_\beta) + R_{\alpha\beta} \quad (2.49)$$

$$= \frac{L}{\ln(10)} \sum_{i=1}^p \Delta\sigma_i(\lambda_\beta) N_i(t_\alpha) + R_{\alpha\beta} \quad (2.50)$$

The quantity $R_{\alpha\beta}$ describes the noise present in the measurement. In this thesis we consider $\Lambda = 512$ channels and $T = 123$ time steps. Therefore the number of entries in the data matrix is $\Lambda \cdot T = 62976$.

2.6.1 SVD-Filter

The SVD-theorem assures the existence of three matrices U , S and V such that:

$$M = U \cdot S \cdot V^t \quad (2.51)$$

In this equation the dimension of matrices U and M is $T \times \Lambda$ (without general restriction we assume $T \geq \Lambda$, otherwise one has to perform the decomposition with the transposed matrix M^t), S and V^t are $\Lambda \times \Lambda$ matrices. Both U and V are orthogonal matrices². The diagonal matrix S contains the *singular values* (SV) of the matrix M : $s_1 \geq s_2 \geq \dots \geq s_\Lambda$. The largest singular values represent the most significant information contained in the data matrix.

In the case of a noise-free signal ($R_{\alpha\beta} = 0$), where $N_k(t)$ are determined by a sum of p exponential functions, the higher singular values with $j > p$ vanish ($s_j = 0$, for $j > p$). When the signal contains other contributions ($R_{\alpha\beta} \neq 0$) the higher singular values do not vanish.

$$M_{\alpha\beta} = \sum_{i,j=1}^{\Lambda} U_{\alpha i} \underbrace{S_{ij}}_{=s_i \delta_{ij}} (V_{j\beta})^t = \sum_{j=1}^{\Lambda} U_{\alpha j} s_j V_{\beta j} \quad (2.52)$$

$$= \sum_{j=1}^m U_{\alpha j} s_j V_{\beta j} + \sum_{j=m+1}^{\Lambda} U_{\alpha j} s_j V_{\beta j} = \sum_{j=1}^m U_{\alpha j} s_j V_{\beta j} + \epsilon_{\alpha\beta} \quad (2.53)$$

²Because the matrix U is non-square it should be more properly called semi-orthogonal, meaning that $UU^t = I_{T \times T}$ and $U^t U = I_{\Lambda \times \Lambda}$.

Setting higher singular values s_n with $n > m$ to zero will lead to a modified data matrix \tilde{M} where the noise may be reduced (SVD-Filter).

$$\tilde{M}_{\alpha\beta} = \frac{L}{\ln(10)} \sum_{i=1}^p \Delta\sigma_i(\lambda_\beta) N_i(t_\alpha) + \underbrace{R_{\alpha\beta} - \epsilon_{\alpha\beta}}_{\delta_{\alpha\beta}} \quad (2.54)$$

$$= \tilde{U} \cdot \tilde{S} \cdot \tilde{V}^t + \delta_{\alpha\beta} \quad (2.55)$$

The quantity $\delta_{\alpha\beta}$ may be small if the number m of primary SV is chosen accurately, but it will never be zero. In other words, the SVD-Filter eliminates noise present in the whole data-set. However, the choice of a too small number m may eliminate relevant information in the data matrix. It is therefore useful to estimate the approximation error $\epsilon_{\alpha\beta}$ using the Frobenius norm [Sat04].

$$\|M_{\alpha\beta}\|_F := \left(\sum_{\alpha} \sum_{\beta} M_{\alpha\beta}^2 \right)^{1/2} \quad (2.56)$$

$$\|M_{\alpha\beta} - \sum_{j=1}^m U_{\beta j} s_j V_{\alpha j}\|_F = \|\epsilon_{\alpha\beta}\|_F = \left(\sum_{i=m+1}^{\Lambda} s_i^2 \right)^{1/2} \quad (2.57)$$

A more meaningful statistical quantity is the *residual standard deviation* (RSD) corresponding to the approximation with m -SV. This is then related to the previous equation as follows:

$$\sigma_{rsd}(m) := \frac{1}{\sqrt{(T-m) \cdot (\Lambda-m)}} \left(\sum_{i=m+1}^{\Lambda} s_i^2 \right)^{1/2} \quad (2.58)$$

Therefore the number m of primary SV should lead to a σ_{rsd} which is lower than the experimental error.

2.6.2 Number of significant singular values

The development of the SVD-filter and its applications enables us to eliminate undesired information present in the data. However a main drawback of this technique is the introduction of systematic errors when dealing with an insufficient amount of primary SV. In other words, even though the data might be smooth enough, a reduced number of SVD-components may not display kinetic information from intermediate states with small signal amplitudes [SZ03, Mic13]. The following section presents two different methods to evaluate the number of SV needed for a correct analysis of the measurements.

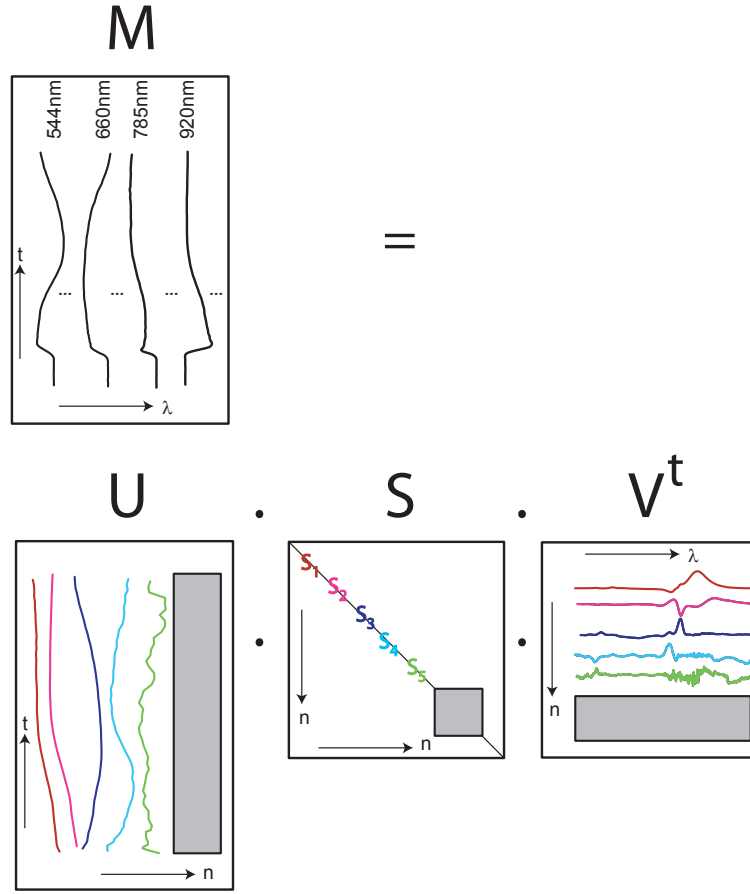


Figure 2.6: Schematic representation of the singular value decomposition (SVD). The data matrix may be decomposed as a linear combination of columns from U and rows from transposed V . The gray regions correspond to elements which have no relevant information and thus may be considered as noise.

The first method to evaluate the number of necessary SV is the *autocorrelation* test [SH82]. A simple but effective analysis evaluates the autocorrelation coefficient for the different columns of the U and V matrix defined in (2.51). These vectors contain information about the significance of the corresponding SV. The autocorrelation for the k -th SV is defined as:

$$a_U(k) = \sum_{l=1}^{T-1} U_{l,k} \cdot U_{l+1,k}, \quad a_V(k) = \sum_{l=1}^{\Lambda-1} V_{l,k} \cdot V_{l+1,k} \quad (2.59)$$

The selection criteria consist in identifying the SV having $a_{U/V} > 0.5$. Column vectors with lower autocorrelation display no physical information and the corresponding SV can be neglected.

The second method is the *median absolute deviation*(MAD) test [Mal09]. This procedure analyzes the significance of the k -th SV by considering the statistical properties of a sequence of approximation errors $\sigma_{rsd}(k)$ (definition see equation (2.58)).

$$v_k := \left\{ \sigma_{rsd}(j) \right\}_{k \leq j < \Lambda} \quad 1 \leq k < \Lambda \quad (2.60)$$

In the search for the primary SV it is therefore necessary to look for outliers in the sequence v_k , whose components contains all remaining RSDs after choosing only the largest k -SV. A fast evaluation is done by considering the distance to the median value of the sequence:

$$\Delta_k := \left\{ |\sigma_{rsd}(i) - \text{median}(v_k)| \right\}_{k \leq i < \Lambda} \quad 1 \leq k < \Lambda \quad (2.61)$$

Since the RSD is small for negligible SV, the last components of v_k will have very similar values for k sufficiently large. In this case the sequence Δ_k will be small. If instead k is smaller than the number of primary SV, then there will be an outlier which has significant different values than the rest. Therefore we consider the median absolute deviation of the sequence. This defines the width in the histogram where no outliers are found:

$$MAD(k) = \text{median}(\Delta_k) \quad (2.62)$$

Computing the distance to the median of the sequence provides the correct quantity to be compared to the MAD:

$$\epsilon(k) := |\sigma_{rsd}(k) - \text{median}(v_k)| \quad (2.63)$$

The outliers k_o are defined as the values lying five median absolute deviations away from the median of the sequence (see figure 2.7).

$$\epsilon(k_o) \geq 5 \times MAD \quad (2.64)$$

Finally it is important to notice that each $\sigma_{rsd}(k)$ is related to $s_{k+1}, \dots, s_\Lambda$. In other words the index k_o^{max} , which corresponds to the largest index having an outlier $\sigma_{rsd}(k_o^{max})$, does not contain the largest primary SV s_p . Thus the number of primary SV is given by the maximal index outlier plus one:

$$p = k_o^{max} + 1 = \max_{\text{outliers}} \{k_o\} + 1 \quad (2.65)$$

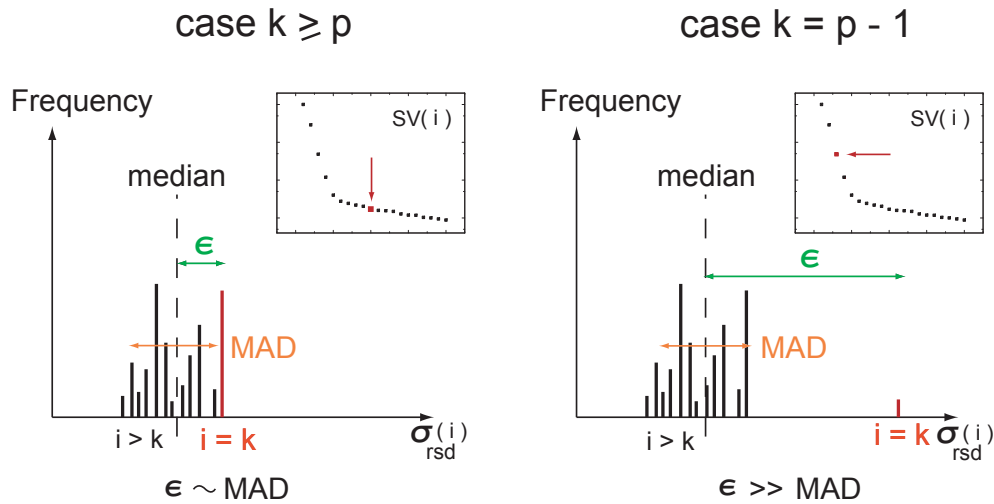


Figure 2.7: Schematic representation of the MAD-test. The histogram of computed $\sigma_{rsd}(i)$ is shown for the case $k \geq p$ (left) and $k = p - 1$ (right). First 20 singular values are plotted as inset. This analysis is well suited to identify outliers in the distribution.

To conclude with, both presented algorithms determine the same amount of SV if the data has moderate amount of noise. Nevertheless our experience shows that the MAD-test is more stable than the autocorrelation coefficient analysis.

2.7 Electron transfer theory

The transfer of an electron from one donor molecule (D) to an acceptor molecule (A) is a complex quantum mechanical process. This can be a classically allowed transition or a pure quantum mechanical *tunneling* between two potential energy surfaces. A very intuitive and powerful theory, developed by **Marcus** fifty years ago, will be considered to estimate the mean transfer rate in a non-adiabatic charge transfer process.

2.7.1 Non-adiabaticity

We begin with the concept of *diabatic states*. By this we understand a molecular state in thermal equilibrium with a reservoir which evolves on the potential energy surface. In the case where two coupled diabatic states are present, the resulting energy surface may not only be the superposition of the original ones. If the coupling is strong enough, the energy surfaces will be deformed at the crossing point. The transition between two diabatic states in the strong coupling limit is called *adiabatic*, meaning that the oscillating system will change its molecular configuration without

barrier - a very fast process. For example, the electron transfer in bacterial reaction centers at room temperature would have a rate constant larger than $(250 \text{ fs})^{-1}$ (Bixon, Jortner 1991).

In the weak coupling limit, the two *diabatic* energy surfaces remain essentially unchanged. The molecule has the classical interpretation of being either in the initial or final state, but never in a superposition of both.

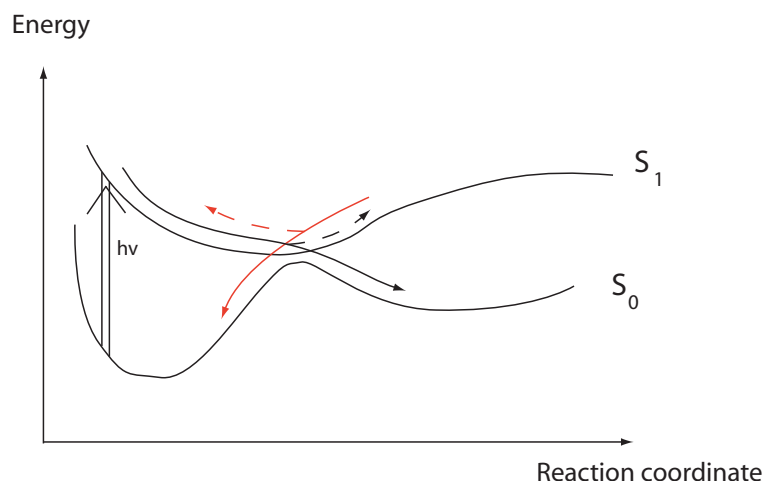


Figure 2.8: Non-adiabatic transfer between two potential energy surfaces after photoexcitation.

The non-adiabatic transition probability from an energetically unfavorable state S_1 into an energetically favorable state S_0 can be computed as follows: neglecting radiative effects, the transition will more probably take place at the molecular configuration given by the intersection point between the two diabatic states. The crossing probability P can be computed using the *Landau-Zener* formula [Lan32, Zen32]:

$$P = 1 - \exp\left(-\frac{2\pi}{\hbar}|V|^2\frac{1}{v|\Delta s|}\right) \quad (2.66)$$

Here V is the transfer matrix element, v is the velocity at the crossing point and Δs is the difference in slope of the two surfaces at their intersection point. For non-adiabatic transitions, the crossing probability is very small, meaning that the system has to complete many oscillations in the upper surface before relaxing to the lower state. In photosynthetic reaction centers at room temperature, this corresponds to rate constants lower than $(250 \text{ fs})^{-1}$.

2.7.2 Marcus theory

The non-adiabatic transition between a state DA , where both donor and acceptor molecules are in the equilibrium state, to a state D^+A^- , where the donor is oxidized and the acceptor reduced, can be approached by considering the corresponding *polarization free energy surfaces* within thermal equilibrium at temperature T . These *diabatic* states correspond to an *ensemble* of molecular states at the given temperature, which display a harmonic behavior in the vicinity of the minimum energy point [Mar63, DeV84]. After the electron transfer, the surrounding molecules become polarized due to the new charge distribution. Consequently, a considerable amount of energy is necessary to reorganize the system in order to generate a favorable configuration in which the electron can be transferred.

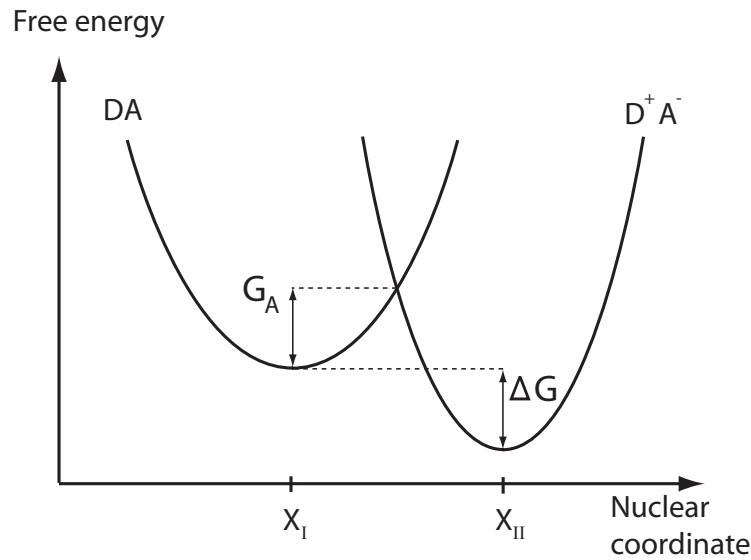


Figure 2.9: Application of Marcus theory. The free polarization energy surfaces are assumed to be parabolas for both initial and final diabatic charge transfer states.

The reorganization energy λ is defined as the free energy necessary to change the initial equilibrium nuclear coordinate X_I to the corresponding value after the electron transfer X_{II} , however without transferring the electron. For this harmonic model, it is related to the activation energy G_A as follows:

$$G_A = \frac{(\lambda - \Delta G)^2}{\lambda} \quad (2.67)$$

A transfer having small or large values of λ will be inefficient, because the corresponding energy barrier is high. Only systems with $\lambda \sim \Delta G$ will have a nearly activation-less electron transfer, consequently with fast transfer rates.

The rate of the process can then be computed using (2.66) for a harmonic oscillator:

$$k_{DA \rightarrow D^+A^-} = \frac{2\pi}{\hbar} |V|^2 \frac{1}{\sqrt{4\pi\lambda k_B T}} \exp\left(-\frac{(\lambda - \Delta G)^2}{4\lambda k_B T}\right) \quad (2.68)$$

2.7.3 Application to reaction centers

Combining the Landau-Zener formula with the Marcus theory it is possible to estimate the coupling matrix elements V using decay information present in time resolved experiments and vice versa. In the case of non-adiabatic electron transfer in bacterial reaction centers, two main models are still discussed in the literature. These involve the primary electron donor special pair P , the accessory bacteriochlorophyll B_A , the bacteriopheophytin H_A and the ubiquinone Q_A (see section 3.3). Both models have one thing in common: after photoexcitation the state P^* starts a series of activationless reactions, where the electron is transferred from P to Q_A within 200 ps. The intermediate steps can be summarized as follows:

In the *superexchange model*, the electron is transferred from P to H_A and further to Q_A without populating the intermediate cofactor B_A . Since the distance between P and H_A is quite large ($\sim 20 \text{ \AA}$), a direct transfer is not possible. For this reason, the chlorophyll B_A plays an important role as virtual state, whose interaction matrix element rises the forward transfer rate. Moreover the energy $E(P^+B^-)$ should be larger than $E(P^*)$ (Bixon, Jortner et al. 1991).

In the *sequential model*, the electron is transferred forward as described in equation (2.46) without backward reactions. Because of the high transfer efficiency, the chlorophyll B_A must be only shortly populated. This reaffirms the hypothesis that the second time constant $\tau(P^+B^- \rightarrow P^+H^-)$ is smaller than the first one $\tau(P^* \rightarrow P^+B^-)$.

The differences between these two models were exhaustively analyzed by Marcus [Mar87]. He considered studies of magnetic field effects on the back transfer reactions. The estimates for the coupling matrix elements are summarized in the following table:

Matrix element	V_{PB}	V_{BH}	V_{PH}
Coupling / cm^{-1}	17	35	0.7

Assuming a typical reorganization energy $\lambda = 1290 \text{ cm}^{-1}$ ($= 0.16 \text{ eV}$), it is possible to use (2.66) to estimate the adiabaticity of the reaction. The crossing probability will reach unity when the coupling is at least 135 cm^{-1} , a value almost four times larger than those reported above. At this point, the non-adiabaticity assumption for the electron transfer in reaction centers is founded.

Finally, it is possible to estimate the decay constants predicted for both models. In particular, the time constant for a superexchange transfer is 1000 larger than measured experimental values.

	Computed decay time / ps		
	$\tau(P^* \rightarrow P^+B^-)$	$\tau(P^+B^- \rightarrow P^+H^-)$	$\tau(P^* \rightarrow P^+H^-)$
Superexchange	-	-	2000
Sequential	3	0.6	-

2.8 Fit algorithms and data analysis

As it was discussed in section 2.5, an exponential behavior of the transient absorption signal $\Delta A(t, \lambda)$ is expected if the system undergoes a rate process. This is particularly true for a non-adiabatic electron transfer reaction.

$$\Delta A(t, \lambda) = \frac{L}{\ln(10)} \sum_{i=1}^p \Delta \sigma_i(\lambda) N_i(t) = \frac{L}{\ln(10)} \sum_{i,j=1}^p \hat{N}_{ij} \Delta \sigma_i(\lambda) e^{-k_j t} \quad (2.69)$$

The canonical multiexponential fit of the data is performed by minimizing the chisquare over a data set having T time steps and Λ channels using a set of independent exponential functions:

$$\chi^2(a, \tau) = \sum_{\beta=1}^T \sum_{\alpha=1}^{\Lambda} \left(\Delta A(t_{\alpha}, \lambda_{\beta}) - \sum_{i=1}^p a_i(\lambda_{\beta}) e^{-t_{\alpha}/\tau_i} \right)^2 \stackrel{!}{=} \min \quad (2.70)$$

The obtained fit amplitudes a_i are called *decay associated difference spectra* (DADS), giving only information on the dynamics present in the measurement. On the other hand, the microscopic information is contained in the *species associated difference spectra* (SADS) $\Delta \sigma_i$, since they describe the absorption of each single intermediate state. The relationship between both can be computed when a specific kinetic model is assumed:

$$\Delta \sigma_i(\lambda) = \frac{\ln(10)}{L} \sum_{j=0}^p \hat{N}_{ji}^{-1} a_j(\lambda) \quad (2.71)$$

2.8.1 Target analysis

Another method to obtain the SADS is to fit a given kinetic model to the data [Hol96, SLG04]. This means that the matrix $\hat{N}_{ij}(k_1, \dots, k_p)$ is known directly as a function of the rate constants. Using (2.47) it is possible to rewrite the data matrix:

$$\tilde{M}_{\alpha\beta} = \Delta A(t_\alpha, \lambda_\beta) = \frac{L}{\ln(10)} \sum_{i=1}^p \Delta \sigma_i(\lambda_\beta) N_i(t_\alpha) \quad (2.72)$$

$$= \frac{L}{\ln(10)} \sum_{i=1}^p \Delta \sigma_i(\lambda_\beta) \cdot \sum_{j=1}^p \hat{N}_{ij} e^{-t_\alpha/\tau_j} \quad (2.73)$$

Therefore, the SADS are the fit amplitudes of $\tilde{M}_{\alpha\beta}$ using the set of basis functions $\{basf_i(t)\}_i$ given by the components of the population vector $\mathbf{N}(t)$:

$$basf_i(t) = N_i(t) = \sum_{j=1}^p \hat{N}_{ij} e^{-t/\tau_j} \quad (2.74)$$

Notice that in equation (2.74) the matrix \hat{N}_{ij} also depends on the time constants $\tau_i = (k_i)^{-1}$, thus it is a variable quantity which should be fitted too for achieving the minimum of the chi-square:

$$\chi^2(\Delta\sigma, \tau) = \sum_{\beta=1}^T \sum_{\alpha=1}^{\Lambda} \left(\Delta A(t_\alpha, \lambda_\beta) - \sum_{i=1}^p \Delta \sigma_i(\lambda_\beta) basf_i(t_\alpha) \right)^2 \stackrel{!}{=} \min \quad (2.75)$$

However in this thesis the matrix \hat{N}_{ij} was considered constant in the fitting procedure, whose entries were a priory set to match a sequential model with given time constants. The output of the fit, which determined the best τ_i , was used to recompute the matrix \hat{N}_{ij} using the new values and the global fit was repeated. This routine was iterated until both quantities are consistent with the a priory assumptions. This approach is justified if the a priory values (estimated using a canonical fit) lie in the vicinity of the minimum, since in this case the variation of global parameter influences mostly the exponential term.

2.8.2 Single value decomposition and target analysis

An alternative method to perform *target analysis* is to fit only the major components of the data matrix. One possible example is to reconstruct the data using the first m-largest singular values from the SVD. As already discussed in section 2.6, this filtering method can considerably reduce the present noise. Despite this advantage,

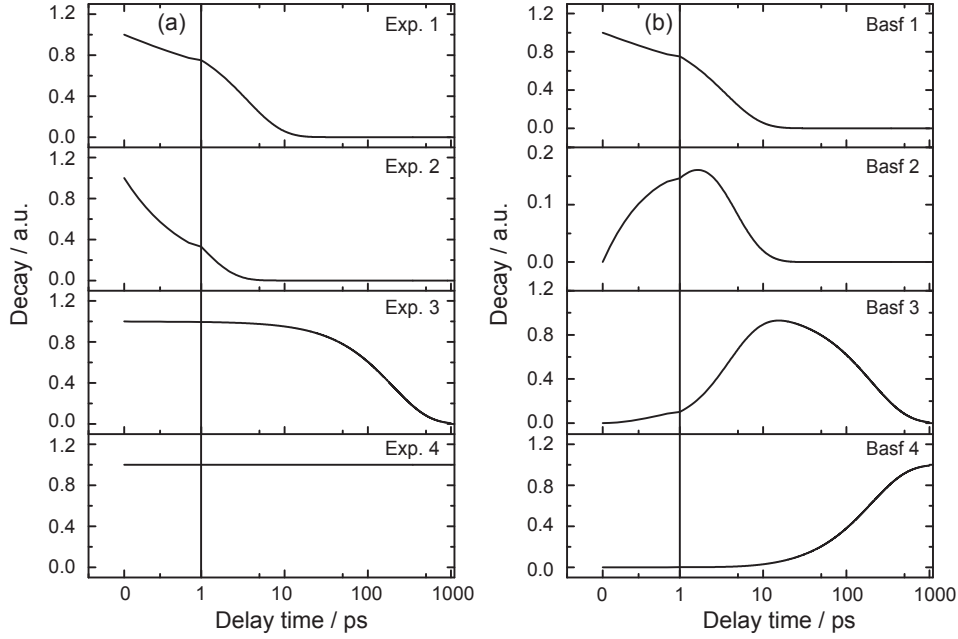


Figure 2.10: Set of functions used to fit the transient data using pure exponential decay (a) and a linear combination given by the kinetic model (b). The time constants are arranged in the order 3.5, 0.9, 200 and $1 \cdot 10^8$ ps.

it is always very problematic to determine how many singular values are to be taken even with current test algorithms. A better and more reliable fit can then be achieved by considering the *decomposed time traces* of the matrix. They can be obtained by multiplying (2.51) with the matrix V [KKN06]:

$$U_{\alpha j} \cdot s_j = \sum_{i=1}^p C_{ij} N_i(t_{\alpha}) + R_{\alpha j}^{(dec)} \quad (2.76)$$

This new representation of the measured data displays the contribution of each singular value in the time domain. In this way it is possible to analyze which kinetics may be lost by deleting the smallest singular values. Complicated as it may appear, this systematic method avoids eliminating those kinetic components with small amplitudes.

The decomposed time traces also have a non vanishing noise, which can be observed at small singular values where the signal is not very high:

$$R_{\alpha j}^{(dec)} = \sum_{\beta} R_{\alpha \beta} V_{\beta j} \quad (2.77)$$

The matrix C_{ij} in equation (2.76) is called *C-matrix*. It is the analog of $\Delta\sigma_i(\lambda)$, with the difference that its number of components is appreciably reduced. This is

because the *C-matrix* spans only over the largest m -singular values and the number of time points T , whereas the SADS span over the wavelength channels Λ and the same number of time points. The linear relation between these two quantities is given by the matrix V :

$$C_{ij} = \sum_{\beta=1}^{\Lambda} V_{\beta j} \cdot \Delta\sigma_i(\lambda_{\beta}) \quad (2.78)$$

At this point it is possible to use the target analysis as explained in section (2.8.1). The previously defined *C-matrix* is determined as the fit amplitude for the decomposed time traces, when using only the largest m singular values:

$$\chi^2(C, \tau) = \sum_{\alpha=1}^T \sum_{j=1}^m \left(U_{\alpha j} \cdot s_j - \sum_{i=1}^p C_{ij} \text{bas} f_i(t_{\alpha}) \right)^2 \stackrel{!}{=} \min \quad (2.79)$$

For the measurements considered in this thesis, the number of channels is $\Lambda = 512$, the number of time steps is $T = 123$, the kinetic model has $p = 4$ components and the number of considered singular values is $m = 5$. This corresponds to a decrease in the number of fit parameters by a factor 85.5.

Fit method	Linear parameter	Number of fit parameters
Canonical fit	$a_i(\lambda_{\beta})$	2052
Target analysis	$\Delta\sigma_i(\lambda_{\beta})$	2052
Singular value decomposition and target analysis	C_{ij}	24

2.8.3 Consistency analysis for the target model

Basics

In this last section we will show how to make a consistency test to verify if the kinetic model and corresponding fit parameters simulate the experimental data with satisfactory quality. This may be done by reconstructing the populations from the fitted linear parameters, which build the *C-matrix*. Actually, this does not mean that we are about to fit the populations, since those are already fixed via the rate model. Instead we are going to compare the theoretical populations with the reconstructed ones and calculate the deviation.

A given data set with m significant SV can have $p \leq m$ kinetic components. This is because the rank of the matrix is related to the number of independent dynamics present in the measurement. The case where $p > m$ corresponds to measurements with low signal-to-noise ratio which do not contain enough information to explain the underlying physical processes.

In the literature [KKN06] it is assumed that only the case $p = m$ has a physical meaning, otherwise it is not possible to invert the *C-matrix*. In the current section a new interpretation is presented where also larger numbers of singular values are allowed and the reconstruction of the population vector is still possible.

New interpretation

The most common situations have more SV than kinetics ($m > p$). At this point we propose to extend the *C-matrix* to a $m \times m$ square matrix *Csqr* in the following manner:

$$Csqr := \begin{pmatrix} C|_{(p \times p)} & C|_{p \times (m-p)} \\ 0 & \text{Diag}(s_{p+1}, \dots, s_m) \end{pmatrix} = \begin{pmatrix} C^{(0)} & C^{(1)} \\ 0 & C^{(2)} \end{pmatrix} \quad (2.80)$$

This kind of extension, called *embedding*, is not unique and any invertible matrix $C^{(2)}$ can be used. This specific choice however has three interesting properties: (i) Every column of the matrix scales as the corresponding SV. (ii) The extended matrix can be easily inverted, if $C(0)$ is invertible. (iii) The reconstructed population vectors depend only on $C(0)$ (see below).

The reconstruction of the population vector can be obtained by inverting equation (2.76). It is important to notice that the present noise $R^{(dec)}$ will also be fitted by the chisquare algorithm. The first p -components of the fully reconstructed vector \mathbf{P} correspond to the physical populations, while the last $(m-p)$ -components show the deviation of the fit from the target model.

$$\mathbf{P}(t) := \begin{pmatrix} \mathbf{N}^{rec}(t) \\ \mathbf{E}(t) \end{pmatrix} \quad (2.81)$$

$$P_i(t_\alpha) = \sum_{j=1}^m U_{\alpha j} \cdot s_j \cdot (Csqr)_{ji}^{-1} \quad 1 \leq i \leq m \quad (2.82)$$

$$N_i^{rec}(t_\alpha) = \sum_{j=1}^p U_{\alpha j} \cdot s_j \cdot (C^{(0)})_{ji}^{-1} \quad 1 \leq i \leq p \quad (2.83)$$

$$E_{i-p}(t_\alpha) = s_i^{-1} \cdot \sum_{k=1}^p C_{ki}^{(1)} \cdot (N_k(t_\alpha) - N_k^{rec}(t_\alpha)) \quad p+1 \leq i \leq m \quad (2.84)$$

Thus the components of the \mathbf{E} vector show the deviation of the fit from the target model, weighted by the normalized fit amplitudes $C^{(1)} \cdot s^{-1}$ over the remaining $(m-p)$ singular values. Furthermore, autocorrelation coefficients for the components P_i , in particular for N_i^{rec} and E_i , can be computed as a measure for fit quality:

$$\mathcal{A}_i := \left(\sum_{\alpha=1}^{T-1} P_i(t_\alpha) \cdot P_i(t_{\alpha+1}) \right) / \left(\sum_{\alpha=1}^T |P_i(t_\alpha)|^2 \right) \quad 1 \leq i \leq m \quad (2.85)$$

In this thesis it is suggested that the model can be accepted if the E-vector has $\mathcal{A}_i < 0.90$. In the contrary case the respective component contains a significant amount of information, proportional to $E_i \sim (N_i - N_i^{rec})$. In this case there are systematic deviations from the target model.

3 The photosynthetic purple bacteria *Rhodobacter sphaeroides*

Purple bacteria are anoxygenic phototroph organisms. They possess one of the simplest photosynthetic cycles among all prokaryotes, thus their study improved the understanding of many key mechanisms of photosynthesis from light absorption and energy conversion to energy storage. In this chapter we will discuss the properties of bacterial photosynthesis with special emphasis in the photosystem of *Rhodobacter sphaeroides* (*Rb. sphaeroides*). Other species like *Rhodospirillum rubrum*, *Chromatium vinosum* and *Rhodopseudomonas viridis* present many analogies.

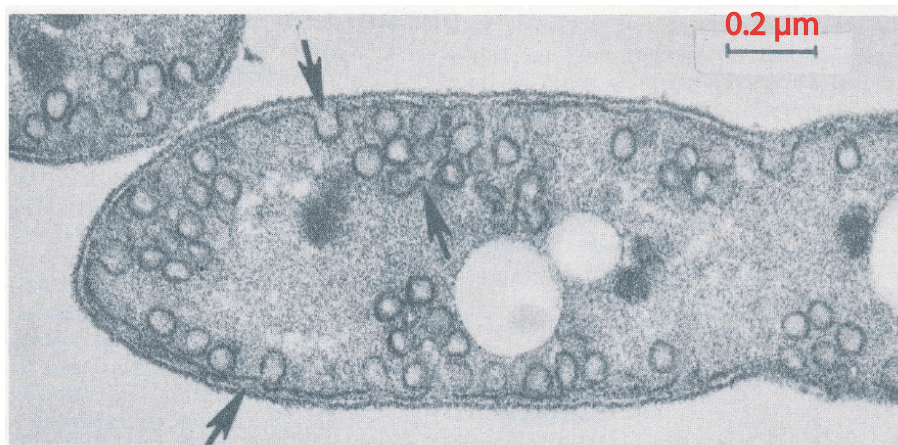


Figure 3.1: Electron micrograph of purple bacteria *Rb. sphaeroides*. The arrows indicate the position of the photosystem units where the reaction centers are located [Cla78].

3.1 The basic principles: light absorption and energy storage

The conversion of light energy into suitable biological units occurs in a specialized protein complex called photosynthetic unit. It consists of a large number of chlorophyll-like pigments which can absorb light in the visible and near-infrared spectrum where the solar-radiation has many photons (figure 3.2). If we consider the radiation power at full sunshine, a single chlorophyll molecule may absorb

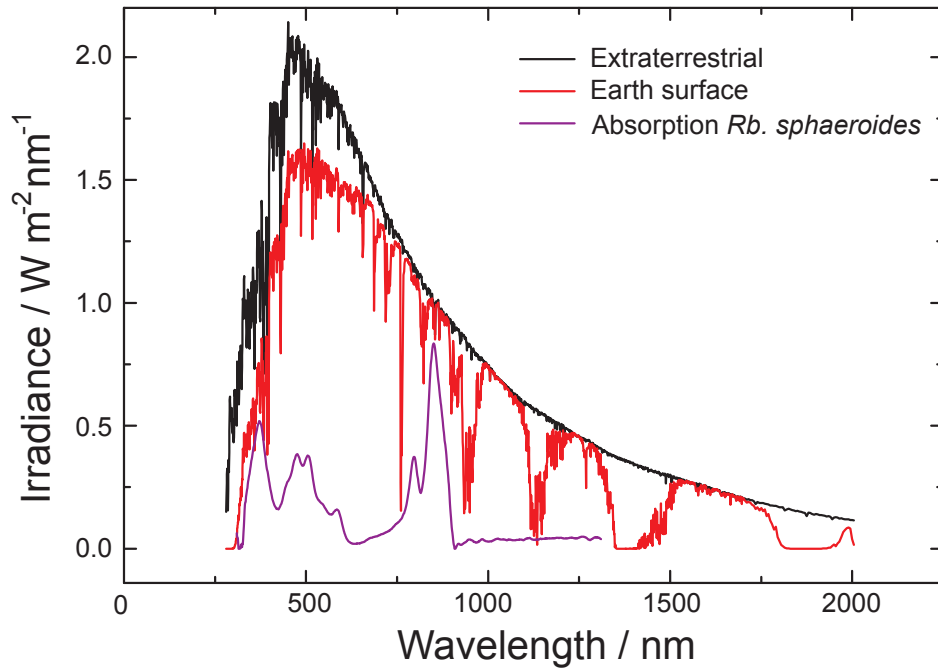


Figure 3.2: Solar irradiance spectra [Ame] and absorption spectrum of purple bacteria *Rb. sphaeroides* [BP07]. These photosynthetic organisms developed protein systems which can absorb the sunlight present at the earth surface.

at most 10 photons per second [Bla02]. For this reason, each photosynthetic unit consists mostly of a set of different antennas which transform and redirect light-energy into a trapping device called reaction center (RC). Two different types of antenna, or *light-harvesting complexes* (LH), can be found [McD95]. The LH2 antenna complexes are integrated in the membrane and appropriately distributed to allow maximal photon absorption. The number of antenna pigments is larger than those of RC and it depends on the conditions of the bacterial environment. The LH1 antenna are buried inside the membrane and form a ring around the RC. They collect the light-energy from the LH2 peripheral antenna and transmit it into the RC.

The RC is a transmembrane chlorophyll-protein complex located in a specially modified portion of the inner cell membrane of the organism called the *intracytoplasmic membrane* (see figure 3.1). It can be defined as the smallest protein complex capable of photosynthetic activity [Cla78]. This huge system is responsible for the initial steps of the photochemistry, which is efficient charge separation and electron transfer after photoexcitation. An electron is transported along the membrane using intermediate steps with very fast transfer rates, reducing the recombination losses (Wraight and Clayton et al. 1974). Accurate measurements show quantum

efficiencies of 98 % for *Rps. viridis* [Tri90]. The final state of the reaction is an oxidized primary electron donor, called *special pair* (P), and a reduced ubiquinone (Q^-) present in the reaction center as shown in figure 3.3. After a few milliseconds, a water soluble c-type cytochrome re-reduces the oxidized *special pair*. The overall energy efficiency for the charge separation process in RC is about 50 % (see [GD89] and references therein).

The next steps of the transmembrane reactions are still controversial. To this date however there is evidence that the process is repeated until a twofold reduced ubiquinone is produced (Q^{2-}) [Yea88, MOF90]. Due to the electrostatic interaction it is possible that this radical becomes hydrated (QH_2) and leaves the reaction center complex. A further cytochrome bc_1 complex dehydrates the ubiquinone and generates a proton gradient between the two sides of the membrane. The enzyme *ATP-synthase* uses this potential difference across the membrane and the respective *proton motive force* to synthesize ATP.

All things considered, a better utilization of renewable energy sources and corresponding design of artificial photosynthetic systems can be obtained by studying bacterial photosynthesis. In this context it is important to understand the primary reaction steps in RC. These will be elucidated in the following sections.

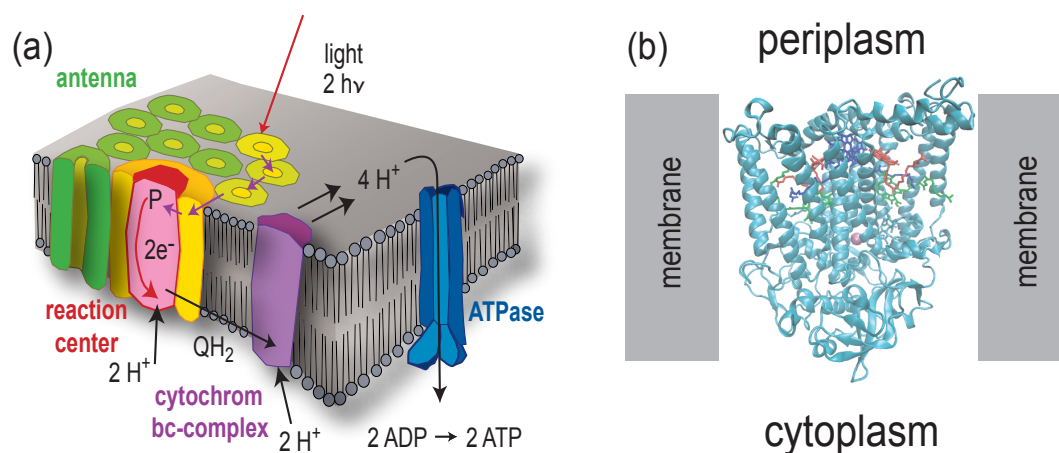


Figure 3.3: Distribution of protein complexes present in the photosynthetic unit at the intracytoplasmic membrane (a) and ribbon representation of the RC with the full protein backbone (b). The arrows show the synthesis of ATP after the absorption of two photons.

3.2 Structure of the reaction center

Isolation of RC from photosynthetic purple bacteria in a pure and photochemically active form was done by **Reed** and **Clayton** et al. 1968. First structural information on the RC from *Rb. sphaeroides* was obtained by determining the molecular weight and amino acid composition of the coarse elements via electrophoresis. Three main components with apparent weights 19, 22 and 28 kDa could be identified, called L (light), M (medium) and H (heavy) respectively [Cla80]. However this terminology is nowadays very confusing, because the experimental error of this technique can be as large as 30%.

A detailed structural analysis of a bacterial RC was first accomplished by **Deisenhofer** et al. [Dei84] using X-ray diffraction experiments of crystallized RC from *Rhodospseudomonas viridis*. Many analogies can be found in the RC from *Rb. sphaeroides*, whose structure was first resolved by **Allen** et al. [All87].

There are five α -helices in each of the L and M subunits which lie in the cell membrane (figure 3.3-b). The H subunit contains only one helix and crosses the membrane at the cytoplasmic side. On the periplasmic side there is an interrupted helix which connects the helices of the L and M subunits.

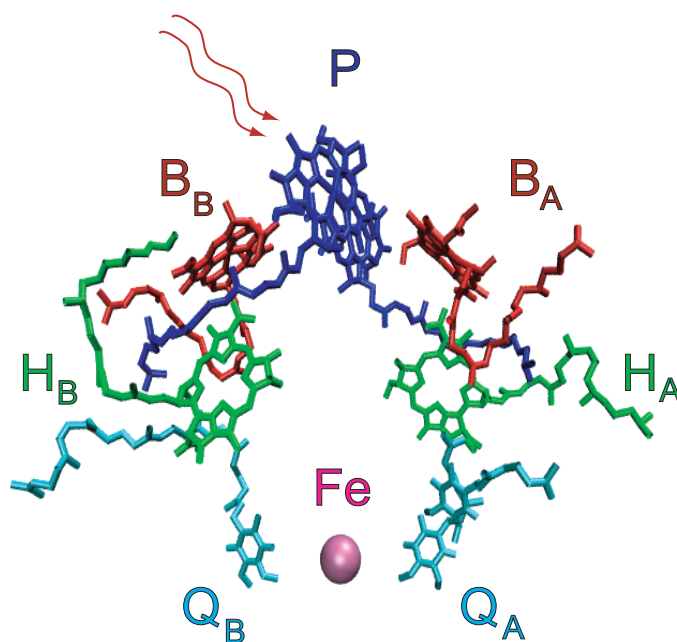


Figure 3.4: Molecular structure of Reaction Centers from *Rb. sphaeroides*. The cofactors involved in the charge transfer process are symmetrically distributed into two branches (A and B). In particular there are one bacteriochlorophyll dimer (P), two accessory bacteriochlorophylls (B), two bacteriopheophytins (H) and two ubiquinones (Q).

The electron transfer (ET) and charge separation is performed within the LM complex. A few discrete units, called pigments or cofactors, are responsible for this process, more precisely four bacteriochlorophylls-b (BChl), two bacteriopheophytins-b (BPhe), two ubiquinones (Q) and one non-heme iron atom. The BChl, BPhe and Q are symmetrically distributed into two branches with almost 2-fold rotation symmetry. In the modern nomenclature, the index A is used to indicate the molecules in the L-subunit and the index B for those in the M-subunit. The iron atom is then very close to the symmetry axis on the lower part of the system, near the ubiquinones.

Two of the four BChl form a dimer with excitonic coupling and delocalized unpaired electrons, which is the primary electron donor (*Special Pair* P) [Nor71]. This dimer is situated on the periplasmic side and it is very close to the symmetry axis too. The two remaining BChl are separated from the special pair and commonly denoted as *accessory chlorophyll* with the letter B. The BPhe are situated below the accessory chlorophylls and denoted with the letter H (this should not be confused with the H-protein subunit).

Last but not least, two main types of RC from *Rb. sphaeroides* can be distinguished: The wild type (WT) strain contains a carotenoid group attached covalently to the RC. This improves the photosynthetic efficiency by absorbing light in a spectral region where the chlorophylls do not, and serves as a photoprotector by quenching the electron transfer between chlorophylls and oxygen (triplet quenching) [CF87]. The R26.1 strain, also called *Rhodopseudomonas sphaeroides*, contain no carotenoid and can more easily be damaged when oxygen is present.

Absorption properties

A key element for understanding the absorption spectrum of isolated RC is the porphyrin monomer, a tetrapyrrol¹ system which forms part of the structure of BChl and BPhe. This almost planar molecule possesses four main $\pi \rightarrow \pi^*$ transitions called $\mathcal{B}_x, \mathcal{B}_y, \mathcal{Q}_x, \mathcal{Q}_y$ [Gou61]. The combination of the \mathcal{B}_x and \mathcal{B}_y bands, which overlap at room temperature, is called *Soret band* and is located in the UV region. The other two bands form the common absorption spectrum in the blue-visible and near-infrared, respectively.

The Q-bands of isolated reaction centers from *Rb. sphaeroides* correspond to porphyrin transitions for the different type of cofactors. The special pair (P) has the absorption maximum at 620 and 865 nm, the bacteriochlorophyll (B) has two narrow bands at 600 and 800 nm and the bacteriopheophytin (H) absorbs around 540 and 750 nm.

Due to the excitonic character of the special pair, its \mathcal{Q}_y band has two possible states called P_+ and P_- . The P_- excited state was already described above with

¹Pyrrole is an aromatic ring compound (C_4H_4NH)

absorption maximum at 865 nm. The second excited state P_+ takes place at 810 nm and overlaps with the absorption of the accessory chlorophyll B (Jonas, Fleming et al. 1996).

The absorption spectrum, as well as the linear and circular dichroism spectrum, can be modeled using a simple excitonic coupled hamilton operator [Kna85]. A careful analysis shows that the influence of the Soret bands on the absorption spectrum is less than 8%. As a consequence, it is not very useful to perform UV spectroscopy when studying the electron transfer dynamics and therefore this spectral region will be discarded. On the opposite, the coupling between Q_x bands of different cofactors is ten times smaller than the Q_y coupling. For this reason it is convenient to study the charge separation process by exciting the special pair at the physiological wavelength of 865 nm and focusing the probing process to the range of the Q_x and Q_y transitions.

The unusual absorption between 450-570 nm corresponds to a carotenoid group attached to the RC. It fills the spectral region where the other cofactors do not absorb.

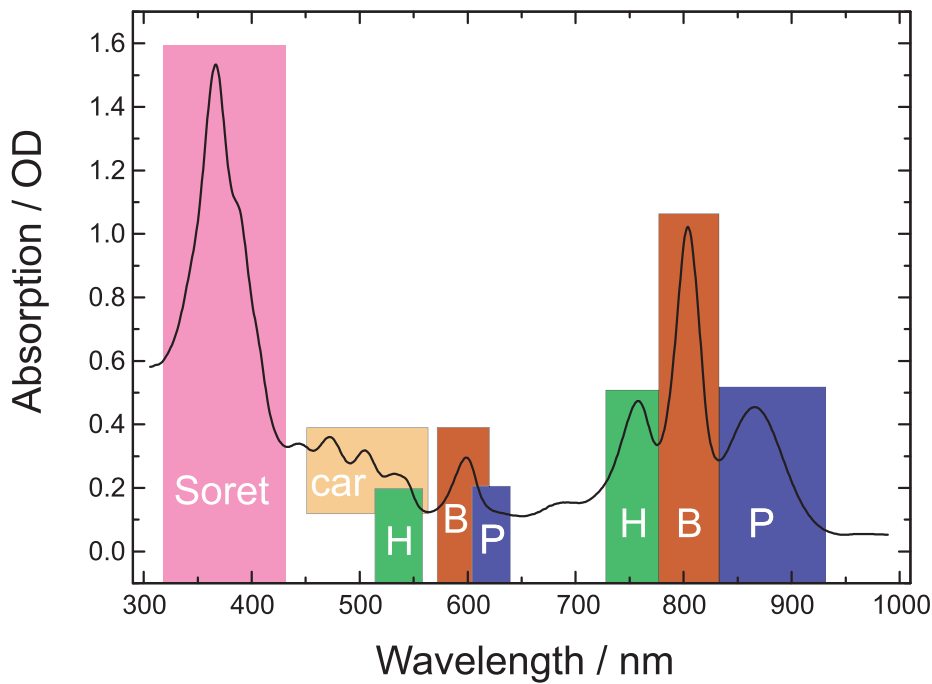
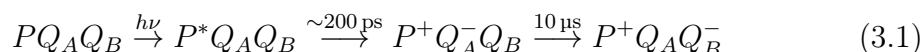


Figure 3.5: Absorption spectrum of reaction centers from *Rb. sphaeroides*. The contribution from different pigments can be determined.

3.3 Photochemical reaction and electron transfer

The photochemical process starts when P is excited at 865 nm, resulting in an excited singlet state $^1P^*$. A sequence of intermediate electron transfer processes take place only on the A-Branch (figure 3.4) and leave the special pair oxidized and the quinone Q_B reduced [Yea88, Par82]. This was already measured before the structure of the RC could be resolved, and can be summarized as:



In order to account for a charge separation quantum yield of almost 1, it is imperative to study the properties of the intermediate steps present in the electron transfer process. The following section summarizes the main contributions done until the present date. The first evidence of a radical $P^+B_A^-$ ([Hol89]) originated a paradigm change in the discussion of electron transfer and it will be taken as division point between old and new measurements.

3.3.1 Chronology 1970-1990

The first set of publications regarding electron transfer and charge separation deals with measurements using the first picosecond and femtosecond laser systems available for time resolved spectroscopy. They are usually characterized by a low repetition rate, a limited temporal resolution and suboptimal signal-to-noise ratio. Theoretical work used simple but efficient computation techniques, which gave an important insight of the problem, unfortunately with ambiguous results.

The participation of a bacteriopheophytin (H) in the photosynthetic cycle was already stated by **Fejer** et al. [Faj75], but first evidence of an intermediate step was found by **Holten** et al. [Hol78] for *Rhodopseudomonas viridis* with the reduction of H_A .

The original idea of an intermediate step with a reduced bacteriochlorophyll ($P^+B_A^-$) was proposed by **Shuvalov** et al. [Shu78] for *Rhodospirillum rubrum*, and the electron should move from P to B_A in less than 15 ps.

Holten et al. [Hol80] did experiments with excitation at 530 nm and 600 nm using 7 ps flashes. They identified the bleaching at 545 nm upon formation of the H^- anion. The identification of a P^+B^- was not clear, because the bleaching at 800 nm could be due to a secondary process, instead of the reduction of the BChl. The measurements showed that the oxidation of P also results in an absorption decrease near 805 nm, and an increase near 790 nm. There was also a 30 ps kinetic at 803 nm, whose participation in the primary electron transfer was rejected. They concluded that the transfer $P^* \rightarrow P^+H^-$ occurs within 4 ps and a formation of P^+B^- should be even faster.

Woodbury et al. [Woo85] did subpicosecond measurements by exciting the Q_x band of the special pair P at 610 nm with 0.8 ps pulses. First evidence of the $P^+B_A^-$ state was observed, especially at 755 nm. Nevertheless this model was rejected because the time resolution was not good enough and the bleaching at 800 nm did not coincide with the formation of $P^+H_A^-$. Comparison with fluorescence measurements showed that the negative signal at 920 nm corresponded to the stimulated emission from P^* , whose lifetime was estimated to be $\tau(P^*) = 4.1$ ps. This coincided with the formation of P^+ . Unfortunately, it was possible that the other Q_x band of B became also excited at 610 nm, and the signal may have been generated by a mixed excitation of P and B .

Martin and Breton et al. [Mar86] excited the Q_y band of the special pair P at 850 nm. The setup had 150 fs excitation pulse and 10 Hz repetition rate. First evidence of a blue shift of the 800 nm band was observed, which could be assigned to an electrochromic effect of P^+ on the Q_y transition of the two accessory bacteriochlorophylls (B) whose absorptions overlap at 800 nm. The decay of P^* was fitted with a 2.8 ps time constant at 675, 870 and 1240 nm. The authors did not find evidence for a fast bleaching in the 0.1-2 ps range at 800 nm, probably because the noise in the data was high. They concluded by assuming that a small time constant should have less than 100 fs, and may be associated with vibrational relaxation within the $^1P^*$ singlet state, thus irrelevant for the electron transfer.

Breton et al. [Bre88] did low temperature measurements at 10 K with excitation pulses of 200 fs at 780, 810 and 870 nm and found a bleaching of P^* of 1.2 ps, but no transient bleaching of B, thus no $P^+B_A^-$ state. Here, one should notice that despite the short excitation pulses, the cross-correlation at 800 nm between pump and probe was larger than 1 ps.

Kirmaier and Holten [KH88] did measurements with RC from *Rhodobacter capsulatus* at room temperature with 350 fs pulses and excitation at 870 and 582 nm. The transient spectra were acquired in the NIR region between 720-840 nm. The time constants found were 3.5 and 209 ps, no sign of a fast kinetic. Two isosbestic points at 765 and 798 nm were reported with both excitation wavelength over the whole time span, which contradicted the formation of the $P^+B_A^-$ intermediate. In this measurement the time resolution was not optimal (1-2 ps).

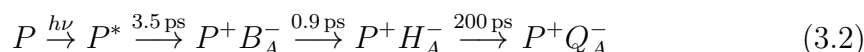
To understand the available experimental data, many theoretical contributions were made in the short time span from 1985 to 1988. The lack of evidence for a $P^+B_A^-$ intermediate step motivated the idea, that the electron should be transferred from the special pair to the pheophytin directly. Because of the fast charge separation rate and the large transport distance, it was clear that the electron transfer cannot be done with a direct coupling between these chromophores. **Marcus** [Mar87] analyzed two possible mechanisms which may lead to electron transfer on this time scale: (i) a superexchange mechanism with an indirect coupling from P to H via a virtual intermediate B and (ii) a two-step sequential electron transfer where the bacteriochlorophyll is directly populated. According

to his computations, the transfer rate for the two-step model could match the experimental values, whereas the superexchange model had 1000 times larger rates.

More accurate simulations were done by **Warshel, Parson and coworkers** [WP87, Cre88] using self consistent field/configuration interaction (SCF/CI) computations together with a multipole expansion beyond the point-dipole expression. They concluded that the energy of P^+B^- should be close to that of P^* , and could not exclude the formation of the $P^+B_A^-$ intermediate on the basis of energetic considerations.

Many other groups tried to find arguments against the two-step model [Mic88, Bix87, BMJ88, FS87, SF86, HM89]. In this process many new possible mechanisms were conjectured. The complexity of the system however does not allow to determine which of the above computations leads to the correct physical model.

First experimental confirmation of the two-step reaction model was done by **Holzapfel et al.** [Hol89, Hol90]. The system had 10 Hz repetition rate, 100 fs cross-correlation and excitation at 860 nm. The angles between cofactors and the ground state dipole moment of P were computed analyzing dichroic data. In particular, the computed angles were $\theta(B^-) = 36^\circ$, $\theta(H^-) = 68^\circ$ in good agreement with quantum chemical computations. Thus, the primary charge separation could be expressed as:



3.3.2 Chronology 1990-2013

The second set of publications contains a variety of disputes regarding the population of $P^+B_A^-$. Experiments done in this time interval are usually characterized by higher repetition rate which may exceed 1 kHz. New developments in the laser technology allowed to perform broad band spectroscopy with very good accuracy. The time resolution was also improved by means of excitation pulses with less than 100 fs duration. Many coherent oscillations were discovered, which overlapped with the ET process even at room temperature. This originated a revival of the adiabatic ET theory. It is important to notice that many of these results have very heterogeneous experimental conditions and data analysis, which could lead to considerable systematic errors.

Kirmaier et al. [KH91] repeated the measurements at room temperature with the same S/N ratio as Holzapfel et al. [Hol89]. In this case the sample was flowed through a 2 mm cell while cooled at 10 °C. The sequential model conflicted with wavelength dependence of lifetimes reported previously. A comparison plot was incorrectly done by plotting the data of Holzapfel et al. in a linear time scale although the measurements had a lin-log scale. Therefore differences in the 0.2-5 ps time window were claimed, and no direct population of the bacteriochlorophyll was detected.

Jortner and co workers [BJM91] analyzed the experimental data at room temperature and 10 K. Because at that time there was evidence of an intermediate state $P^+B_A^-$ only at room temperature, they proposed a model with a superposition of sequential two step and superexchange as a "peaceful coexistence of sequential and superexchange ET routes for the primary ET in the RC of some purple bacteria". Moreover, at room temperature the process was estimated to be non-adiabatic for rate constants $k \leq (250 \text{ fs})^{-1}$. Finally, the authors conclude that the occurrence of a parallel mechanism for the primary ET has a redundancy, which might be essential to ensure the prevalence of efficient ET in photosynthetic RC.

Vos et al. [Vos91] did measurements at 10 K and 100 K with 50 fs pulses at 870 nm. Two oscillations with period 700 fs and 2 ps were observed for *Rb. sphaeroides*. The oscillation features were the same when using broad or narrow excitation pulses. Stronger oscillations were observed in the mutant *Rhodobacter capsulatus* which has no pheophytin on the A-branch. The frequency range of the oscillations was 15-80 cm^{-1} , whereas the frequency of P^* vibrational modes was known to be larger (120 cm^{-1}). They concluded that the 2 ps mode could be coupled to the electron transfer, and therefore an adiabatic theory would be possible. This could also explain the weak temperature dependence of the charge transfer reaction.

Vos et al. [Vos92] did measurements at 10 K with 45 fs pulses at 870 nm for *Rb. sphaeroides* (R-26) and *Rhodobacter capsulatus* D_{LL} . The RC were kept open via prereduction of Q_A with 50 mM dithiothreitol. Measurements with R-26 showed the appearance of two absorption bands at $t = 0 \pm 50 \text{ fs}$ in the BChl-region, namely at 796 nm and 807 nm. Other two bands at 760 nm and 785 nm were also observed. In contrast to the 807 nm-band, which remains present at different delay times during the charge transfer process, the 796 nm-band disappeared already at ca. 500 fs. Kinetics of P^* could be fitted by a bi-exponential decay [0.9 ps (80 %) and 4.5 ps (20 %)]. The signal at 796 nm is modulated by damped oscillations with a period of ca. 0.65 ps and damping time of 0.8 ps. Also a fast kinetic with 90 fs was observed. At 805 nm the 90 fs component had an opposite amplitude than at 785 nm and 796 nm. Measurements with *Rhodobacter capsulatus* did not display the 796 nm-band. The authors concluded that a initial fast relaxation within the excited state P^* is present.

Hamm et al. [Ham93] did subpicosecond emission experiments at 10 Hz with 200 fs pulses. Contrary to absorption experiments, there was no interference with absorbance change of long lived ground state intermediates. The data cannot be explained by a monoexponential decay. Two time constant were found with 7 ps and 2.3 ps. The amplitude of the 7 ps was 4x smaller than the 2.3 ps. They concluded that the 3.5 ps time constant from absorption experiments is an average value of this new decay constants. They proposed that this biexponentiality may come from heterogeneous RC. These time constants were also confirmed by Arlt et al. [Arl93] by measuring the absorbance change of the B^- -band at 1016 nm where none of the pigments P, B, H and H^- absorb.

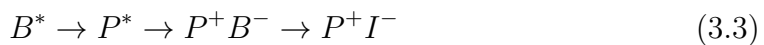
Marchi et al. [Mar93] estimated the different electronic diabatic surfaces by computing probability distributions and autocorrelation functions for the energy gaps between the surfaces. In contrast to Warshel et al. [WP87] they did not consider the non-polar hydrogens and the strong polarity coming from the surrounding water molecules. The simulation predicted a nearly activationless forward reaction within a superexchange mechanism.

Vos et al. [Vos94] did experiments at room temperature and 30 fs excitation pulses at 870 nm with 30 Hz repetition rate. Oscillations were observed at 938 nm with a main vibrational peak at 145 cm^{-1} , in good agreement with the measurements at 10 K. Their interpretation of the data concluded that at room temperature the P^* state is not thermally relaxed and that the short lived $P^+B_A^-$ would be unlikely. Their conclusion was that non-adiabatic ET is inappropriate, because of the observed coherence.

Schmidt et al. [Sch94, Sch95] did measurements with 150 fs pulses and 50 Hz repetition rate at 870 nm using parallel polarization between pump and probe beams. They modified the RC to have pheophytin-a instead of bacteriopheophytin-a with a purity of 95 %. The energy $G(P^+H_A^-)$ was raised to reach the free energy of $G(P^*)$. The reaction was described by a rate equation system. Using the principle of detailed balance the free energy difference between charge transfer states was investigated. They found that the B-band at 1020 nm was increased, leading to a larger population of $P^+B_A^-$. The authors concluded that $G(P^+B_A^-) < G(P^*)$, thus contradicting the superexchange model. The values for the difference free energy were set to $\Delta G(P^*) = 0$, $\Delta G(P^+B_A^-) = -450 \text{ cm}^{-1}$, $\Delta G(P^+H_A^-) = -2000 \text{ cm}^{-1}$.

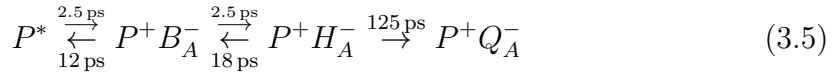
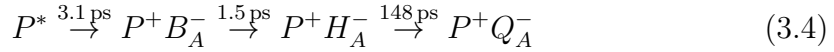
Maiti and Hochstrasser et al. [Mai94] did measurements in the $1560\text{-}1960 \text{ cm}^{-1}$ region. They used 300 fs pulses centered at 870 nm with 5 kHz repetition rate. They observed a shift of the 1682 cm^{-1} to 1702 cm^{-1} in 2.5 ps. The measured anisotropy at the 1702 cm^{-1} band was 0.19, which could be assigned to the P_M 9-keto carbonyl. This signature corresponded to the formation of $P^+H_A^-$. At 1665 cm^{-1} a 0.9 ps time constant was found, indicating a B_A^- band.

Beekman and Grondelle et al. [Bee95] did experiments using excitation pulses at $\sim 600 \text{ nm}$ with a cross-correlation time of 200 fs. The RC were pre-reduced with 200 mM sodium ascorbate. In the 880-960 nm region they found the time constants $\tau_1 = 4.1 \text{ ps}$ and $\tau_2 = 16 \text{ ps}$. On the other hand, in the 960-1060 nm region the observed kinetics were $\tau_3 = 200 \text{ fs}$, $\tau_4 = 1.8 \text{ ps}$, $\tau_5 = 5 \text{ ps}$. It was assumed that τ_1 and τ_2 described the relaxation of P^* under heterogeneity, whose time constant using a monoexponential fit was given by τ_5 . The kinetic τ_4 was then related with the formation of P^+B^- . The fastest kinetic τ_3 should be related to the energy transfer $B^* \rightarrow P^*$. The final stage of the model was described as some unknown intermediate due to the reduction of Q.



Hamm et al. [Ham95] did time resolved infrared measurements at 12°C in the spectral range 1000-1800 cm⁻¹. The excitation was done at 870 nm with a very high energy of 1 μJ using 1 kHz repetition rate. The cross-correlation was measured to be 400 fs. A positive band at 1666 cm⁻¹ and a negative at 1638 cm⁻¹ were measured for P^* corresponding to a 9-keto C=O mode of P. Global fit led to time constants $\tau_1 = 3.8$ ps, $\tau_2 = 240$ ps. The fast kinetic (0.9 ps) was not observed. No oscillations of P^* could be measured due to experimental uncertainty.

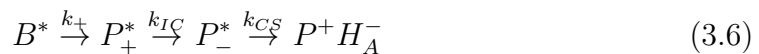
Holzwardt et al. [HM96] did measurements at room temperature with excitation at 860 nm, repetition rate 3 kHz and ca. 100 fs pulses. The polarizations were set at magic angle. Data analysis was done using global fit and target analysis of a given kinetic model. Fitted time constants were $\tau_1 = 1.5$ ps, $\tau_2 = 3.1$ ps, $\tau_3 = 147$ ps, $\tau_4 = \infty$, $\tau_5 = 10.8$ ps. The spectral shape of τ_3 and τ_5 were very similar but not equal. They explained the wavelength dependence of lifetimes reported by [KH91] in spite of this non-exponential decay of P^* . This could be understood in term of a mixing of these new decay constants. Tested kinetic schemes were:



The authors concluded that the reversible model is more than a small correction to the pure forward model. With this rate constants they computed a very small energy gap $G(P^*) - G(P^+ H_A^-) = -1058$ cm⁻¹. They claimed that this low energy gap may explain the non-exponential behavior and modifies all fast lifetimes even without change in any of the forward reaction rates.

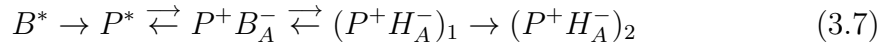
Woodbury and co workers [LTW96] did absorption experiments with a very high repetition rate of 3.8 MHz and excitation at 6 different wavelengths. Excitation of H showed a lifetime of H^* less than 30 fs, which contradicted the non-adiabatic model. The authors concluded that the electron transfer is not described by Marcus theory, rather by an adiabatic ET. Moreover, evidence of vibrational relaxation in P^* in the stimulated emission was observed. Fitted time constants were $\tau_1 = 0.5$ ps, $\tau_2 = 2$ ps, $\tau_3 = 14$ ps. In conclusion the amplitude of the 14 ps time constant discarded the hypothesis of a possible heterogeneity of the RC.

Jonas and Fleming et al. [Jon96] excited the 805 nm band directly with a cross-correlation of 25 fs using 5 kHz repetition rate. The data was recorded in the time range -300 fs to 2 ps. Fitted time constant were $\tau_1 = 120$ fs, $\tau_2 = 2.3$ ps. The 100 fs time scales involved suggested that the ET is at least partially electronically coherent. They observed quantum beats (125 and 227 cm⁻¹) with near zero anisotropy. The authors concluded with the following kinetic model and $\tau_{B^* \rightarrow P_+^*} = 80$ fs. Either B or P_+ could be excited.



Streltsov and Shuvalov et al. [Str97] did measurements with native and B_M -modified RC at room temperature with a time resolution of 45 fs, excitation at 865 nm. Treated RC had a loss of the B_M contribution at 800 nm. The RC were kept open by adding sodium-ascorbate. Oscillations with frequencies 31 cm^{-1} and 170 cm^{-1} were found at 805 nm. These were assigned to oscillations related with the accessory Chlorophyll B_A . They proposed that the 31 cm^{-1} mode is selectively coupled to the electron transfer. This was modeled by a modified adiabatic potential surface of P^* and $P^+B_A^-$ with a reversible return to the P^* state, thus an adiabatic electron transfer.

van Stokkum et al. [Sto97] did experiments with excitation at 800 nm and 250 kHz repetition rate within the time range -1 ps to 50 ps. The RC were reduced with 100 mmol/L sodium ascorbate. Fitted time constants were $\tau_1 = 0.18$ ps, $\tau_2 = 1.9$ ps, $\tau_3 = 5.1$ ps, $\tau_4 = 22$ ps, $\tau_5 = \infty$. The ~ 0.2 ps time constant had an intense bleaching around 810 nm, thus corresponded to $B^* \rightarrow P^*$. The 5.1 ps corresponded to primary charge separation. The 1.9 ps had a strong amplitude at 775 nm and 1010 nm, thus corresponded to $P^* \rightarrow P^+B_A^-$. They assumed a second charge separation state $(P^+H_A^-)_2$ and proposed the full kinetic scheme:



Spörlein and Wachtveitl et al. [SZW98] did measurements at room temperature using 60 fs excitation pulses at 870 nm and 20 Hz repetition rate. The polarization of the excitation was parallel to the probe pulse. They observed a non-adiabatic ET behavior at later times, which explained the exponential behavior of the process. At early time some adiabaticity could be present and oscillations may take place. One main contribution at 135 cm^{-1} was found for all wavelengths $\lambda > 920$ nm. A smaller oscillation with 40 cm^{-1} was superposed for $\lambda > 1030$ nm. No strong modulation of $P^+B_A^-$ was observed, indicating a weak connection between vibrational motion and ET. The oscillations could be explained as a single wave packet like modulation on the excited state surface of P^* . At this time it was not clear why only one vibrational motion should contribute to the oscillations since in principle P^* has many.

Vos et al. [VJM98] studied the coherent oscillations at 15 K with excitation at 880 nm using 30 fs pulses. Polarizations were parallel and magic. The traces of SVD were analyzed separately, and only the largest 10 SV were considered. Many components at 70, 94, 125, 156, 195 and 335 cm^{-1} were observed. The oscillations were described using a semi-classical model of wave packet motion on a harmonic potential energy surface. The different oscillation frequencies presented a phase jump in the vicinity of 925 nm, however not at the same position. The 125 cm^{-1} was probably due to sum or difference frequencies of the fundamental frequency near the center of the band. The 70 cm^{-1} was different than the others. It did not reflect a wave-packet motion on P^* . The authors concluded that this vibrational

mode is coupled to the ET. Furthermore it was conjectured that it may be related with the electrochromic shift of the B-band, reflecting the formation of $P^+H_A^-$.

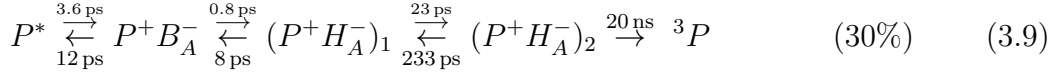
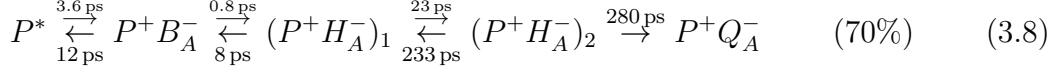
van Brederode and Grondelle et al. [Bre99] did experiments at 77 K with excitation at 796 nm and 880 nm. The model was assumed irreversible sequential with an intermediate state P^+B^- . Excitation at 796 nm showed a strong bleaching of the B band even after 600 fs. Thus the process $B^* \rightarrow P^*$ did not occur within 200 fs. Fitted time constant were $\tau_1 = 0.18$ ps, $\tau_2 = 1.7$ ps, $\tau_3 = 710$ ps, $\tau_4 = \infty$; other kinetics were difficult to resolve. A strong spectral evidence of a $P^+B_A^-$ state was present, but no kinetic was resolved. Also, $P^+B_A^-$ could be populated directly from B^* . The authors concluded that the processes $B^* \rightarrow P^*$ and $B^* \rightarrow P^+B_A^-$ may be adiabatic, whereas $P^* \rightarrow P^+B_A^- \rightarrow P^+H_A^-$ could be non adiabatic.

Spörlein and Wachtveitl et al. [Spö00] did measurements at room temperature with different modified RC. The excitation was the same for all samples at 870 nm. A biexponential decay for P^* was observed. For WT samples $\tau_{1a} = 2.3$ ps, $\tau_{1b} = 7$ ps with amplitude ratio $a_{1a}/a_{1b} = 2.4$. For vBChl-RC instead $\tau_{1a} = 25$ ps, $\tau_{1b} = 3.2$ ps with amplitude ratio $a_{1a}/a_{1b} = 0.42$. A fast time constant was observed at 1022 nm for all samples: $\tau_2^{WT} = 1.1$ ps, $\tau_2^{vBChl} = 0.9$ ps. For vBChl/Phe-RC an additional time constant $\tau_3 = 100$ ps was necessary at 1022 nm, indicating a long lived $P^+B_A^-$. By using a non-adiabatic ET it was possible to compute $\Delta G(P^+B_A^-) = +270 \text{ cm}^{-1}$ for vBChl-RC, thus $P^+B_A^-$ was above P^* .

Fingerhut et al. [FZV08] used evolutionary algorithms (covariance matrix adaptation evolutionary strategy) to optimize the initial charge transfer in reaction centers. The rate γ_{chem} (coupling to the energy storage system) and charge separation energy ΔG_{RC} were used as input parameters for the optimization run. The parameters d_{ij} (chromophore distance) and ΔG_{ij} were optimized by the evolutionary algorithm for a fixed number of chromophores. Simulations for *Rb. sphaeroides* led to quantum efficiencies $\Phi = 98\%$ close to the experimental values. The second ET step was found to have the fastest time constant $\tau_{23} \sim 0.7$ ps. Moreover the quantum efficiency barely depended on τ_{23} , but is strongly depended on the number of chromophores. It was shown that at least an energy difference $\Delta G_{RC}^{min} = 0.25 \text{ eV}$ is required to assure efficient charge separation. The resulting optimal values were $\eta_{max} \sim 33,5\%$ for $\Delta G_{hv} = 1.34 \text{ eV}$ (925 nm) with $\Delta G_{RC}^{opt} = 0.28 \text{ eV}$.

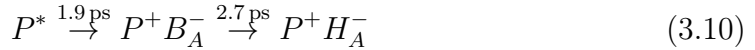
Pawlowicz and Louise Groot et al. [Paw08] did measurements at room temperature in the mid-IR between 1600 and 1800 cm^{-1} . The excitation was done at 600m, 805 and 860 nm with a repetition rate of 1 kHz. The ubiquinones Q_A were chemical removed. They used no reference probe, and the measured noise was removed by SVD-filtering. Fitted time constant under global and target analysis were $\tau_1 = 0.1$ ps, $\tau_2 = 3.8$ ps, $\tau_3 = 16$ ps, $\tau_4 = 4$ ns, $\tau_5 = \infty$. The relaxation of $P_+^* \rightarrow P_-^*$ was observed as well as $B^* \rightarrow P_-^*$. A multi-exponential decay of P^* was observed with an increase in $P^+H_A^-$ in the time scale of 20 ps. No evidence of 3P

upon 3 ns was found. The mid-IR absorption spectrum of $P^+B_A^-$ was described using the following model:



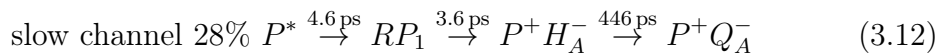
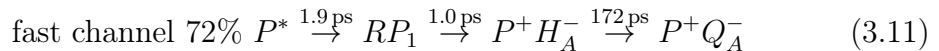
Fingerhut et al. [FZV09] extended the previous model ([FZV08]) by considering non-ideal activated electron transfer ($\Delta G + \lambda \neq 0$) and the dielectric of the surroundings at room temperature. Optimization of the charge separation steps led to $\tau_{12} = 1.8 \text{ ps}$, $\tau_{23} = 0.9 \text{ ps}$ with a quantum efficiency $\Phi_{RU} = 95.4\%$. Tolerated perturbation from activated case have $|\Delta G_{12} - \lambda_{12}| < 40 \text{ meV}$ and $|\Delta G_{23} - \lambda_{23}| \sim 120 \text{ meV}$. This implicated that the dielectric environment must assure a low reorganization energy λ_{ij} . Next the influence of antenna sizes was tested by using different gain factors (amplification of the excitation photon flux). The efficiency limit of antenna systems with gain factor 10^2 was $\eta = 24.4\%$, where RU alone had $\eta_{RU}^{opt} = 33.5\%$. The author concluded that the optimization of antenna system is possible up to efficiencies $\eta \sim 21 - 27\%$.

Kakitani and Koyama et al. [Kak10] did experiments with excitation at 870 nm with 0.1 μJ and 1 kHz repetition rate in the time range -1 ps to 30 ps. The whitelight continuum was generated with the fundamental wavelength at 800 nm and then the region around 800 nm was blocked with a notch filter. They used global and target analysis using only the first 4 singular values. Fitted time constants were $\tau_1 = 1.9 \text{ ps}$, $\tau_2 = 2.7 \text{ ps}$, $\tau_3 = 200 \text{ ps}$. Following model was proposed:



Moreover, a strong emission negative signal at 920 nm was observed in the computed absorption cross-section of $P^+B_A^-$. This was interpreted as a reverse charge recombination process.

Zhu and Louise Groot et al. [Zhu13] did measurements with excitation at 870 nm at magic angle and 1 kHz repetition rate. The data was analyzed using global and target analysis. Fitted time constants were $\tau_1 = 3.2 \text{ ps}$, $\tau_2 = 1.3 \text{ ps}$, $\tau_3 = 201 \text{ ps}$, $\tau_4 = \infty$. The model presented in [Kak10] was rejected. The second intermediate state RP_1 was interpreted as a mixture of $P^+B_A^-$ and $P^+H_A^-$. This model could not reproduce completely the data, thus they assumed a heterogeneity of the sample and analyzed it with a branched model.



3.4 Recombination processes and chemical modification

In section 3.1 we have explained the recombination process of RC which are embedded in their natural environment inside the photosynthetic unit. This cannot be achieved when exciting isolated reaction centers which do not have a cytochrome in the vicinity. As a result, the charge separated state $P^+Q_A^-$ can mainly relax to the ground state by electronic recombination as shown in figure 3.6-a.

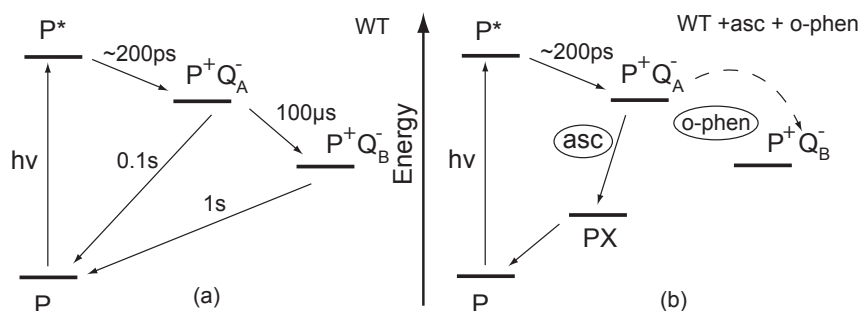


Figure 3.6: Recombination rates of charge transfer states in reaction centers for the wild type strain (a) and chemical treated with ascorbate and ortho-phenanthroline (b).

The recombination of an unmodified sample usually takes place from the state $P^+Q_B^-$, leaving the sample photoinactive for a couple of seconds [Feh89]. This process is very long when compared to repetition rates of 1 kHz (or higher) used in modern laser systems. Commonly, most of the experiments do not have a sufficiently large quantity of RC to provide a fresh sample at every excitation, as it may be expected in view of the complicated isolation procedure.

To avoid accumulation of RC in the $P^+Q_B^-$ state, it is possible to treat the sample using organic compounds such as sodium ascorbate and ortho-phenanthroline (figure 3.6-b).

Sodium-ascorbate is a salt originated from the reaction between sodium hydroxide (caustic soda) and ascorbic acid (Vitamin C). At room temperature it possesses a high solubility in water, making it suitable for biological applications. Indeed it has an important role in photosynthesis since it acts as an alternative electron donor for the photosynthetic unit [Tót09]. In particular, the oxidized special pair present in $P^+Q_B^-$ can be reduced, therefore allowing further photochemical processes by excitation at 865 nm.

Ortho-phenanthroline is a heterocyclic organic compound with iron chelator properties. In other words, it can react with the iron radical present in the RC giving a double coordinate bound. It has a very small water solubility which makes it difficult to dissolve in TRIS-solution in which the RC are present. The effect of ortho-phenanthroline is to inhibit the electron transfer between both ubiquinones [HB74]. At high concentrations (10 mmol/L) it can remove one or both ubiquinones [OIF75, MOF90].

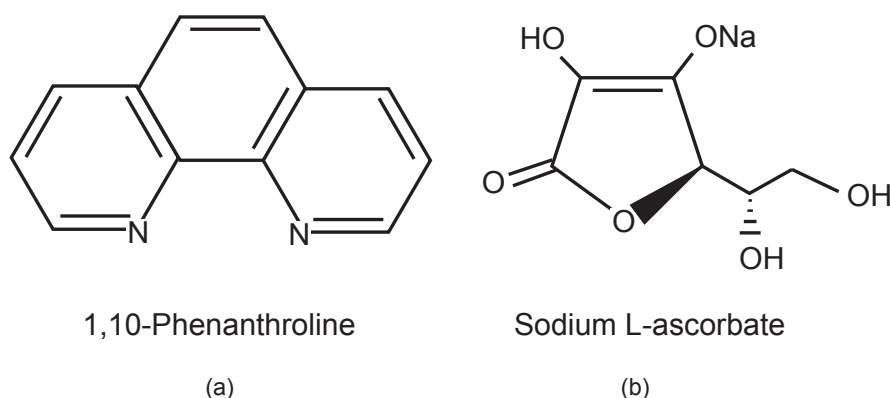


Figure 3.7: Chemical structure of sodium-ascorbate (a) and ortho-phenanthroline (b).

The combined action of these two chemicals can be summarized as follows:

- The ortho-phenanthroline avoids the generation of $P^+Q_B^-$, which means that the longer relaxation time is not 1 second, rather 0.1 second coming from $P^+Q_A^-$.
- The sodium-ascorbate donates an electron to the oxidized special pair in the photoproduct $P^+Q_A^-$ before the electron sitting in the ubiquinone recombines. The reduction of the special pair makes the RC photoactive again and avoids the accumulation of non-absorbing molecules at the excitation wavelength 865 nm. It is not yet clear what happens after a new excitation of this system, namely the system could fall into a state PX where the special pair is in the ground state and one or many cofactors, as well as their protein environment, are not in their original conformation.

In section 5.2.3 we will discuss the possible alterations on the charge separation steps originated from the previous chemicals. The hypothesis of a unnatural behavior of the primary reactions in RC will be tested by reducing the excitation rate of the experiment to 50 Hz. The lower exhaustion of the sample, together with

an efficient exchange of illuminated molecules, allows the RC to naturally recombine before a new photoreaction is started. Under these new experimental conditions the measurements can be performed without implementation of sodium-ascorbate and ortho-phenanthroline.

3.5 Final remarks and status quo

In this final section we will summarize the many aspects regarding the purple bacteria *Rb. sphaeroides* known to this date. First of all, the primary reaction steps in bacterial RC can be considered as a prototype for all photosynthetic energy conversion devices. The well defined absorption bands of the pigments involved in the charge separation process facilitates the identification of the intermediate states using pump-probe techniques.

Second, the many contributions presented in the past two decades have still three main conflicting points: (i) existence of a fast (~ 1 ps) kinetic involved in the ET, (ii) the role of coherent effects in the charge transfer process and (iii) the possible adiabaticity of the process.

Last but not least, artificial reduction of the RC allows experiments with high excitation rates by avoiding accumulation of inactive species. In this case the large number of measurements performed leads to high signal-to-noise ratio and very smooth data. However the high levels of exhaustion may produce new effects which are not relevant for natural photosynthesis.

In chapter 4 we will describe the pump-probe experiment used in this thesis. The system was prepared and optimized to produce accurate measurements with low excitation rates (50 Hz) and also high excitation rates (500 Hz). By reducing the excitation rate of the experiment it is possible to study the RC without additional chemicals. At this point a detailed study of the alterations originated from these and other similar chemicals becomes mandatory, because a large number of publications in this field refer to measurements done under homologous artificial conditions. Therefore eliminating possible sources of systematic errors will allow us to discuss the conflicting points for the primary steps in bacterial photosynthesis under physiological conditions.

4 Experimental set-up

The science of light fascinated mankind since primordial times. It was however only in the middle of the 17th century that it became possible to fabricate high quality optical instruments to study light phenomena more closely. The possibility to create and manipulate coherent light at ease, started by the first laser in 1960, facilitated the introduction of laser technologies in practically all scientific disciplines.

Goal of this chapter is to describe the current experimental tools used in measurements of reaction centers from *Rb. sphaeroides*. The development and optimization of the present experiment had very important contributions from Matthias Himmelstoß [Him12], Jeff Michelmann [Mic13] and Florian Lehner [Leh14].

4.1 Sample preparation

In this section the elaboration of different compounds necessary for this thesis will be explained. As standard procedure the CW-absorption of all samples was controlled before and after each measurement using a commercial spectral photometer LAMBDATM 750 from *Perkin Elmer*.

The laser dye IR132 (Lambdachrome) dissolved in di-methyl sulfoxide (DMSO) was used as calibration molecule. It has an absorption band with maximum at 834 nm, thus it can also be excited at the same wavelength used for the reaction centers (865 nm). The extinction coefficient at the absorption maximum is approximately $\varepsilon(834 \text{ nm}) = 160\,000 \text{ Lmol}^{-1} \text{ cm}^{-1}$. The concentration was adjusted to have an absorption of 0.4 OD/mm at the excitation wavelength. A detailed study of this infrared dye can be found in [Str13].

The reaction centers from *Rb. sphaeroides* wild-type (strain 2.4.1) were isolated using standard purification procedure by A. Gardiner and R. Cogdell at the University of Glasgow [Dom14]. Phototrophically grown cells were washed with a MES/KCl buffer (20 mM MES, 100 mM KCl, pH 6.8) and re-suspended in 20 mM Tris.Cl at pH 8.0. The RC were solubilized using 0.25 % LDAO. A final purification with a 35-40 % ammonium sulphate precipitation eliminated the remaining LH2 complexes. For the measurements, the RC were dissolved in a TL buffer (20 mM Tris.Cl, 0.1 % LDAO at pH 8.0). At the excitation wavelength the sample has an extinction coefficient of $\varepsilon(865 \text{ nm}) = 115\,200 \text{ Lmol}^{-1} \text{ cm}^{-1}$ and the absorption cross-section is $\sigma(865 \text{ nm}) = 4.4 \cdot 10^{-16} \text{ cm}^2$. A total amount of 10 ml with two different concentrations was available for all measurements. The concentration of

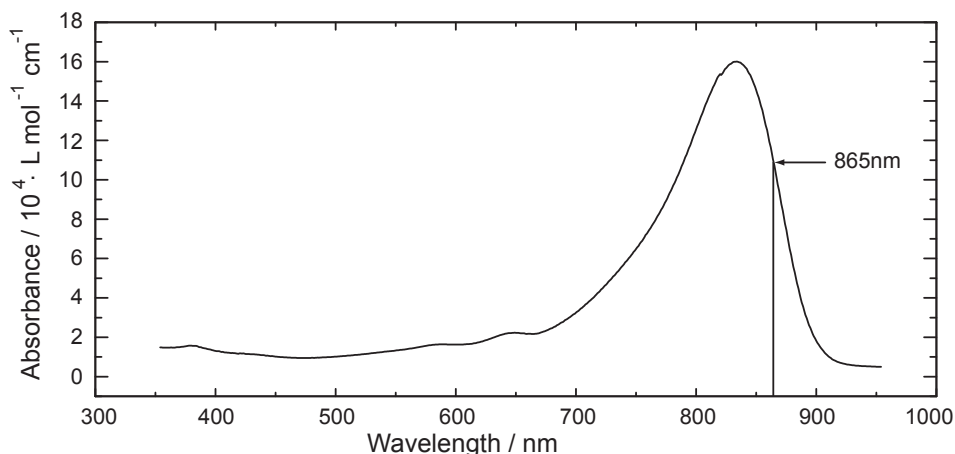


Figure 4.1: Absorption spectrum of the calibration laser dye IR132 in DMSO.

the first 5 ml solution was adjusted to have an absorption of 1 OD/mm, for the other half 0.4 OD/mm.

For some measurements, the reaction centers were also treated with ascorbat and ortho-phenanthroline. In this case the buffer solution had 10 mmol/L ascorbat and 1 mmol/L ortho-phenanthroline. They were prepared adding 30 μL of a stock solution with 0.11 mol/L ascorbate and 0.01 mol/L ortho-phenanthroline into the cuvette containing 300 μL of the sample. The stock solution was prepared mixing 22 mg sodium ascorbate and 2 mg ortho-phenanthroline into 1 mL TRIS-buffer.

Three related variables were used to describe the exhaustion of the sample in pump-probe experiments. In general, a high sample exhaustion has to be avoided because it may lead to non-linear effects or even irreversible damage. This could be controlled with the energy of the excitation beam and the corresponding beam diameter at the cuvette. The concentration of the sample had also a small influence, since saturation effects are more evident at low concentrations where the number of molecules is smaller.

The *photon density* ρ is defined as the number of excitation photons per square centimeter at the cuvette. In the present experiments a constant excitation energy of 60 nJ was used. The diameter of the excitation beam was set to 300 μm . As a result the photon density was fixed to $\rho = 3.7 \cdot 10^{14} \text{ cm}^{-2}$.

The number of *photons per molecules* describes how many photons will be in average absorbed by each molecule in the excitation volume. It can be computed as the product $\rho_{\text{abs}} \cdot \sigma$ of absorbed photon density and absorption cross-section.

Finally the *exposed sample* is defined as the percentage of the excited molecules at the excitation volume. It can be computed as the quotient between absorbed photons and number of molecules in the excitation volume.

Concentration RC	Absorption @ 865 nm	photons per molecule	exposed sample
37 $\mu\text{mol/L}$	0.4 OD/mm	0.1	10 %
87 $\mu\text{mol/L}$	1 OD/mm	0.15	6 %

Table 4.1: Absorption parameters for RC from *Rb. sphaeroides*. The photon density was set to $3.7 \cdot 10^{14} \text{ cm}^{-2}$.

Thus, using a low excitation energy of 60 nJ it was possible to excite less than 10 % of the molecules present in the excitation volume. This value is acceptable when using an adequate stirring mechanism as described in section 4.2.3.

4.2 Pump-probe setup

The light source for the time resolved measurements was a commercial femtosecond pulsed laser system (Clark-MXR CPA-2001, 1 kHz repetition rate, pulse duration 150 fs, 1 mJ pulse energy at 772 nm). The short pulses were generated in an additive pulse mode locking fiber oscillator with 37 MHz repetition rate and had less than 100 pJ per pulse (for a theoretical description see [IHL89]). Output energies of about 1 mJ/pulse were achieved using a *chirped pulse amplification* (CPA) technique [SM85]. The gain medium in the amplification cavity was a Titan:Sapphire crystal which was pumped by a YAG laser. A circulating bath (VWR 1162A) was capable to thermally stabilize the laser system to 20 °C. The humidity inside the laser was kept below 5% using a continuously dry-air-flushing system.

The energy fluctuations were analyzed using a photodiode connected to a triggered current integrator (Wieserlabs, WL-IPD4 2010). A fraction of the full energy was measured at every single pulse, denoted as e_i . The fluctuation analysis considered the energy deviation over $n = 500$ pulses. The *long term fluctuations* $\sigma_{long}^{(rel)}$ was computed as the relative standard deviation of the values $\{e_i\}_{i=1}^n$. Likewise the *short term fluctuations* $\sigma_{short}^{(rel)}$ was given by the relative standard deviation of $\{\delta_i\}_{i=1}^{n/2}$, where $\delta_i := e_{2i-1} - e_{2i}$ was the energy difference between two consecutive pulses.

$$\sigma_{long}^{(rel)} := \frac{\left(\sum_{i=1}^n (e_i - \langle e_i \rangle)^2\right)^{1/2}}{\sqrt{n-1} \cdot \langle e_i \rangle} = 0.4 - 0.6\% \quad (4.1)$$

$$\sigma_{short}^{(rel)} := \frac{\left(\sum_{i=1}^{n/2} (\delta_i - \langle \delta_i \rangle)^2\right)^{1/2}}{\sqrt{n/2-1} \cdot \langle \delta_i \rangle} = 0.1 - 0.2\% \quad (4.2)$$

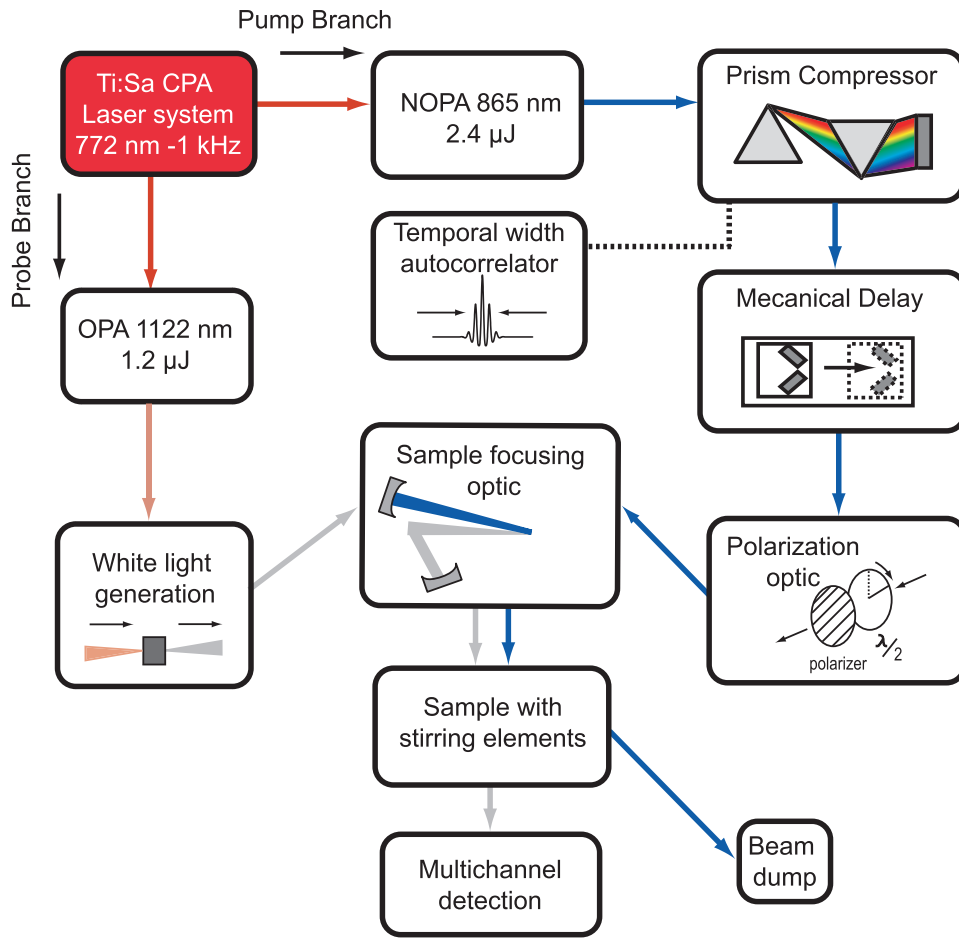


Figure 4.2: Schematic representation of the pump-probe setup. The experiment is divided into a pump branch and a probe branch.

Sixty percent of the laser output was used for the time resolved measurements. This energy was split into two branches used to generate the pump and probe pulses (see fig. 4.2). After a series of intermediate steps, both pulses were focused on the sample. In this experiment all metallic reflecting optics used silver coating because of its improved reflectivity in the near-infrared (NIR). Finally the pump pulse was captured and eliminated by a beam dump (in this case an aperture) while the probe pulse was measured in the spectrometer. Integrating over a large number of excitation cycles enhanced significantly the signal-to-noise ratio of the measurement without any loss in time resolution. The evolution of the dynamical processes after photoexcitation of the sample was registered by changing the delay time between pump and probe pulse using a mechanical delay stage.

4.2.1 Excitation pulse

The excitation pulse at 865 nm was generated using a self made *non-collinear optical parametrical amplification* (NOPA) device based on currently available technology described elsewhere [Rie00]. A simple theoretical description was already presented in section 2.3. The incoming laser beam at 772 nm and energy 275 μJ was reduced in diameter and collimated by Telescope 1 using two thin lenses with focal length +100 mm and -50 mm. A beam splitter separated the pulse sending 90 % of the incoming energy to the *second harmonic generation* (SHG) branch (fig. 4.3 upper part). Using the birefringent crystal *beta barium borate* (BBO) with phase matching angle $\theta = 30^\circ$ and 0.6 mm thickness it was possible to convert the 772 nm red photons into more energetic 368 nm blue photons. The rest of this branch had purely reflective optic with dichroic mirrors HR400. One periscope lowered the propagation height of the new blue photons while filtering the remaining undesired red photons. A spherical mirror allowed to focus the blue beam into a second BBO with $\theta = 28^\circ$ and 1 mm thickness.

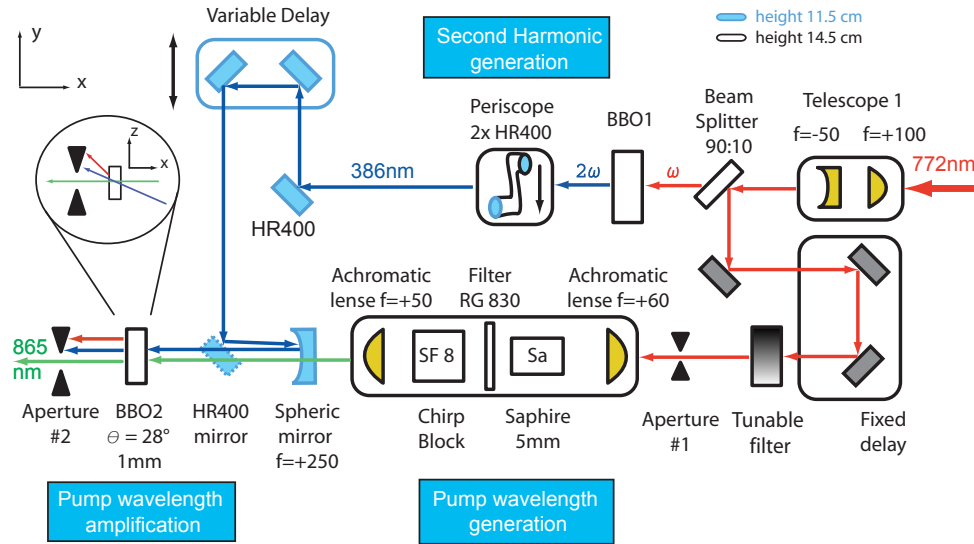


Figure 4.3: Schematic representation of the NOPA setup.

The remaining 10% of the incoming energy was used to generate the desirable wavelength (fig. 4.3 lower part). First, a fixed delay corrected the difference in path length with respect to the SHG branch. Second, one achromatic lens with focal length 60 mm focused the beam into a 5 mm Sapphire crystal. One tunable gray filter in combination with a small aperture were used to modify the energy and numerical aperture of this convergent beam. Adjusting these two parameters correctly it was possible to widen the spectrum and to generate photons in the

desired region of 865 nm via continuum generation [BBR09]. Undesired visible and 772 nm photons were eliminated using a long-pass filter RG830. A Flint glass SF8 (10 mm) introduced a spatial chirp in the pulse and consequently reduced the amplification bandwidth of the NOPA. In other words the spectral shape at the output was narrowed, however it was still broad enough to allow short pulses. The last component was an achromatic lense with focal length 50 mm which focused the beam in the BBO2.

Both pulses were spatially and temporally overlapped in BBO2. In order to amplify the 865 nm photons it was necessary to tilt the crystal to obtain the correct phase matching condition. In the amplification process an idler beam at 697 nm was also generated. For safety reasons the idler was blocked as soon as possible to avoid reaching the eye of the experimenter.

The output energy of the NOPA pulse centered at 865 nm was 2.4 μJ with a spectral width of 25 nm (fig. 4.5-a). The temporal width of the outgoing pulse was approximately 200 fs. The long term standard deviation over 500 pulses had the value $\sigma_{long}^{(rel)} = 0.7\%$. On the opposite side, the pulse-to-pulse energy deviation was $\sigma_{short}^{(rel)} = 1.5 - 2.0\%$ (see equations (4.1) and (4.2)).

Pulse compression

Using a two prism geometry it is possible to generate a negative chirp which reduces the temporal length of a positive chirped pulse [DP82]. After the generation stage, the positive chirped NOPA pulse was mapped to the prism compressor using Telescope 2. The beam was adjusted to have its minimal diameter at the end mirror after both prisms (see fig. 4.4). The beam diameter was adjusted to be smaller than 5 mm. The maximal transmission efficiency of the whole prism compressor was 64% and the output energy of the compressed pulse was 1.53 μJ .

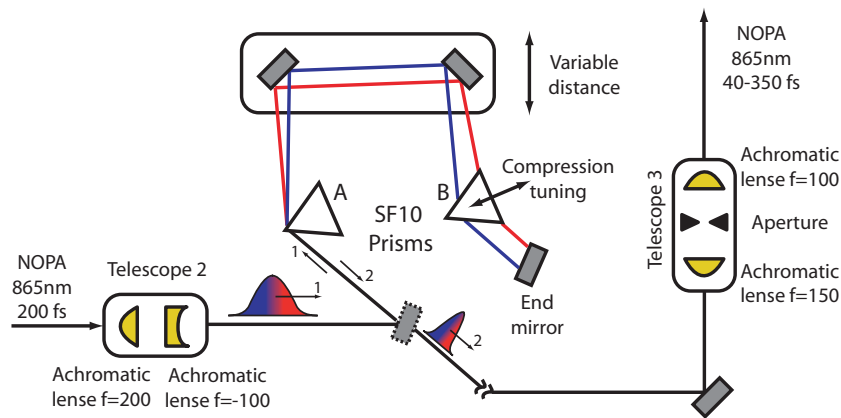


Figure 4.4: Schematic representation of the prism compressor setup.

The prisms were made of flint glass SF10 which is very dispersive in the NIR-spectral region. A Brewster angle was adjusted at every glass surface to avoid reflection losses. The incoming beam (1) was reflected by a mirror into the first prism. The end mirror changed the propagation direction of the returning beam (2) in order to overcome the half mirror. In this geometry, the red spectral components had a longer optical path than the blue components, therefore the temporal width of the pulse was reduced.

Using Telescope 3 it was possible to collimate the beam and reduce its diameter by 33%. An aperture was placed in the focal plane between both achromatic lenses to eliminate non-gaussian beam profile components. Using a standard autocorrelator [Koz04] it was possible to measure the temporal width of the pulse after this telescope and to adjust the compression by shifting prism B. The shortest pulse possible had 40 fs, nevertheless all experiments used pulses with 175 fs (fig. 4.5-b).

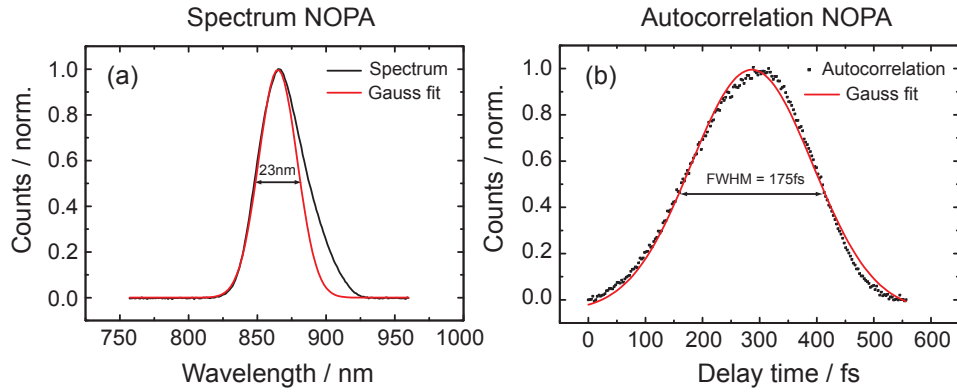


Figure 4.5: Spectrum of the excitation pulse centered at 865 nm (a) and autocorrelation after the prism compressor (b).

Delay Stage

The compressed pump pulse was coupled to a mechanical translation unit with 30 cm displacement (Physik Instrumente, M-531DD), thus changing the temporal delay with respect to the probe pulse. Using two different retro reflectors, a moving horizontal reflector at the translation stage and one vertical reflector fixed outside the unit, it was possible to use four times the displacement length to generate a maximal delay of 4000 ps. A stepper motor generated a minimal rotation step which determined a transverse displacement of 0.1 μm . In the previously described fourfold geometry it corresponded to a delay of the pump pulse of 0.4 μm , equivalent to 1.33 fs.

4 Experimental set-up

The *time zero delay* was determined when both pump and probe pulses reached the sample at the same time. One reference measurement with the sample in the ground state was recorded at -2 ps, while the proper experiment started at -1 ps. Until +1 ps the variation of the time delay was performed linearly with a step width $\beta = 23$, equivalent to 30.7 fs. In other words, the number of moving steps at the n -th position was given by:

$$S_n = S_0 + n \cdot \beta \quad 0 \leq n \leq N_{lin} \quad (4.3)$$

with a number of linear displacements N_{lin} . At later times, the translation was done exponentially using a *logarithmic scale factor* $\alpha = 0.136$ until a total number of displacements N_{tot} :

$$S_n = S_0 + N_{lin} \cdot \beta + (n - N_{lin}) \cdot e^{\alpha(n - N_{lin})} \quad N_{lin} + 1 \leq n \leq N_{tot} \quad (4.4)$$

The configuration of all delay parameters used in this experiment can be found in the following table:

	step units	time units
Reference measurement	-1500	-2 ps
Experiment start	-750	-1 ps
Experiment end	-	3485 ps
Stepwidth (β)	23	30.7 fs
Linear delay displacements N_{lin}	65	-
Total delay displacements N_{tot}	121	-

Polarization optic

The different kinds of dichroic measurements use a specific configuration of the mismatch polarization angle between pump and probe beam, as described in section 2.4. This could be adjusted using two polarization elements in the pump branch since the polarization of the probe beam was always parallel to the optical table.

First, a $\lambda/2$ plate rotated the polarization direction of the pump beam. In this case we used a narrow bandwidth wave plate at 865 nm which did not modify the propagation direction of the pulse. If instead a broad bandwidth wave plate was used, a shift in the propagation of the pulse could be observed. This could lead to a loss in spatial overlap with the probe pulse at the cuvette.

Second, a thin *wire grid polarizer* determined the polarization of the beam. This was commonly set to be parallel or perpendicular to the probe beam as well as at the magic angle configuration. Together with the $\lambda/2$ plate it adjusted the energy of the transmitted beam.

4.2.2 Probe pulse

In the present experiment it was necessary to probe the sample at all wavelengths between 450-1050 nm. The technical difficulties which were present in the generation of a white light continuum over an octave could be overcome by dividing the spectral range into three different regions: The *BLUE continuum* spanned over 450-600 nm, the *VIS continuum* was used between 550-950 nm and the *NIR continuum* covered the 900-1050 nm region. They were all produced using a 5 mm YAG crystal since it has a high yield in the NIR ([BBR09] and Fig. 4.6).

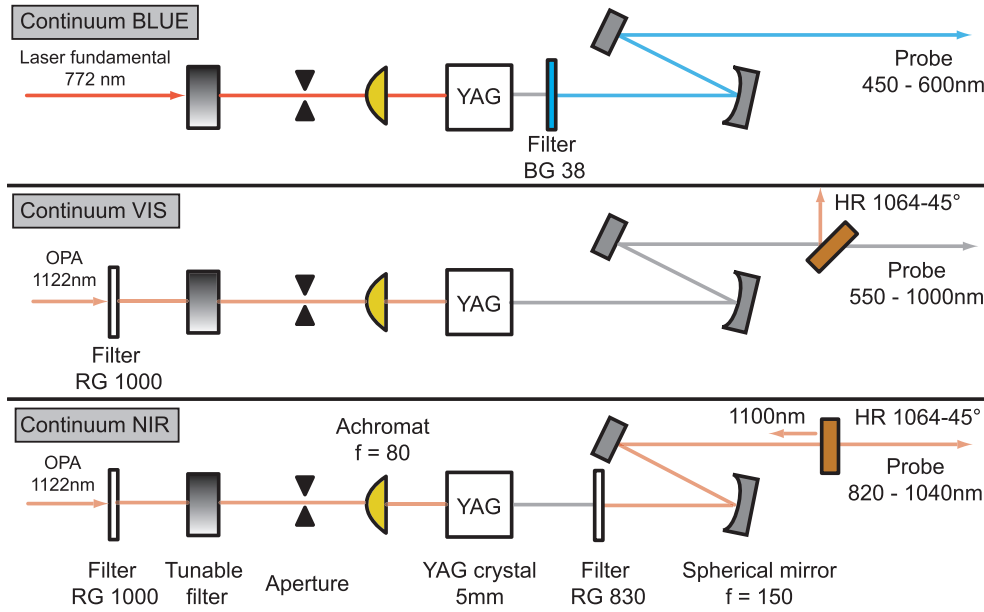


Figure 4.6: Different types of continuum generation.

The *BLUE continuum* was generated by focusing the laser fundamental beam at 772 nm into the crystal. This produced a strong white light in the blue and visible spectrum, but it was not efficient in the NIR. The strong fundamental beam was then filtered out using a BG38 filter.

The generation of *VIS continuum* required an intermediate step which is the generation of a NIR-beam at 1122 nm using a self made OPA. A full description can be found elsewhere [Him12]. The OPA was adjusted by analyzing the produced white light. By varying the wavelength and the intensity of the beam it was possible to achieve a better continuum which may be stable in different but not all wavelength channels. The remaining energy of the OPA pulse after the continuum generation as well as unstable NIR-wavelengths were eliminated using a dichroic mirror HR1064-45°.

The *NIR continuum* used a similar configuration of the *VIS continuum*. In this case however the visible components were eliminated by a red filter RG830 and the OPA was adjusted such that particularly the NIR wavelengths had low fluctuations. Tilting the dichroic mirror it was possible to change the cutoff edge to longer wavelengths which were more stable than in the previous case.

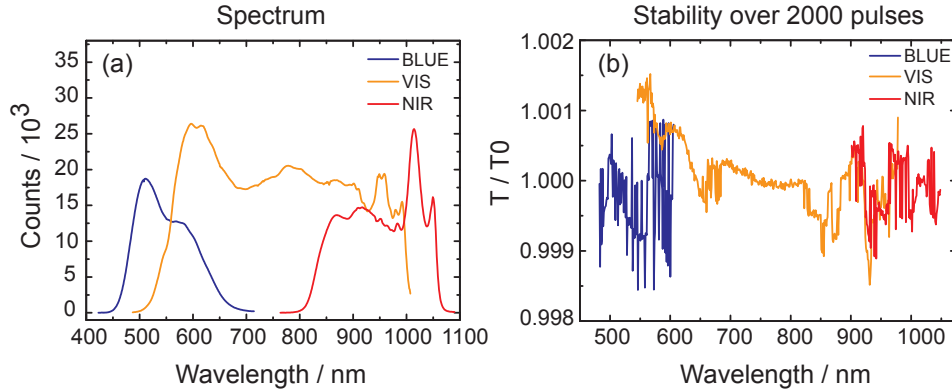


Figure 4.7: Spectrum of different types of white light continuum (a). Measured pump-probe signal without sample, averaged over 2000 pulses (b).

The combination of these three different types of white light continuum generation allowed measurements over the complete desired spectral region, each of them having a satisfactory stability. In fact, each wavelength of the detected probe beam had more than 10000 counts in the photodiode array (fig. 4.7-a), which improved the detection limit caused by the shot noise in the electronic components of the detection. In addition, the measured pump-probe signal without sample, averaged over 2000 pulses, deviated at most 1 % from the expected value $T/T_0 = 1$ (fig. 4.7-b). Equivalently it could detect transmission changes $\Delta T/T = 10^{-3}$. It is important to notice that the detection efficiency was optimized in the region between 700 - 800 nm, where it is possible to detect changes $\Delta T/T < 10^{-4}$.

4.2.3 Sample focusing and stirring elements

The final part of the pump-probe experiment was the focusing of both beams in the sample. The excited and probed volume in the cuvette had to be the same at all measured delay times in this setup. The variation of the delay time via the delay stage generated a small shift of the focus of the pump beam. To avoid an overlap loss, it was convenient to adjust the pump focus to be twice larger than the probe focus in the sample. In this case, the complete probed volume was always excited even if the pump spot was moved.

The probe beam was focused using a concave spherical mirror with focal length $f = 250$ mm (curvature radius $r = -500$ mm) and afterwards reflected to the

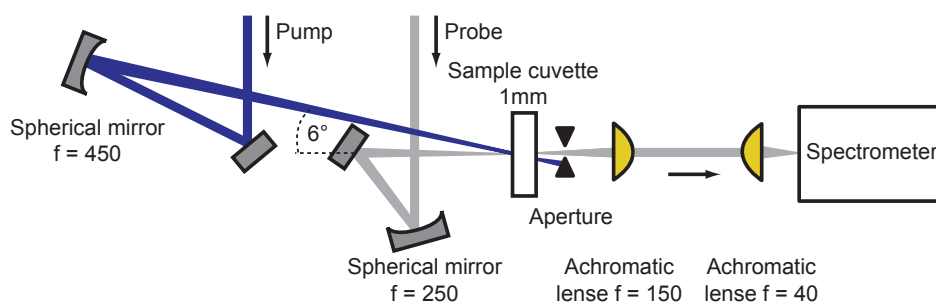


Figure 4.8: Focusing optic. All mirrors had silver coating.

sample. The position of the cuvette was located at the waist of the probe beam. The geometry of the spherical mirror generated a small astigmatism which could be observed with a beam profiling camera. Moving the position of the beam profiling camera it was possible to search for the location at which the beam became symmetric, corresponding to the beam waist at the focus. In the present configuration the diameter of the probe beam at the sample was $120\text{ }\mu\text{m}$ and coincided with the beam waist.

The pump beam was reflected on a concave spherical mirror with focal length $f = 450\text{ mm}$ (curvature radius $r = -900\text{ mm}$). The distance between mirror and sample was adjusted to have a beam diameter of $300\text{ }\mu\text{m}$ at the sample. After the cuvette the beam was captured by a half closed aperture.

An angle of 6° was present between the propagation direction of pump and probe pulses. Therefore, a spatial overlap at the sample was ensured over more than 1 mm . The probe beam and the generated pump-probe signal were then collimated by an achromatic lens with $f = 150\text{ mm}$. They were further coupled to the spectrometer with another achromatic lens $f = 40\text{ mm}$.

The next topic of this section deals with the exchange of molecules within the cuvette (Hellma type 110-QS, $350\text{ }\mu\text{L}$). Because of the small amount of available sample it was not possible to use a standard flow cuvette device which would pump new molecules into the excitation volume after each pulse. In other words, we were forced to develop an exchange mechanism using a closed 1 mm cuvette. In this way we were able to perform the experiments with a small volume of only $300\text{ }\mu\text{L}$ of RC for each measurement.

The flow exchange system resulted as a combination of two different mechanisms: First, it was necessary to ensure that the molecules did not get excited by two successive pump pulses. In this case a fast exchange mechanism was required. Second, it was necessary to avoid inhomogeneities in the sample, especially of molecules which had not reached the ground state, thus achieving a good reference measurement when the excitation pulse was blocked. This required a slow exchange mechanism.

The fast exchange mechanism was achieved by translational motion. The cuvette and cuvette holder were displaced in a circular path with 8 mm diameter which was orthogonal to the optical axis of the probe beam. By means of this small diameter we could ensure that the pump and probe beams always reached the inner part of the cuvette without contact with the boundary. The rotation was produced by a coupled DC-motor (Faulhaber 2230-012 S, 8000 rpm) with a gear ratio of 97.3:1, whose final rotation frequency was 1.4 Hz. The resulting velocity of a single molecule inside the cuvette was 0.035 m/s. This value was four times lower than the 0.15 m/s needed to ensure complete volume exchange after 2 ms, which was the time interval between two subsequent excitation pulses at the excitation rate of 500 Hz. For this reason some measurements required to lower the excitation rate of the system to 50 Hz (see section 4.2.4).

Because the laser system had 1 kHz repetition rate, the time between excitation measurement and reference measurement was 1 ms. In this time interval, a single molecule could be displaced 50 μm away from the excitation beam which was adequate for excitation diameter of 300 μm since it ensured similar conditions between both sampled volumes.

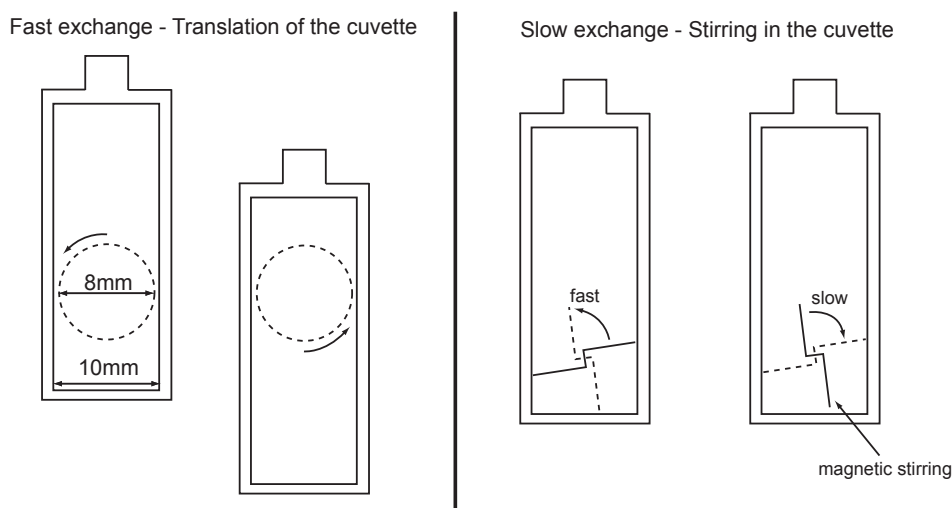


Figure 4.9: Exchange mechanisms. For description see text.

The slow exchange mechanism was composed of a slow internal drift of the molecules produced by a magnetic stirring. In combination with the rapid motion of the cuvette, the slow stirring ensured a global homogeneity even to volumes where no direct excitation occurred. A self made metallic stirring built from magnetic wire with 0.5 mm diameter and 5 mm length (Stahlbecker Germany, 1.4310, X10CrNi18-8) was encapsulated in a 15 mm PTFE tube with inner diameter 0.5 mm and outer diameter 1 mm. The extremities of the tube were closed using a hot iron and

stretched longitudinal after heating with a hot air pistol until the whole element had the right size to fit into the cuvette. Two equally long 5 mm wings were then bended asymmetrically up to 90 degrees, forming a Z-shaped stirring. The resulting element was slightly larger than the cuvette width and it was only able to perform a quarter of a revolution. Using a Neodymium magnet attached to an independent DC motor (Conrad elektronik, 2.3 Hz) the magnetic wire was turned slowly from the vertical to the horizontal position. When both extremities reached the cuvette walls, the stirring stopped moving and maintained its position until the polarity of the magnetic field was flipped. The resulting magnetic force moved the stirring very fast to the original vertical orientation. An overall zigzag motion was generated which catapulted the molecules to the top of the cuvette with a mean velocity of 0.01 m/s.

4.2.4 Chopper and shutter

This section describes the beam blocking devices. In the experimental set-up two different types were implemented, namely the optical chopper and the mechanical shutter.

First, two optical choppers (New Focus, model 3501) were used to produce blocking frequencies between 50-500 Hz. They consisted of a rotating aluminum wheel with a periodic number of apertures. In particular, this model allowed to adjust the rotation phase, which improved the synchronisation of the chopper with the laser. The chopper 1 was placed in the pump branch and blocked every second excitation pulse. Since the laser system had 1 kHz repetition rate, this chopper worked with 500 Hz. The chopper 2 was used to reduce the repetition rate of the pump-probe experiment as requested for some measurements. It was placed at the end of both pump and probe branches and could completely block both beams simultaneously. The rotation frequency was 50 Hz with a duty cycle of 2 to 20. For this chopper a new self made asymmetric wheel was constructed having an opening of 36°. The size of this opening was chosen to allow transmission of two consecutive pulses, the first with excitation and the second with the excitation blocked by chopper 1. Due to this asymmetric construction, the rotational movement had a considerable drift leading to a phase instability. This was observed with the spectrometer as a periodic vanishing of the continuum spectrum. Solving this problem by mechanical means was not possible, the *defect* pulses were analyzed with the measurement software and discarded.

Second, two self made mechanical shutters were implemented, each one placed at the respective branch. Their implementation allowed to prevent an over-illumination of the sample. They were built using a servo-motor (Modelcraft, model Mini-Servo WG-90MG) with a black carton attached to the rotating axis. The controlling electronic was self assembled and programmed using a micro-controller (Atmel, model Atmega8). After each illumination of the sample (analogously *illumination*

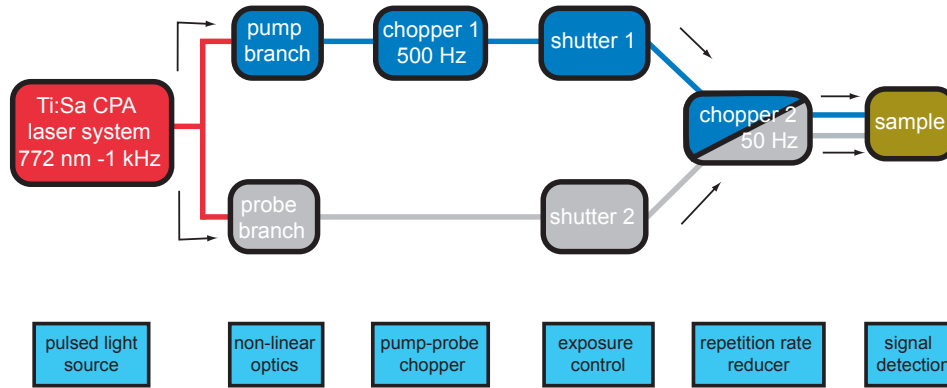


Figure 4.10: Disposition of chopper and mechanical shutter in the pump-probe experiment.

time, see section 4.3.1) the shutters were closed, therefore avoiding an unnecessary exposure when the electronic devices are still busy and are not ready for a new acquisition. Moreover, at the end of one measurement the shutters remained closed for 1 s to facilitate the relaxation of the sample.

4.2.5 Spectrometer and detection

The spectral decomposition and analysis of the probe beam was performed using a grating spectrometer coupled to a photodiode array which is synchronized with the laser system. The beam was focused into the spectrometer slit using an achromatic lens with focal length $f = 40$ mm and had a diameter of approximately $32\text{ }\mu\text{m}$ (figure 4.8).

The spectrometer (Princeton Instruments, model Acton SP2300) was built in a Czerny-Turner configuration and had a grating with 150 lines/mm which is blazed for 800 nm. The photodiode array consisted of a NMOS Linear Image Sensor (Hamamatsu, S8380-512Q) with 512 silicon pixel. Each pixel had a width of $50\text{ }\mu\text{m}$, thus the spectral resolution was not influenced by the geometric imaging of the beam into the diodes. To calibrate the assembly of spectrometer and photo-array we used a Rubidium lamp which has many sharp lines in the 600-1000 nm region.

One spectral window of this detection did span 530 nm in the considered region, which was imaged into the 512 pixels of the photodiode. The resulting spectral resolution was then 1.04 nm, thus sufficient for measuring molecular processes of complex proteins.

Because the absorption properties of silicon is poor for NIR-wavelengths, as well as the diffraction efficiency of the grating, it was impossible to do measurements above 1100 nm. In this context it is important to choose the right coating for the diodes. Another detection that was tested in this thesis (Hamamatsu, S3902-512Q) had a very poor NIR-coating and produced less counts in this region, which made the measurements more difficult.

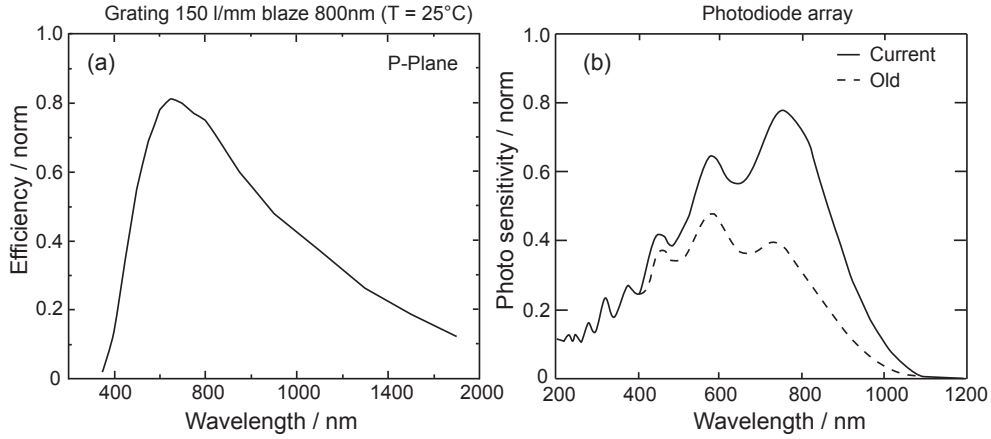


Figure 4.11: Approximated efficiency curves from grating (a) and photodiode array (b).

To conclude with, the diffraction of light at the grating may lead to the appearance of wrong signals in the detection when measuring in a broad spectral region. If we consider a grating with a line distance d and a incident angle θ_0 , then the diffraction maxima are given by:

$$d(\sin \theta - \sin \theta_0) = \pm n\lambda \quad (4.5)$$

where λ is the wavelength of the considered monochromatic wave and n is the diffraction order. Therefore the first diffraction order of λ coincides with the second diffraction order of $\lambda/2$ and both are measured at the same pixel of the photodiode array. This problem was solved by using three different measurement windows within one octave as described in section 4.2.2. It was also necessary to use filters to cut the spectrum of the probe pulse which lies outside the given window to avoid the appearance of these artifacts.

4.3 Software for measurement and data analysis

4.3.1 Acquisition software

The acquisition software for this experiment¹ was written using the C language and it was fully developed in the group of Prof. Zinth by Ingmar Hartl, Bernhard Schmidt, Stefan Laimgruber and Evelyn Plötz. Further development in the acquisition and analysis of the data was performed in this thesis and will be explained shortly.

The measurement was performed in a series of *scans*, each one corresponding to the acquisition of data for all desired delay time steps and twice the total sampling number (one corresponding to the forward, the other to the backward displacement of the delay stage). The sampling at each delay time step was divided into many packages called *measurement per step*, where each one corresponded to the acquisition of the signal over a predefined *illumination time*. Every *measurement per step* was analyzed and saved independently. In particular, two main algorithms were used to eliminate undesired signal spikes and slow energy drift present in the probe pulses as described below.

The *spikes correction algorithm* performed a statistical test over all registered shots in *measurement per step*. In the present experiment, a number higher than 100 shots for each excitation-reference modus was taken. The correction was done independently for each measured pixel of the photodiode array. After computing the mean value and standard deviation of the sampling, all measured shots situated *two standard deviations away* from the mean value were marked as *defect* and deleted. Later, the mean value and standard deviation of the *good* shots were computed and saved, whereas the values of each single shot were discarded to reduce the file size.

The *drift correction algorithm* improved the signal-to-noise ratio by compensating for the slow energy drifts present in the probe continuum. This could be alternatively increasing or decreasing. In particular, two different measurements as described in figure 4.12 would have a systematic deviation. Each transmission value was computed as the quotient over the averaged pulse signal:

$$T_1 := \frac{\sum_{i=0}^{N-2} E_i}{\sum_{i=0}^{N-2} R_i}, \quad T_2 := \frac{\sum_{i=1}^{N-1} E_i}{\sum_{i=0}^{N-2} R_i} \quad (4.6)$$

In this particular example T_1 would be lower than T_2 because the energy of the probe continuum would have drifted towards larger values and would not be compensated by referencing. The algorithm corrected this behavior by averaging

¹ rclh2mess.x, latest version 06.12.2013

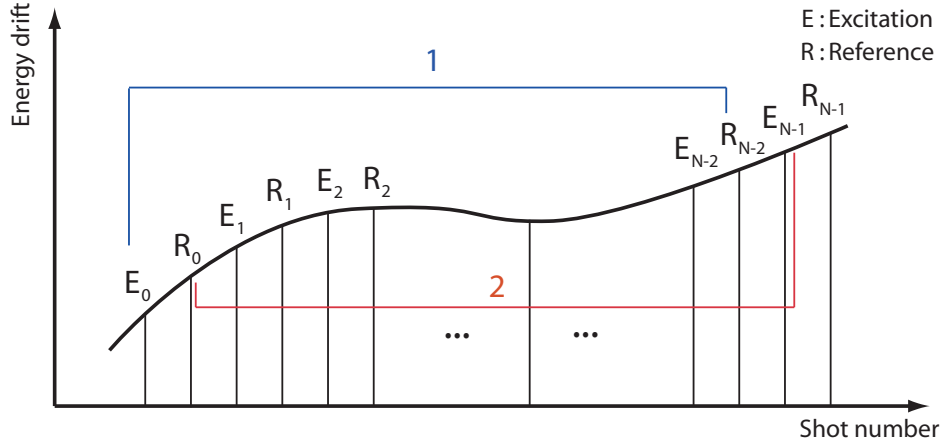


Figure 4.12: Slow energy drift of the probe continuum. In a pump-probe experiment the absorption of the sample is referenced after each excitation. In this example the mean energy drift over the excitation pulses is lower than the mean energy drift over the reference pulses.

the two transmission values. The ultimate transmission value $\langle T \rangle$ was computed as follows:

$$\langle T \rangle := \frac{T_1 + T_2}{2} = \frac{\frac{1}{2}(E_0 + E_{N-1}) + \sum_{i=1}^{N-2} E_i}{\sum_{i=0}^{N-2} R_i} \quad (4.7)$$

In summary, the drift correction algorithm computed the transmission signal as the averaged value over $N-1$ shots for the excitation and reference pulses. Moreover, the first and N th excitation pulses were averaged and the N th reference pulse was not considered.

4.3.2 Analysis software

All measured data was analyzed using a program written in the IDL5.4 language called *z20*, also developed at the institute. Several acquired scans were averaged and then converted into absorption change signal. Afterwards it was necessary to *calibrate the time zero* of each wavelength due to the presence of a temporal chirp in the pump and probe beams. This was conveniently done using a reference substance which had a strong signal and a very sharp signal rise, in this case the laser dye IR132 in the solvent DMSO. For the considered spectral interval the time zero deviation between 500 nm and 1000 nm was larger than 1 ps, thus of the same order of the kinetics to be measured. As a consequence a multiexponential fit of uncorrected data would have led to wrong results. All corrected data had a time zero which coincided for all wavelengths within 10 fs, i.e. much smaller than the time resolution of the experiment.

The multiexponential fit of the data was done using a routine written in C-language called *URMEL*² initially developed by Ingmar Hartl. Modifications were done to allow fitting of the coherent time zero artifacts (section 2.1.2) and target analysis (see section 2.8.1).

Finally, for the analysis and processing of the fitted spectra a *singular value decomposition and target analysis* was implemented in a *Wolfram Mathematica 10* worksheet.

4.4 Measurement specifications

In the last section of this chapter the specific configuration and preparation of the experiment will be described for the different types of measurements. All experiments were performed at room temperature (297 K). To check for the integrity of the sample one CW-spectra was taken after every measurement.

The first type were the *measurements at 500 Hz*. In this case the sample was used at two different concentrations: 0.4 OD/mm for measurements in the spectral region around 800 nm and 1 OD/mm for the remaining wavelengths. Because of chopper 1 the excitation rate was half the 1 kHz repetition rate of the laser. The chopper 2 was not used and remained static. The *illumination time* was set to 100 ms and the number of *measurement per step* was 20, leading to a total number of 2000 measured shots. These measurements did not have a rotating cuvette holder, therefore the exhaustion of the sample was higher. To avoid the accumulation of long-lived states, two cuvettes were alternately measured thus leaving half of the sample unexposed.

The second type were the *measurements at 500 Hz with reducing agents*. In this case the concentration of the sample was 0.4 OD/mm. Furthermore 10 mmol/L sodium ascorbate and 1 mmol/L ortho-phenanthroline were added as described previously to avoid long lived states. The *illumination time* was set to 100 ms and the number of *measurement per step* was 20. Stirring was performed as described in section 4.2.3.

The third type were the *measurements at 50 Hz*. In this case the concentration of the sample was 0.4 OD/mm. Using the chopper 2 it was possible to produce an effective repetition rate which was ten times smaller as before. Contrary to the previous cases, the *illumination time* was set to 500 ms and the number of *measurement per step* was 4, leading to a total number of 200 measured shots with the same scan duration. Moreover, a 3-point median filter on the time axis was performed to remove artifacts from scattering objects in the sample. Stirring was performed as described in section 4.2.3.

²German initials for "Unglaublich rasanter Marquardtalgorithmus mit externem Linearfit", latest version 24.09.2013

5 Results and Discussion

In this chapter we will present the results of the pump-probe experiments. At the beginning, the recorded kinetics of the calibration dye IR132 will be discussed since they were not found in the literature.

The successive sections deal with the proper measurements of reaction centers. Initially, the measurements performed with 50 Hz excitation rate will be discussed. An excitation rate of 500 Hz is used for the further measurements, in analogy with many recent publications. In this case significant deviations in the electron transfer kinetics are evident.

5.1 Calibration dye IR132

The measurements of the laser dye IR132 are shown in figure 5.1. The data displays a ground state bleaching around the excitation wavelength 865 nm and a broad excited state absorption between 500-700 nm. Also a strong stimulated emission can be observed at 940 nm, which partially overlaps with the ground state bleaching.

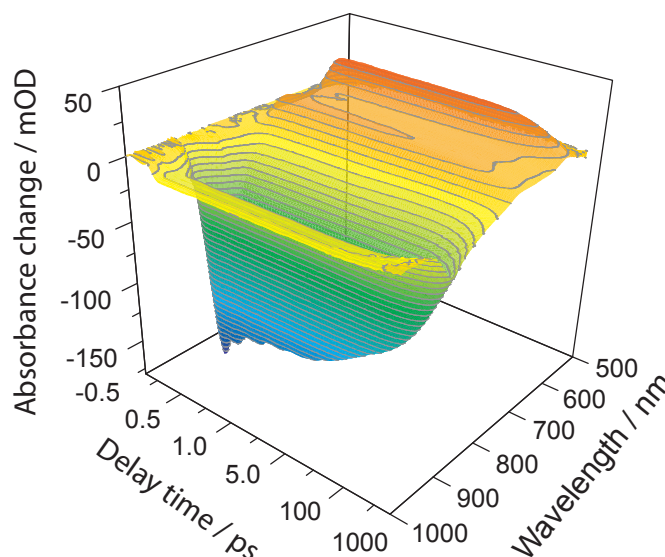


Figure 5.1: Dynamics of the laser dye IR132 in DMSO in a 3D-plot. The data is displayed at magic angle, computed using parallel and perpendicular dichroic measurements.

The data justifies the particular choice of this laser dye. The strong signal bleaching and stimulated emission, which exceed the 150 mOD at the current excitation energy (figure 5.2-a), makes it suitable for adjusting the experiment. Especially when the time and spatial overlap of pump and probe beams is poor, a partial signal can be identified in the spectrometer and allows further tuning of the experiment. Moreover, the signal rise at time zero is very sharp and coherent artifacts are not visible.

A satisfactory fit was obtained using three decay constants, namely 1.5 ps, 22 ps and 740 ps. They all present a very large amplitude around 865 nm, therefore they are related to relaxation processes. Similarities between the two short decay constants may indicate the presence of a non exponential kinetic, which can also be fitted by a bi-exponential decay. On the other hand, the largest decay constant is related to the relaxation of the stimulated emission.

Finally, the induced absorbance change vanishes after a couple of nanoseconds, thus the excited molecules relax to the ground state very fast. No accumulation effects were observed when using high repetition rates (500 Hz).

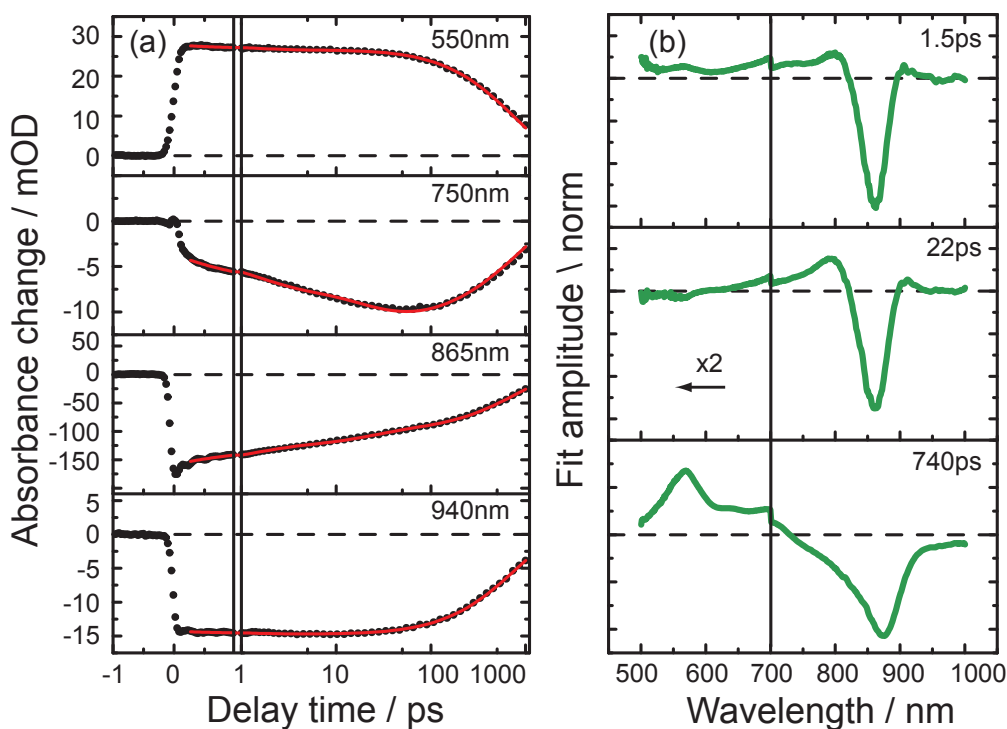


Figure 5.2: Time resolved data at characteristic wavelengths (a) and fit amplitudes for a three multiexponential fit (b), multiplied by 2 for wavelength below 700 nm . The data is displayed at magic angle, computed using parallel and perpendicular dichroic measurements.

5.2 Reaction centers

In this section we will present the time resolved measurements for the reaction centers from *Rhodobacter sphaeroides*. The analysis is focused on the dynamics present after 300 fs. For measurements at high repetition rate, the coherent artifacts at time zero will be modeled phenomenologically, but their interpretation will not be discussed. Moreover, the observed coherent oscillations will not be considered in this discussion since they have a negligible amplitude for times larger than 0.5 ps.

5.2.1 Measurements at 50 Hz

Broadband transient absorption measurements of reaction centers using 50 Hz excitation rate were recorded using the specifications given in section 4.4. These results have been recently published [Dom14]. Selected transients are displayed in figure 5.3-a. The main signatures are a ground state bleaching (GSB) at 865 nm, strong stimulated emission (SE) at 920 nm and a wide excited state absorption in the visible (450-700 nm) and near infrared region (1000-1060 nm). Weak absorbance change is already present 100 fs before the time zero, due to the limited duration of the pulses and the coherent artifacts. Four different transition phases can be identified:

- Phase 1 (After 0.3 ps): Strong bleach of the Q_y -band of the special pair P around 865 nm, stimulated emission around 920 nm and a very broad absorption with a narrow positive band at 810 nm. These features suggest the presence of an electronically excited state P^* .
- Phase 2 (about 1 ps): Absorption decrease in the BChl band at 800 nm, increased absorption at 1020 nm and around 600 nm. These features point to contributions from a BChl anion.
- Phase 3 (about 15 ps): Stimulated emission and features due to the anion of BChl have decayed. At that time one observes a bleach of the BPhe Q_x -band at 540 nm together with an absorption increase around 670 nm. These absorption features point to the presence of a BPhe anion H_A^- in this time range.
- Phase 4 (after 500 ps): At late delay times the features related to the BPhe anion decay, namely the 750 nm H-Band reached its minimum, the H-Band at 544 nm is recovered and 660 nm-band fully vanishes. The system represents the spectrum expected for the state $P^+Q_A^-$.

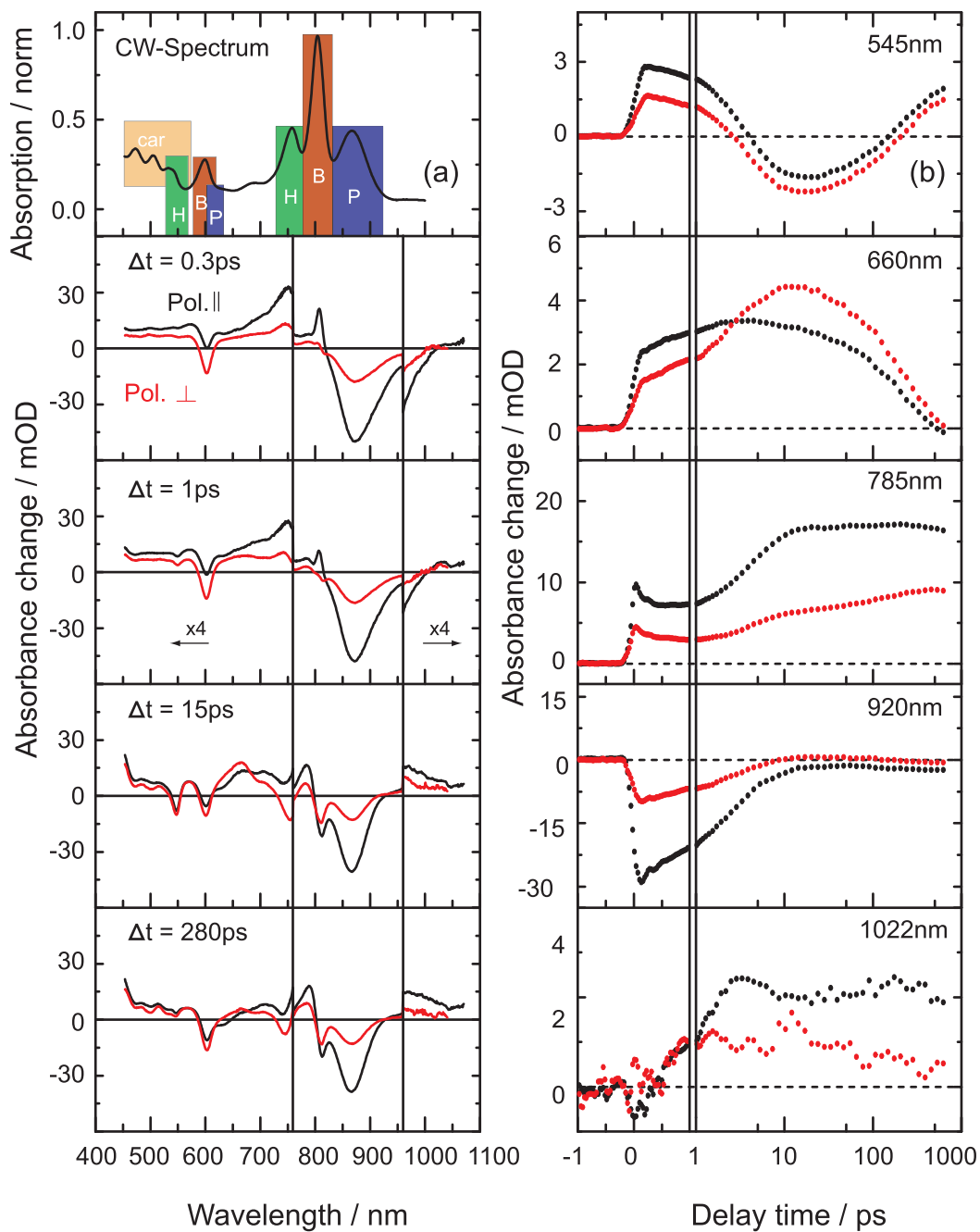


Figure 5.3: Transient and stationary spectra (a) and time evolution at the given characteristic wavelengths (b). Black data has parallel polarization and red data perpendicular. For the absorbance changes in figure (a) the wavelengths below 760 nm and above 960 nm have been multiplied by 4.

The time dependence of the absorption change at some characteristic probing wavelengths is shown in figure 5.3-b. They show the same kinetics as in previous publications [Hol, Hol90], with the difference that the data quality was considerable improved as well as the number of probing wavelengths. The measured kinetics can be described with a superposition of exponential functions for delay times Δt in the range $300 \text{ fs} < \Delta t < 1 \text{ ns}$. A first canonical fit evaluated the number of kinetic components. Four time constants were necessary for a satisfactory result. The obtained DADS are very smooth for wavelengths below 980 nm (fig. 5.4). Above 1000 nm the perpendicular measurements display a considerable noise, originating from low detection efficiency in this spectral region combined with a low signal amplitude.

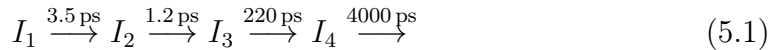
Confidence intervals for every time constant were obtained using an exhaustive search algorithm [Sat04]. Small absorption kinetics in the 1 ns range may reflect the change of the beam overlap at that very long delay time. For this reason the longest time constant was set to $\tau_4 = 4000 \text{ ps}$, which improved the fit quality.

Parallel pol.				Perpendicular pol.			
\parallel	best	min	max	\perp	best	min	max
τ_1	1.19	0.96	1.49	τ_1	1.12	0.84	1.51
τ_2	3.51	3.16	3.87	τ_2	3.54	3.18	3.89
τ_3	220	188	265	τ_3	223	201	257

Table 5.1: Confidence interval for each time constant evaluated using an exhaustive search algorithm for the parallel (left) and perpendicular (right) dichroic measurements. All entries are in ps.

The data was then inspected using singular value decomposition and target analysis (see section 2.8.2). At first it is desirable to estimate the number of primary singular values p . Using two different algorithms, first the autocorrelation analysis and second a MAD-test (see section 2.6.2), we computed $p = 4$. Nevertheless we will present an analysis using five SV to avoid information loss ($m = 5$). In this case the residual standard deviation is $\sigma_{rsd} = 0.105 \text{ mOD}$, which is of the same magnitude as the experimental error $\sigma_{exp} = 0.1 \text{ mOD}$.

The targeted model is assumed to be sequential without back-reactions:



Decomposed time traces after a singular value decomposition are shown in figure 5.5-a. They summarize the kinetic information present in the full data-set. In this case the largest singular value display mainly the most relevant components over the whole spectral range, such as the 3.5 ps, 220 ps and the 4000 ps kinetics. The fastest kinetic with 1.2 ps is clearly evident in the fourth singular value, where the other time constants have less contribution.

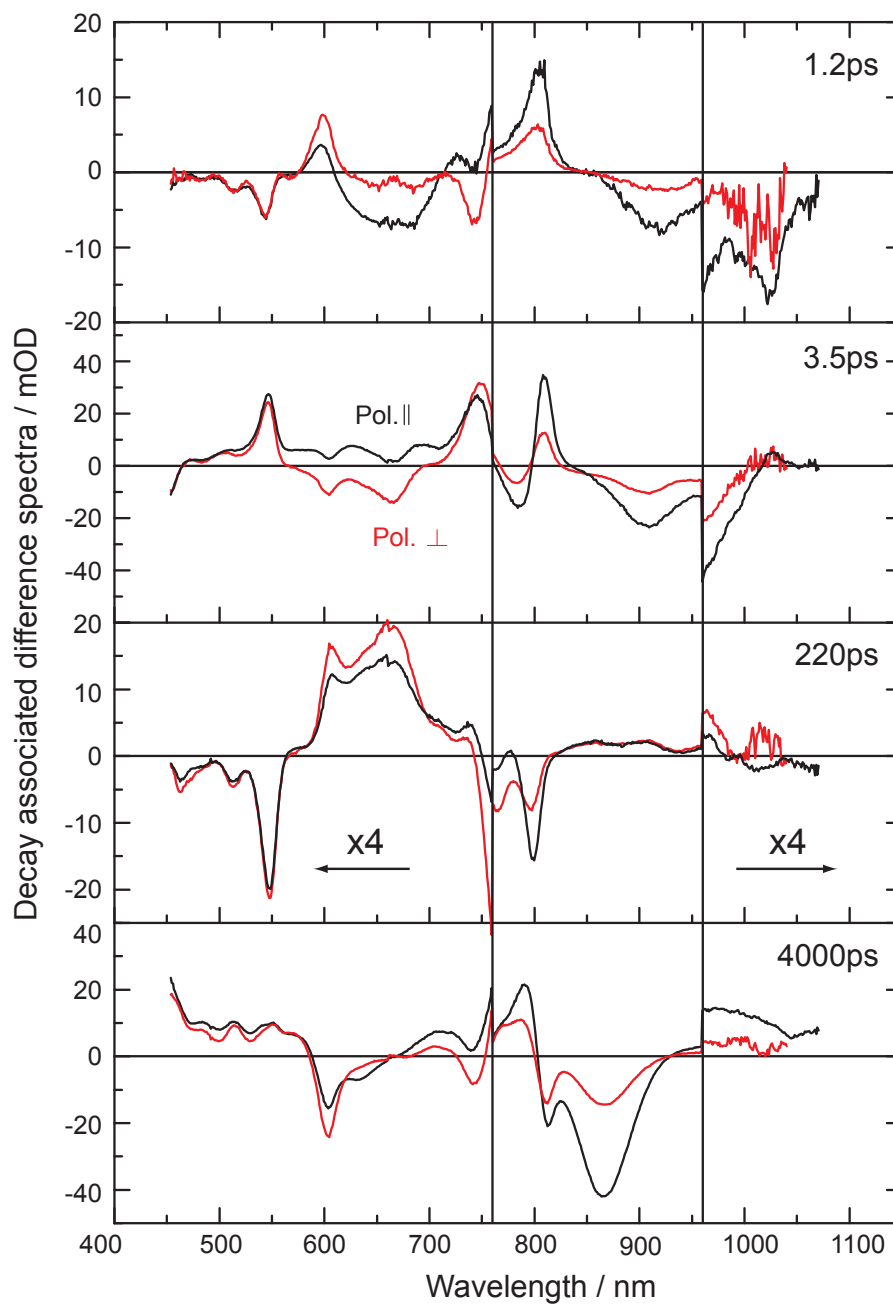


Figure 5.4: Decay associated difference spectra between 480-1060 nm. The wavelengths below 760 nm and above 960 nm were multiplied by x4. If the stimulated emission with time constant 3.5 ps is modelled by a bi-exponential decay (2 ps [85%] and 7 ps [15%]), the amplitude of the 0.9 ps kinetic is slightly changed. This however has little influence in the computation of the SADS.

Using a least chisquare fit it is possible to obtain the C-matrix coefficient for the parallel (C^{\parallel}) and perpendicular (C^{\perp}) measurements for this particular model. In the present case these are $p \times m$ matrices with only a reduced number of elements.

$$C^{\parallel} = \begin{pmatrix} -382.376 & -145.347 & -19.967 & 11.6695 & 0.0656623 \\ -200.396 & 210.29 & 113.058 & -74.5831 & -0.449469 \\ -258.102 & 103.382 & 16.3835 & 5.13413 & 0.0770358 \\ -261.173 & 87.7948 & -41.9089 & -5.06565 & -0.144272 \end{pmatrix} \quad (5.2)$$

$$C^{\perp} = \begin{pmatrix} -129.541 & -64.1464 & -8.60027 & -8.77759 & 0.247723 \\ -86.3432 & 83.0108 & 50.6756 & 54.9216 & -1.56232 \\ -93.0059 & 48.1931 & 16.3577 & -3.0181 & 0.0877409 \\ -102.623 & 29.5983 & -39.3931 & 2.31889 & -0.0676781 \end{pmatrix} \quad (5.3)$$

Using the reconstructed population vector (figure 5.5-b) it is possible to display the kinetic information which is not described by the model. The points represent the reconstructed populations whereas the solid curves are the exact solution of the underlying kinetic model. A qualitative analysis shows that all real populations (upper plots) perfectly match the targeted populations. Moreover, the error component E_1 (lower plot) has a noise-like behavior. A quantitative estimate can be achieved using the corresponding autocorrelation coefficients given in table 5.2. In this case the coefficient \mathcal{A}_5 is 20-30 % lower than the rest and does not reach the value 0.9, suggesting that no significant information is contained in E_1 .

coefficient	parallel	perpendicular
\mathcal{A}_1	0.97	0.97
\mathcal{A}_2	0.99	0.98
\mathcal{A}_3	1.00	0.99
\mathcal{A}_4	0.95	0.95
\mathcal{A}_5	0.79	0.65

Table 5.2: Autocorrelation coefficient for the reconstructed population vector. The last component \mathcal{A}_5 corresponds to the remaining information which is not described by the targeted model.

Finally, the SADS (fig. 5.6) were computed from the C-matrix by inverting equation (2.78). This leads to the following expression:

$$\Delta\sigma_i(\lambda_k) = \sum_{j=1}^m C_{ij} V_{jk}^t \quad (5.4)$$

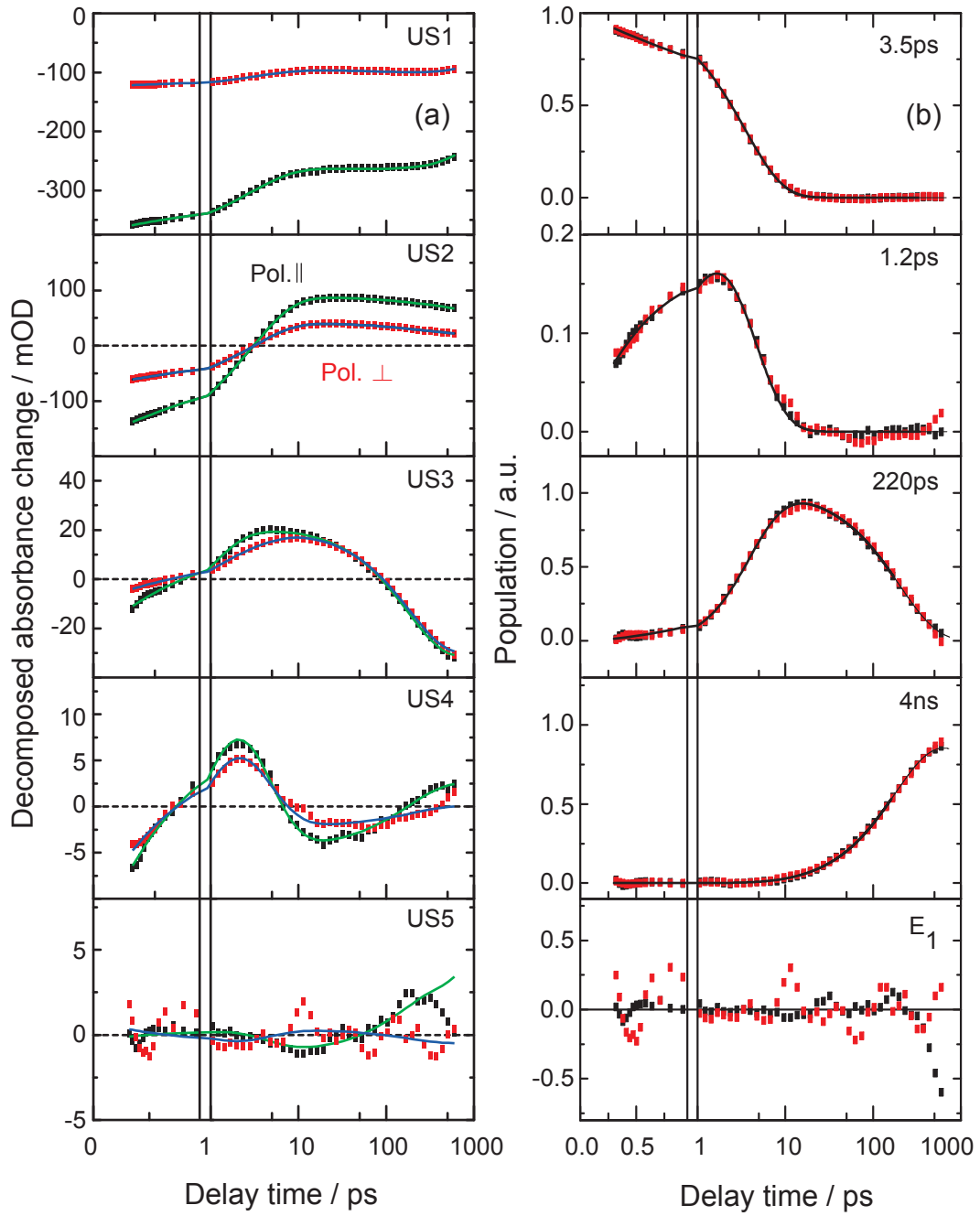
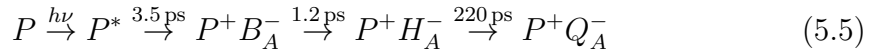


Figure 5.5: Decomposed absorbance for the first five $U \cdot S$ traces fitted with target analysis (a) and reconstructed populations vectors (b). Black points have parallel dichroism, red points perpendicular.

A detailed analysis of the absorption spectra for each intermediate state is presented below.

- The state I1 with lifetime 3.5 ps displays a bleaching of the Q_y -Band of P at 865 nm and SE of P at 920 nm, an ESA at 810 nm originating from the BChl of the special pair and a small ESA of the BPhe at 750 nm. Therefore it is possible to identify this state as P^* .
- The state I2 with lifetime of ca. 1 ps shows a bleaching of the accessory Q_y BChl-Band at 810 nm, a B^- -Band at 1022 nm and a bleaching of the Q_x P-Band at 600 nm. Therefore it is possible to identify this state as P^+B^- .
- The state I3 with lifetime of ca. 200 ps shows a bleaching of the Q_x H-Band at 544 nm and a decrease of the absorption at the Q_y H-Band at 750 nm. The 810 nm B-Band is blue shifted towards 780 nm and the Q_y and Q_x P-Bands are bleached. Therefore it is possible to identify this state as P^+H^- .
- The long-lasting state I4 shows a bleaching of the Q_x and Q_y -Bands of P at 600 nm and 865 nm. The B-Band at 810 nm is blue shifted towards 785 nm. The Q_x -Band of H at 544 nm is recovered and there is an overall induced absorption at the spectrum edges (e.g. 500 to 600 and 920 to 1100) originated from P^+ . Therefore it is possible to identify this state as P^+Q^- .

In conclusion, these results support the validity of a sequential model with four intermediate states, as initially suggested by Holzapfel et al. [Hol89, Hol90]. The time constants obtained by this analysis are 1.2 ± 0.3 ps, 3.5 ± 0.2 ps, 220 ± 20 ps and a long-lasting component. The adapted scheme is then given by:



On the other hand it is also possible to fit the data using a similar model with the first two rates inverted. This has the same kinetic components and therefore presents no differences in the fit quality. However, the reconstructed SADS using an inverted model yields spectral characteristics which are not easy to interpret.

Finally we can compute the dichroic angles $\gamma(\lambda)$ between the absorbing dipole moments at the given wavelength and the ground state dipole moment of the special pair P (equation (2.39)). To do so it is important to identify the absorption cross-section of a single pigment and select absorption bands where the other pigments do not contribute. At this specific wavelength it is then possible to compute the dichroic angles of the corresponding transition (Q_x or Q_y). We will refer only to the Q_y transitions since they are the most relevant for the charge transfer process.

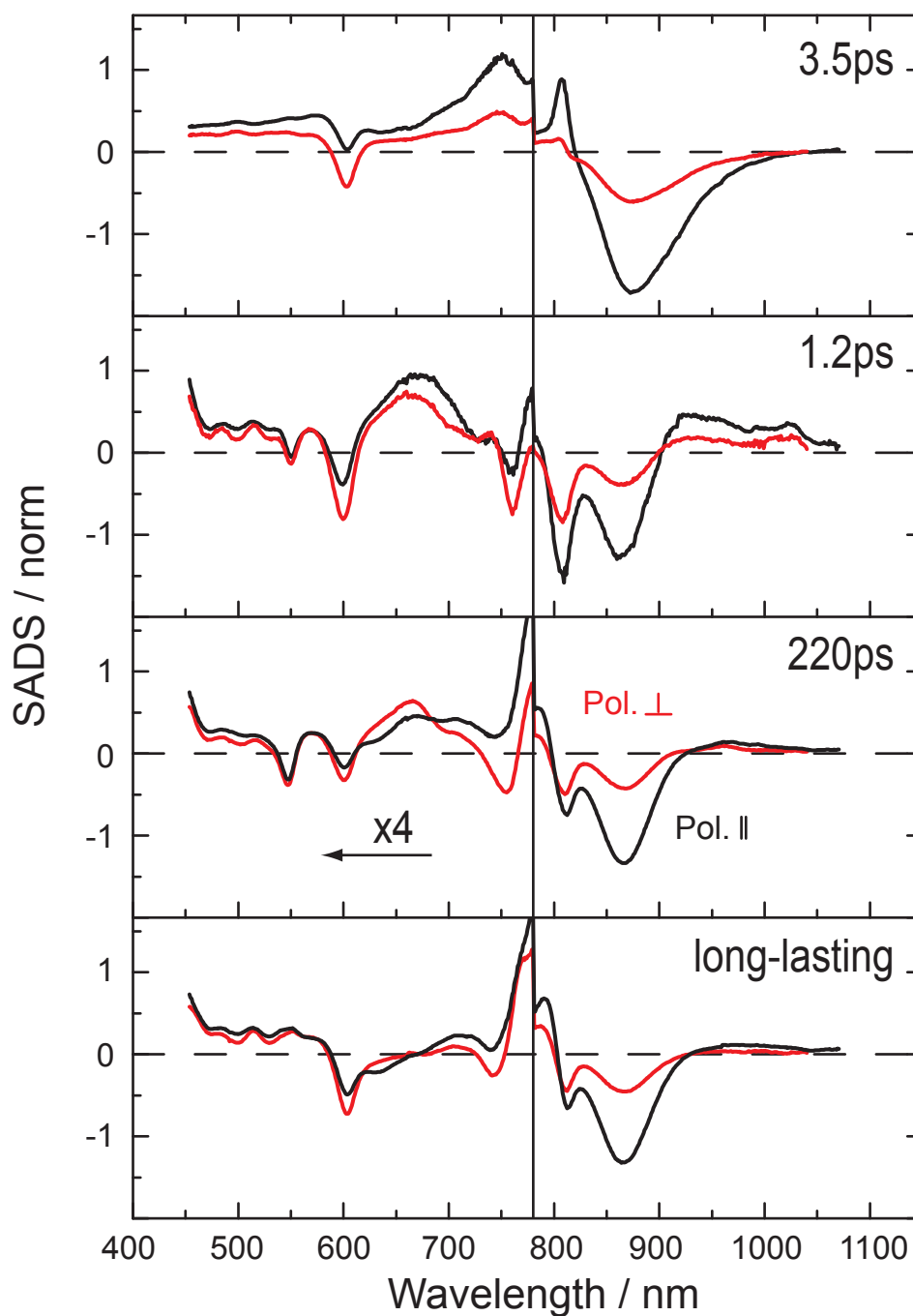


Figure 5.6: Reconstructed species associated difference spectra between 480-1060 nm. The black (red) curves correspond to parallel (perpendicular) measurements. The target model is sequential where the second intermediate state decays with the fastest time constant. Many characteristic of the state with lifetime 1.2 ps suggest a Bchl anion. The wavelengths below 780 nm were multiplied by x4.

The dichroic angles can be computed as follows:

- The absorption of the state P^* can be computed from $\Delta\sigma_1$, which corresponds to $I_1 = P^*$. At 998 nm it is possible to measure the ESA which contributes with a positive signal.
- The absorption of the state P^+ can be computed from $\Delta\sigma_4$, which corresponds to $I_4 = P^+Q_A^-$. Since the ubiquinone does not produce absorption changes in the near infrared region, the signal can be fully associated with the radical special pair. Here it is also possible to look at the induced absorption at 998 nm.
- The absorption of the state B^- can be computed as $\Delta\sigma_2 - \Delta\sigma_4$. At 1022 nm it is possible to measure the BChl-anion band.
- The absorption of the state H^- can be computed as $\Delta\sigma_3 - \Delta\sigma_4$. At 660 nm it is possible to measure the anion band of the reduced pheophytin.

$\gamma(P^*)$	$\gamma(P^+)$	$\gamma(B^-)$	$\gamma(H^-)$
9°	12°	31.4°	66.8°

Table 5.3: Dichroic angles corresponding to the \mathcal{Q}_y transition of the different charge transfer states, computed from dichroic measurements of reaction centers at 50 Hz.

The computed angles 31.4° and 66.8° (table 5.3) for the BChl and BPhe anions are in good agreement with the values reported by Holzapfel et al. (36° and 68°). Under the assumption that the transition dipole moment in the NIR region is the same for the neutral and the anion chlorophyll-like pigments, we can compare these values with the computed angles from structural data. This is motivated from quantum chemical computation of isolated radicals [Pet80, Pet81]. The Crystallographic data shows $\gamma_{struc}(B) = 29^\circ$ and $\gamma_{struc}(H) = 73^\circ$. Therefore both structural orientations and calculated dichroic properties of the BChl and BPhe anions coincide within the experimental precision.

5.2.2 Measurements at 500 Hz

In this section we will deal with the measurements of reaction centers using an excitation rate of 500 Hz. Because the RC were separated from the rest of the photosystem unit, it cannot relax to the ground state at ease. Therefore accumulation effects can occur and less absorption is observed.

As already discussed in section 4.4, these measurements were performed with poor stirring and without the fast flow exchange mechanism produced by the translational motion of the cuvette. Consequently the exhaustion of the sample was significantly increased. The reduced signal amplitude reflects that many RC in the excitation volume were not in the ground state.

For a better comparison, the data of both parallel and perpendicular measurements were scaled to have the same bleaching at the excitation wavelength $\lambda_{ex} = 865$ nm. However it is important to notice that, contrary to the 50 Hz measurements (fig. 5.3-a), the quotient between parallel and perpendicular bleaching signal of the special pair is not 3, which is expected from a single dipole transition. The unscaled data satisfies instead the following relation [Mic13, Leh14]:

$$\frac{\Delta A^{\parallel}(\lambda_{ex})}{\Delta A^{\perp}(\lambda_{ex})} = 2 \quad (5.6)$$

A lower value between parallel and perpendicular bleaching at the excitation band indicates a deviation from the single dipole moment absorption statistic. One possible cause of this effect is that the primary absorption is not originated by a single dipole. For example, if two slightly different samples contribute to the absorption signal, then the bleaching does not reflect the electronic transition of one oriented dipole moment, but a mixture of many. Another possibility could be the influence of saturation effects in the absorption signal of a single dipole moment. If the exposure levels are high, then the absorption of the molecules whose dipole is parallel oriented to the pump beam will reach the saturation before the molecules with perpendicular orientation [Jon96]. In this case the dichroic measurements will have a different relation.

The time dependence of the absorption change at some characteristic probing wavelengths is shown in figure 5.7. The data was scaled with a factor 6.5 for the parallel measurements (black) and 5.0 for the perpendicular measurements (red). Because of the lower signal, the data is not as smooth as the 50 Hz measurements (blue points). Another feature is the presence of strong coherent artifacts at time zero, whose contribution to the parallel measurements have twice the value of the signal at later times.

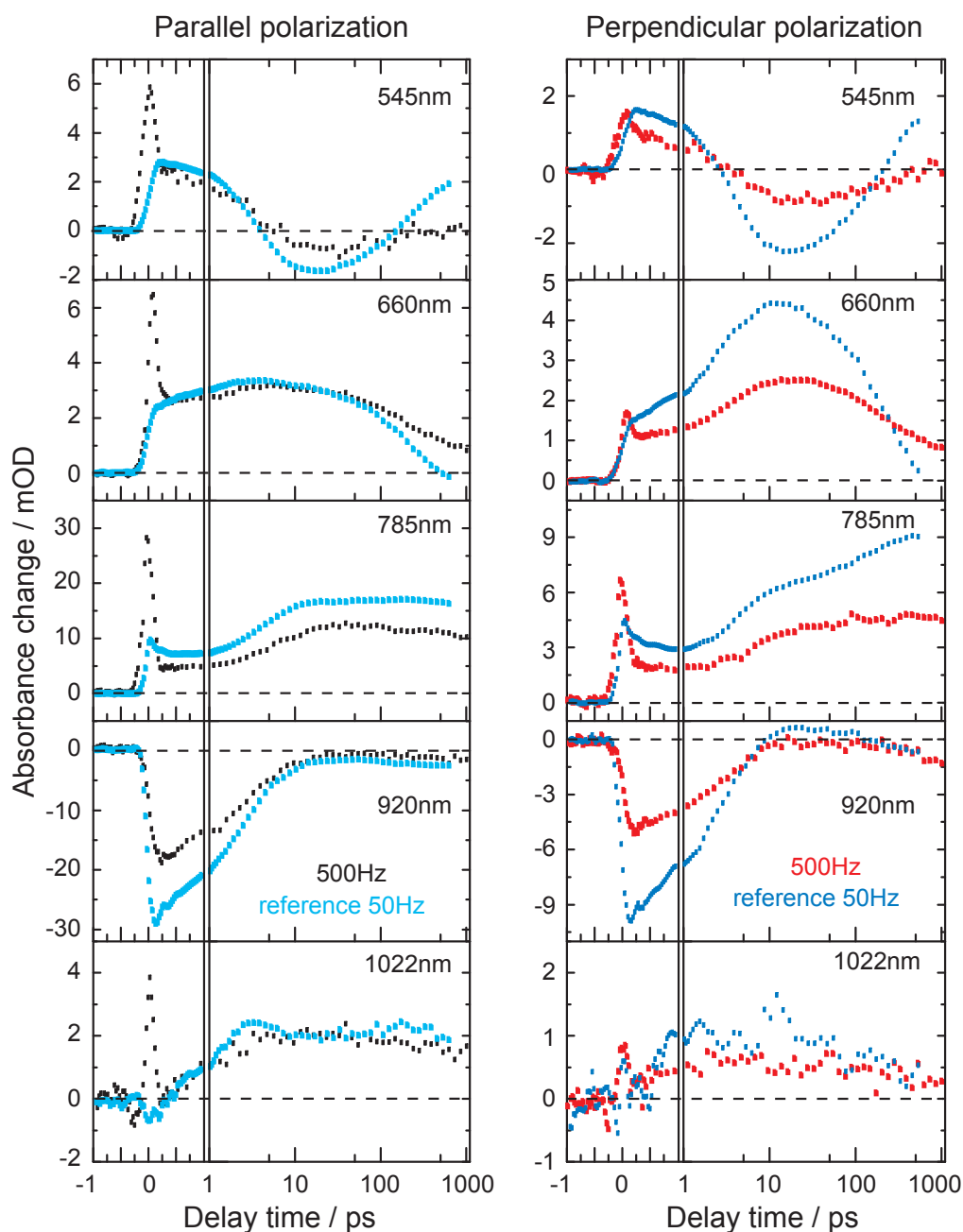


Figure 5.7: Time dependence of the absorption change at some characteristic probing wavelengths for the parallel (left) and perpendicular (right) polarization. The 500 Hz data (black/red) was scaled to reach the same bleaching of the 50 Hz measurements (blue) at the excitation wavelength. The presence of strong coherent artifacts at time zero makes the identification of the fastest time constant more difficult.

The time evolution of the measured signal is qualitatively similar to the 50 Hz measurements, however there are many discrepancies. First of all the difference in signal amplitude is not the same in all channels. The stimulated emission at 920 nm is 1.5 (1.7) times smaller for parallel (perpendicular) measurements. At 785 nm the signal is lower and the evolution after 300 fs is very flat, thus the 0.9 ps kinetic cannot be clearly identified. The B^- anion band at 1022 nm is, within the experimental precision, equal for both polarizations. Finally the mixed H^-/B^- anion band at 660 nm, as well as the H^- anion band at 545 nm, is 2 times smaller in the perpendicular polarization. Here the 200 ps kinetic is less remarkable and there is evidence of another time constant, namely 1 ns.

An attempt to fit the data in the [0, 3, 1000] ps time range produced unsatisfactory results. Due to the strong coherent artifacts it is not possible to identify the 0.9 ps uniquely, and indeed the outcome of the fit is strongly dependent on the starting values. In other words, the chisquare hypersurface is very flat, and the minimum is not well defined. Moreover modulations of the signal are still appreciable at early times.

A better analysis was made considering the whole time interval [-1, 1000] ps. In this case, the coherent artifacts were fitted independently as described in section 2.1.4. For this measurement, no particular kinetic model is available, therefore we perform target analysis with a diagonal rate matrix.

A preliminary examination was performed fitting the DADS from the raw data. Using four exponential decay functions is not sufficient for describing the time evolution of all channels. As already discussed before, a long time constant of 1 ns is needed. Furthermore a 10 ps kinetic is required, especially at the wavelength 795 nm (figure 5.8).

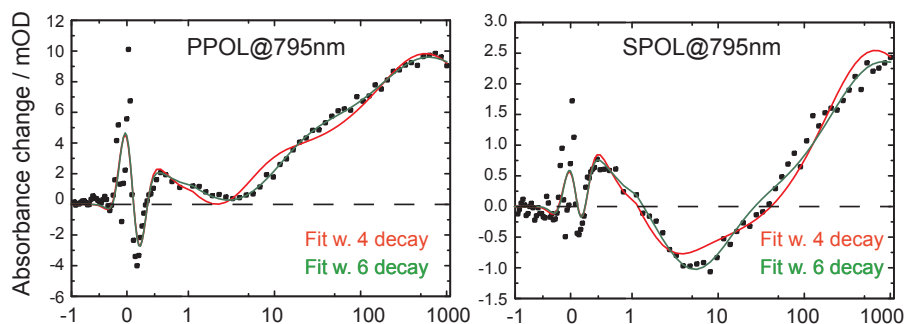


Figure 5.8: Time evolution of the reaction centers measured with 500 Hz repetition rate at 795 nm. The fit was performed with 4 exponential decays (1, 3.5, 200, 4000 ps) and 6 exponential decays (0.6, 2, 8, 250, 1000, ∞ ps). In this spectral region the need of a further time constant in the range of ca. 10 ps is evident.

The complete analysis was performed by fitting the time traces originated from the singular value decomposition in the corresponding time interval (figure 5.9). Estimating the number of significant SV using a MAD test resulted in 18 (13) SV for the parallel (perpendicular) measurement. The largest kinetic were fixed to $\tau_5 = 1000$ ps and $\tau_6 = \infty$. The remaining time constants were computed using a non-linear fit (table 5.4). Unfortunately the confidence intervals could not be computed due to the poor S/N ratio.

	parallel	perpendicular
τ_1	0.58	1.25
τ_2	2.05	3.56
τ_3	8.35	46
τ_4	250	135

Table 5.4: Computed time constants using 6 exponential decay functions. The largest kinetics $\tau_5 = 1000$ ps and $\tau_6 = \infty$ were kept constant.

The linear parameter of the fit form the C^{diag} -matrix, related to the target analysis with diagonal rate matrix. It is then possible to compute the DADS using the V-matrix:

$$\Delta a_i(\lambda_k) = \sum_{j=1}^m C_{ij}^{diag} V_{jk}^t \quad (5.7)$$

The fastest time constant $\tau_1 \sim 0.6$ ps is more predominant in the parallel measurement. The fit produced anomalies in the excitation band, displayed by the oscillating behavior of the amplitude around 880 nm. Both parallel and perpendicular measurements have a strong positive amplitude at 820 nm and a negative amplitude at 850 nm, which cannot be uniquely associated with a B^- anion kinetic. The parallel measurement has further a positive amplitude at 600 and 789 nm, as well as a considerable negative amplitude at 1022 nm. The perpendicular data shows a broad positive amplitude at 666 nm and a negative amplitude at 750 nm.

The short time constants $\tau_2 \sim 2$ ps and $\tau_3 \sim 10$ ps have very similar spectral shape, except in the 650 nm region and around 790 nm. They present a positive amplitude at 546, 597, 750 and 810 nm as well as a negative amplitude at 910 nm. A comparison with the 50 Hz data indicates that both kinetics are related with the special pair P.

The middle time constant $\tau_4 \sim 230$ ps has a broad positive amplitude at 660 nm and a negative amplitude at 549, 760 and 800 nm. This indicates the presence of a H^- anion. The amplitudes for the near-infrared region $\lambda > 850$ nm have strong oscillations and should not be considered.

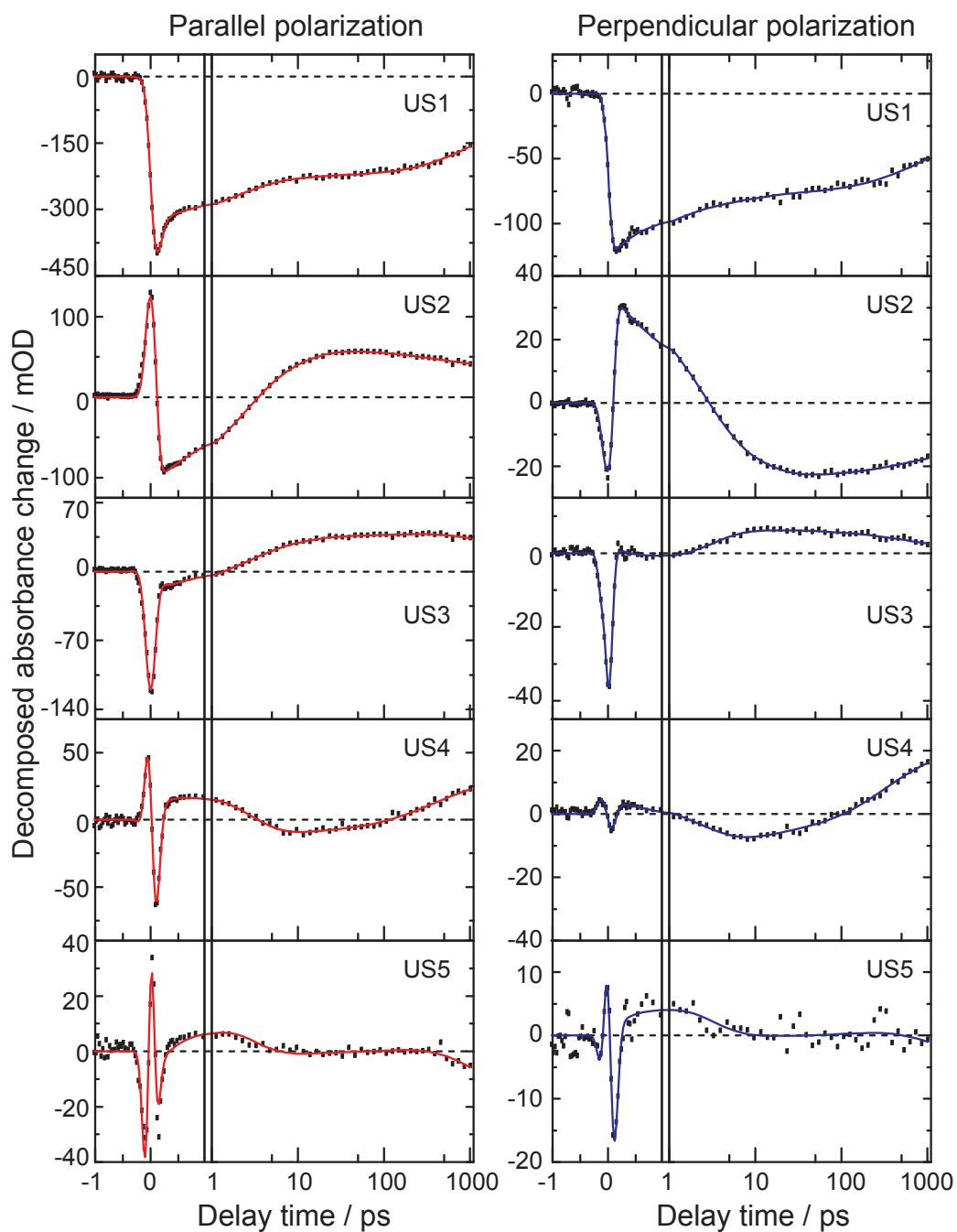


Figure 5.9: Decomposed time dependencies of the measurement at 500 Hz without reducing agents. Only the first five singular values are shown for the parallel (left) and perpendicular (right) measurements. The singular value decomposition was performed in the time interval $[-1, 1000]$ ps.

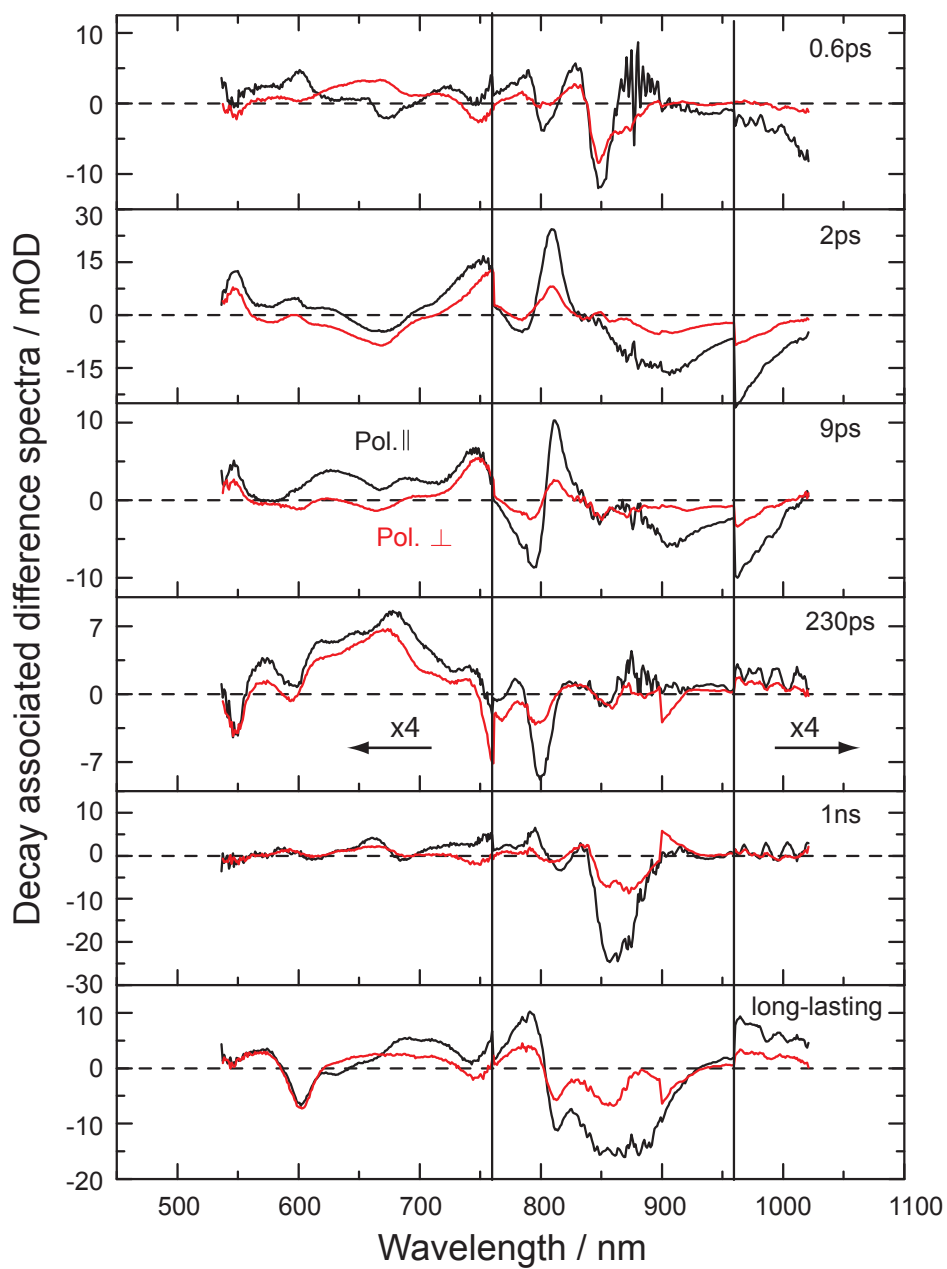


Figure 5.10: Reconstructed decay associated difference spectra (DADS) for the measurement with 500 Hz excitation rate without reducing agents. The amplitudes are shown for the parallel (black) and perpendicular (red) measurements. Data below 760 nm and above 960 nm was scaled by a factor 4.

The new time constant $\tau_5 \sim 1000$ ps is mostly present in the parallel measurements. It has a positive amplitude at 660, 750 and 800 nm and a high negative amplitude at 865 nm. It can be related to a recombination process of the H^- anion.

The last time constant $\tau_6 = \infty$ has a negative amplitude at 600, 800 and 865 nm and a positive amplitude at 785 nm. This can be related to the absorption of the P^+ .

In summary, the measurements of RC at high excitation rates reveals systematic alterations of the charge transfer process. An increased number of kinetics is appreciable, whose origin is still not clear. They may be related to modifications in the protein environment of the cofactors in the RC, as well as to recombination and trapping of the electron in radical states. Moreover the amplitude of the new 8 ps kinetic should be analyzed with caution. Since the 2 and 8 ps time constants are close to each other one is not able to identify uniquely each component with a multiexponential fit within the experimental precision. A further discussion will be presented below.

5.2.3 Measurements at 500 Hz with reducing agents

In this section we will deal with the measurements of reaction centers mixed with 10 mmol/L sodium ascorbate and 1 mmol/L ortho-phenanthroline using an excitation rate of 500 Hz. The interaction between sample and chemicals allows relaxation to be improved, where the special pair is in its ground state, and therefore the measured signal is ca. 14 times higher than the previous measurement at 500 Hz without reducing agents. The better signal to noise ratio allows to understand better the influence of a high repetition rate on the sample.

Like in section 5.2.2, the measurements were also scaled to show the same bleaching signal at 865 nm as the 50 Hz measurements. Moreover the quotient between parallel and perpendicular bleaching signal of the unscaled data satisfies the same relation as in (5.6):

$$\frac{\Delta A^{\parallel}(\lambda_{ex})}{\Delta A^{\perp}(\lambda_{ex})} = 2 \quad (5.8)$$

The time dependence of the absorption change at some characteristic probing wavelengths is shown in figure 5.11. The data was scaled by a factor 0.33 (parallel, black points) and 0.23 (perpendicular, red points). Coherent artifacts at time zero are less pronounced compared to the measurements at 500 Hz without reducing agents and do not produce significant modulation of the signal at early times. In this case the fastest subpicosecond kinetic could be clearly observed.

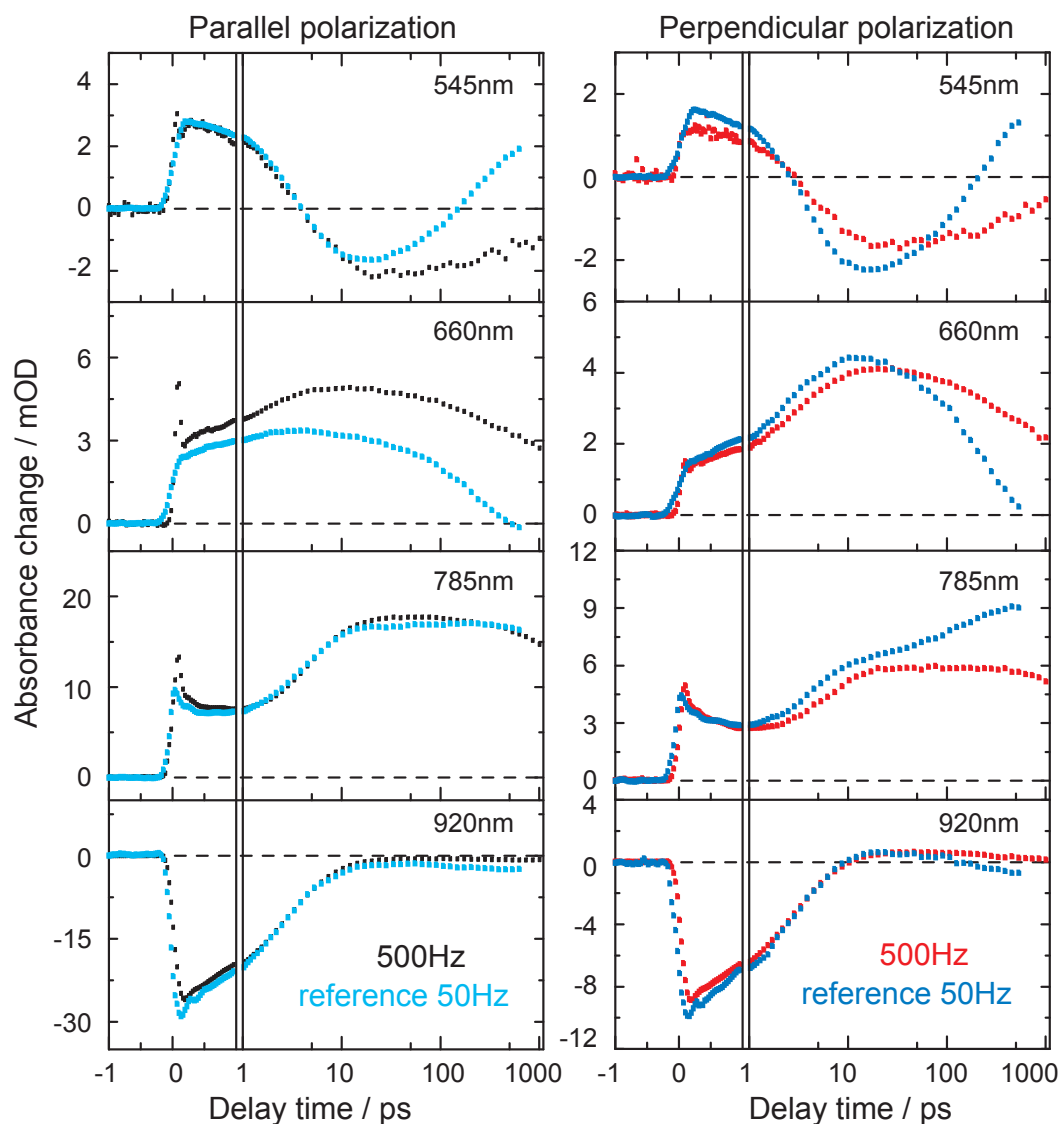


Figure 5.11: Time dependence of the absorption change at some characteristic probing wavelengths for the parallel (left) and perpendicular polarization (right). The 500 Hz data of RC with reducing agents (black/red) was scaled to have the same bleaching as the 50 Hz measurements (blue) at the excitation wavelength. Both measurements have similar kinetics in the first picoseconds whereas large deviations are present at later times.

For delay times $\Delta t \leq 1$ ps the time evolution of the measured signal is similar to the 50 Hz. The H^- anion band at 545 nm is 0.8 times smaller in the perpendicular polarization. The mixed H^-/B^- anion band at 660 nm is 1.2 times larger for the parallel measurements and 0.9 times smaller for the perpendicular measurements.

At 785 nm both measurements show the same kinetics. Finally the stimulated emission is 0.9 smaller at both polarizations.

In analogy to section 5.2.2, the time evolution at later times shows a 200 ps and a 1 ns kinetic. The 200 ps time constant has smaller amplitude than the 1 ns kinetic. Finally, the perpendicular measurements show a delayed signal rise at 660 nm and 785 nm, indicating a new time constant of about 6 ps.

The data was fitted in the time interval $[-1, 1000]$ ps and the coherent artifacts were analyzed as described previously. Modeling the data with six exponential decays resulted in a good fit quality of the corresponding decomposed time traces (fig. 5.12).

Parallel pol.				Perpendicular pol.			
\parallel	best	min	max	\perp	best	min	max
τ_1	0.52	0.20	0.79	τ_1	0.36	0.11	-
τ_2	2.04	1.23	2.67	τ_2	1.92	0.79	2.85
τ_3	5.63	3.50	8.08	τ_3	5.27	3.09	9.52
τ_4	181	-	-	τ_4	220	-	-

Table 5.5: Confidence interval for the time constant evaluated using an exhaustive search algorithm for the parallel (left) and perpendicular (right) dichroic measurements. All entries are in ps.

A MAD test estimated the number of significant singular values, which results in 18 SV for the parallel and 13 SV for the perpendicular polarization. These happen to be the same as in section 5.2.2. The computed time constants and corresponding confidence intervals are shown in table 5.5.

The decay associated difference spectra can be reconstructed using equation (5.7), leading to very smooth curves. They present similarities with the measurements at 500 Hz without reducing agents, only the signal to noise ratio was considerably improved.

The first time constant $\tau_1 \sim 0.6$ ps has a broad positive amplitude at 784 nm and its shape is different from the one found in section 5.2.2. Other positive bands are located at 660 nm for the perpendicular measurement, and at 910 nm for both polarizations. Negative amplitudes appear at 630 , 685 and 810 nm for the parallel measurement, as well as 745 nm for both polarizations.

The amplitude of the short time constants $\tau_2 = 2$ ps and $\tau_3 = 6$ ps are almost identical to those reported in section 5.2.2, and minor differences can be appreciated in the relative signal height.

The middle time constant $\tau_4 \sim 200$ ps has also similar shape as in section 5.2.2. However, its absolute value is about 2 times smaller. In this case the positive amplitude at 660 nm is larger for the perpendicular measurement, as expected from a pheophytin anion H^- .

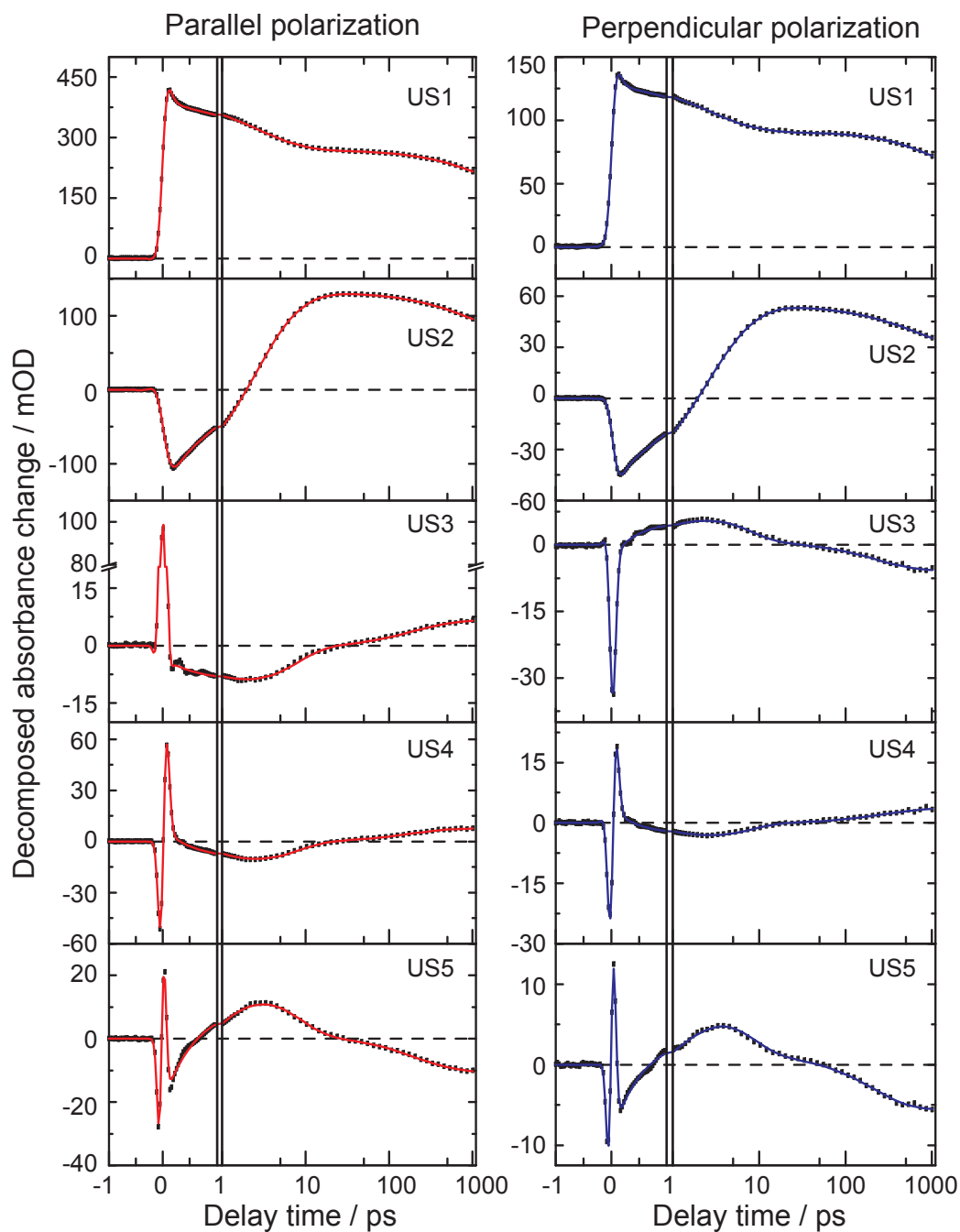


Figure 5.12: Decomposed time dependencies of the measurement at 500 Hz with ascorbate and ortho-phenanthroline. Only the first five singular values are shown for the parallel (left) and perpendicular (right) measurements. The singular value decomposition was performed in the time interval $[-1, 1000]$ ps.

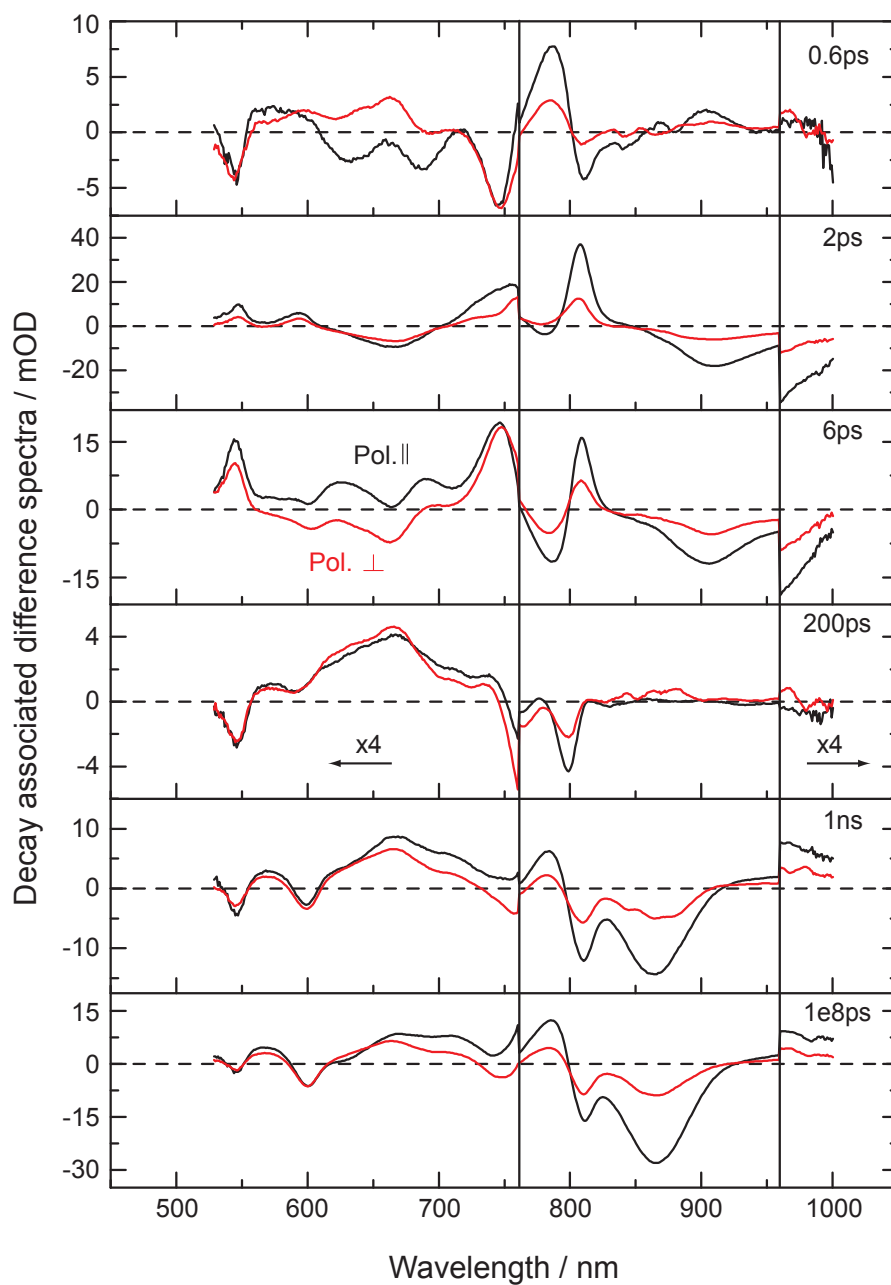


Figure 5.13: Reconstructed decay associated difference spectra (DADS) for the measurement with 500 Hz excitation rate with addition of ascorbate and ortho-phenanthroline. The amplitudes are shown for the parallel (black) and perpendicular (red) measurements. Data below 760 nm and above 960 nm was scaled by a factor 4.

The time constant $\tau_5 \sim 1000$ ps is more relevant than in section 5.2.2 and has a well defined structure. It has the same shape as $\tau_6 = 1 \cdot 10^8$ ps and similar signal height, which is consistent with a recombination kinetic of the H^- anion. There are positive absorption bands at 660 and 785 nm and a broad positive amplitude in the NIR-region. The negative bands are located at 545, 600, 810 and 865 nm.

Discussion and possible reaction model

In the following a possible interpretation of the obtained DADS (figure 5.13) will be discussed. The increased number of kinetics with sometimes similar decay times does not allow to find a simple reaction model. In this context we will use the simplest reaction scheme available which may describe the experimental observations.

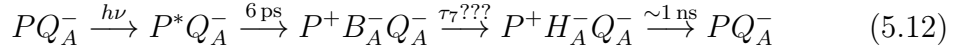
First of all one should notice that the presence of ascorbate in the sample can artificially reduce the special pair radical P^+ and brings the RC into an accumulated state, for example PQ_A^- where the special pair is in the electronic ground state and the ubiquinone is reduced. This can be deduced from the decreased amplitude of $\tau_4 \sim 200$ ps compared to the measurements at 50 Hz, since the transfer $P^+H_A^-Q_A^- \rightarrow P^+H_AQ_A^{2-}$ is unlikely. More probable is a recombination towards the oxidized special pair P^+ which may correspond to the nanosecond kinetic τ_5 . In fact the recombination from the radical BPhe occurs in native RC in ca. 10 ns when the ubiquinone Q_A is chemically extracted [Feh89]. It is therefore plausible that the presence of a radical Q_A^- could accelerate the recombination process:



The amplitude of the fastest time constant τ_1 has a strong contribution in the BChl band at 810 nm and displays similarities with the 1.2 ps kinetic found at 50 Hz. Differences may originate from the number of time constants used for the fitting procedure. Indeed, if the 50 Hz measurements are fitted with 5 exponential decays (0.9 ps, 2 ps, 5 ps, 220 ps and a long-lasting component), then the amplitudes of the fastest time constant become very similar (data not shown). Thus the kinetic τ_1 may still describe the electron transfer $B_A^-H_A \rightarrow B_AH_A^-$.

The time constants $\tau_2 = 2$ ps and $\tau_3 = 6$ ps have partially the same amplitudes as the 3.5 ps kinetic at 50 Hz. This can indicate a possible heterogeneity in the formation of the electronically excited special pair. Because τ_3 is two times slower than the expected decay of P^* , it is reasonable that the heterogeneity may be caused from the molecular environment. More precisely it may be due to an accumulated radical Q_A^- which slows down the electron transfer due to the Coulomb-repulsion between charges.

In summary a possible reaction scheme is given by the following equations:



In equation (5.12) the time constants τ_7 was postulated but could not be resolved in this experiment. The increased kinetic $\tau_3 \sim 6 \text{ ps}$ leads to a lower population of the state $P^+ B_A^- H Q_A^-$ and makes its detection more difficult.

5.3 Final remarks and conclusions

In this chapter the experimental data regarding reaction centers from *Rhodobacter sphaeroides* was presented and discussed for the different available excitation rates. Measurements using 50 Hz excitation rate were used to study the electron transfer kinetics under physiological conditions. The data could be simulated using a stepwise reaction model where the fastest time constant $\sim 1 \text{ ps}$ appears in the second reaction step.

Measurements using 500 Hz excitation rate were performed to test the exhaustion of the sample. It was possible to demonstrate that, due to the high excitation levels, new reactions occur whose role in the primary charge separation process in nature is negligible. The observed kinetics can be qualitatively explained by a heterogeneous model (see equations (5.10), (5.11), (5.12)), caused by the partial accumulation of $P Q_A^-$ radicals. All in all there are still two points of discussion:

First, the model does not explain the relation between parallel and perpendicular absorption signals at the excitation band (equation (5.6)). We found no evidence that the primary absorption is not uniquely originated by the Q_y transition of the special pair at 865 nm. Thus, the anomalous relation between parallel and perpendicular measurements could be originated by saturation effects.

Second, the obtained DADS of the $\sim 3 \text{ ps}$ and $\sim 6 \text{ ps}$ time constants in both measurements, with addition of ascorbate/ortho-phenanthroline and without reducing agents, are very similar. At this point we can conclude that, assuming the validity of the presented reaction model, there is also an accumulation of $P Q_A^-$, i.e. RC with neutral P and with reduced ubiquinone, in the measurement without reducing agents. However in the absence of ascorbate it is not clear how the oxidized special pair in $P^+ Q_A^-$ should obtain an electron from the environment. One possibility could be the reduction of the special pair by the negative radicals available in the buffer solution, which is less efficient than the reduction by ascorbate. In this context it should be noted that the formation of $P Q_A^-$ radicals is not as significant

as in the measurements at 500 Hz with reducing agents. As observed, the number of RC absorbing at 865 nm is reduced due to the high exhaustion of the sample. Thus it is imaginable that the signal produced by these two RC populations could have the same magnitude. Further experiments will clarify these remaining aspects.

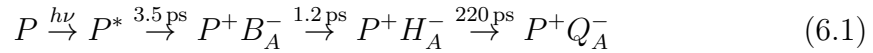
6 Summary

In this thesis the primary reactions in photosynthetic reaction centers from the purple bacteria *Rhodobacter sphaeroides* were studied at room temperature under different experimental conditions. This bacterium has one of the best studied photosystems, with well defined absorption bands of the pigments (cofactors) involved making it suitable for optical experiments. After photoexcitation at 865 nm an electron is transferred from the special pair (P) via the bacteriochlorophyll (B) and bacteriopheophytin (H) to the ubiquinone (Q). Many different reaction schemes were presented in the literature to explain the high quantum efficiency of the process and are still controversial. In particular there are three main conflicting points: (i) existence of a fast (~ 1 ps) kinetic involved in the electron transfer, (ii) the role of coherent effects in the charge transfer process and (iii) the possible adiabaticity of the process.

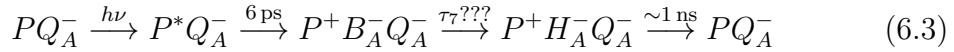
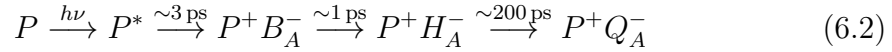
A pump-probe experiment was built to perform measurements in the spectral range 450-1060 nm with subpicosecond time resolution for delay times between $-1 \text{ ps} \leq \Delta t \leq 1 \text{ ns}$. Optimization of the non-linear processes involved in the generation of pump and probe beams led to high signal to noise ratio. Special attention was paid to the BChl band around 800 nm, where it was possible to detect weak transmission changes $\Delta T/T < 10^{-4}$.

Within a non-adiabatic electron transfer theory it is possible to model the reaction by rate equations whose kinetics are given by exponential decays. In this context we showed that a simple stepwise model with an involved 1 ps time constant, as originally proposed by Holzapfel et al. [Hol89], does explain the observed kinetics for delay times > 0.3 ps when using low exposure levels, namely low excitation energy and low excitation rate. Furthermore, the coherent oscillations observed at early times have a small amplitude compared to those of the electron transfer reaction and vanish after a few 100 fs. Therefore they do not influence the charge transfer dynamics at later times. Deviations from the simple stepwise model become visible when using higher exposure levels.

Measurements performed under physiological conditions using an excitation rate of 50 Hz displayed the time constants 1.2 ± 0.3 ps, 3.5 ± 0.2 ps, 220 ± 20 ps and a long-lasting component. These results are in good agreement with previous publications. The data was fitted using singular value decomposition and target analysis. Furthermore, a new consistency analysis was developed to test the compatibility of the target model with the experimental data. The following reaction scheme reproduced the expected absorption spectra of the intermediate radical states very well:



Measurements with an excitation rate of 500 Hz showed significant deviations from the simple stepwise model. The measured time constants were 0.6 ps, 2 ps, 6-9 ps, 200 ps, 1 ns and a long-lasting component. In this case the experimental data could be explained by the following heterogeneous model:



where the time constant τ_7 could not be detected.

In sum, this thesis provide very accurate experimental information about the primary reaction step in photosynthetic reaction centers from purple bacteria *Rhodobacter sphaeroides*. The measurements under physiological conditions reaffirmed the simple stepwise model for the electron transfer dynamics relevant in natural photosynthesis, in contradiction with several recent publications. The origin of these discrepancies was identified as a chemical modification of the reaction centers due to high exposure levels, where the accumulation of reaction centers in the state PQ_A^- is present.

Further experiments will make use of the acquired know-how in sample exposure of reaction centers. In particular, measurements with shorter excitation pulses (~ 50 fs) are suitable for studying the fast coherent oscillations under low excitation levels. In this approach it will be possible to study the kinetics taking place before the electron transfer and to extend the reaction model towards early times.

7 Zusammenfassung

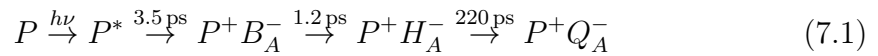
In der vorliegenden Arbeit wurden Energietransferschritte in den Reaktionszentren vom Purpurbakterium *Rhodobacter sphaeroides* bei Raumtemperatur, sowie deren Veränderung bei verschiedenen experimentellen Bedingungen untersucht. Dieses Photosystem besitzt Pigmente (Kofaktoren) deren Absorptionsbanden sich im sichtbaren und nahinfraroten Spektrum häufig nicht wesentlich überschneiden. Eine Analyse der chemischen Veränderungen ist dann mit optischen Experimenten möglich. Ein Elektron wird, nach Anregung mit Licht der Wellenlänge 865 nm, vom ursprünglich angeregten special pair (P) über ein Bakteriochlorophyll (B) und ein Bakteriophäophytin (H) zum Ubichinon (Q) übertragen. Eine große Zahl von Reaktionsschemen welche die hohe Quanteneffizienz des Prozesses erklären wurde in der Literatur vorgeschlagen. Dabei sind die primären Reaktionsschritte der Photosynthese noch umstritten. Insbesondere gibt es drei Hauptkonfliktpunkte: (i) die Existenz einer schnelleren (~ 1 ps) Kinetik, (ii) die Auswirkung von kohärenten Effekten auf den Prozess des Ladungstransfers und (iii) eine mögliche Adiabaticität der Reaktion.

In dieser Arbeit wurde zuerst ein Anrege/Abtastexperiment für den Spektralbereich zwischen 450 und 1060 nm entwickelt. Die Messungen wurden an verschiedenen Zeitschritten $-1 \text{ ps} \leq \Delta t \leq 1 \text{ ns}$ aufgenommen und die Zeitauflösung lag im Sub-pikosekundenbereich. Die Anrege- und Abtastpulsen wurden zusätzlich durch nichtlineare Effekte generiert deren Optimierung zu einem hohen Signal-Rausch Verhältnis führt. In diesem Zusammenhang hatte die BChl-Bande bei 800 nm eine Sonderstellung, da hier die Detektion von Transmissionsänderungen $\Delta T/T < 10^{-4}$ möglich war.

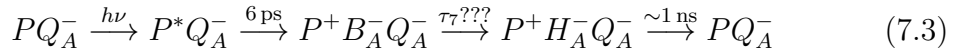
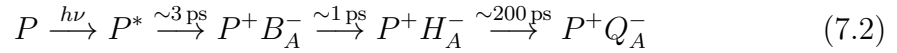
Im Rahmen einer nicht-adiabatischen Elektrontransfertheorie ist es möglich die Reaktionen mit einer Rategleichung zu beschreiben. Die resultierenden Kinetiken sind monoexponentielle Zerfälle. Bei der Betrachtung von Messungen bei niedrigen Anregungsenergien und Anregungsraten wurde gezeigt, dass ein einfaches Stufenmodell die Transienten ab 0.3 ps nach der Anregung beschreibt. Dieses Modell, bei dem eine Zeitkonstante von 1 ps vorkommt, wurde ursprünglich von Holzappel et al. [Hol89] vorgeschlagen. Außerdem wurden kohärente Oszillationen bei früheren Zeiten beobachtet, die nach einigen 100 fs verschwinden. Diese Oszillationen haben eine niedrigere Amplitude als die Kinetiken des Elektrontransfers und haben keine Auswirkung auf die Dynamik des Ladungstransfers zu späteren Zeiten. Messungen mit höherer Probenbelastung, die durch eine höhere Anregungsrate verursacht

wurden, zeigten deutliche Abweichungen und konnten nicht durch ein Stufenmodell angepasst werden.

Messungen bei physiologischen Bedingungen, deren Anregungsrate 50 Hz betrug, zeigten die Zeitkonstanten 1.2 ± 0.3 ps, 3.5 ± 0.2 ps, 220 ± 20 ps sowie eine langlebige Komponente. Diese stimmen mit vorherigen Publikationen überein. Die Daten wurden mit einem modernen Algorithmus ausgewertet, der sogenannten Singulärwertzerlegung mit Targetanalyse. Dabei wurde ein neuer Konsistenztest entwickelt, der die Kompatibilität des Modells mit den Daten quantifiziert. Das folgende Reaktionsschema konnte die erwarteten Absorptionsspektren der radikalen Zwischenzustände sehr gut nachbilden:



Messungen mit einer Anregungsrate von 500 Hz weichen vom Stufenmodell ab. Die gemessenen Zeitkonstanten waren 0.6 ps, 2 ps, 6-9 ps, 200 ps, 1 ns sowie eine langlebige Komponente. In diesem Fall wurde ein heterogenes Modell zur Erklärung der Daten aufgestellt:



wobei die Zeitkonstante τ_7 nicht detektiert werden konnte.

Ein besonderes Merkmal dieser Arbeit sind die äußerst präzisen experimentellen Informationen über die Primärreaktionen in photosynthetischen Reaktionszentren von *Rhodobacter sphaeroides*. Messungen bei physiologischen Belichtungsbedingungen bestätigten das einfache Stufenmodell. Diese Elektronentransferdynamiken sind die einzigen, die eine Rolle bei der natürlichen Photosynthese spielen, was im Widerspruch zu einer Reihe von kürzlich veröffentlichten Daten steht. Der Grund für solche Abweichungen konnte durch chemische Veränderungen der Reaktionszentren bei hohe Anregungsraten erklärt werden, die eine Akkumulation von Molekülen im PQ_A^- Zustand verursacht. Dieser Effekt beeinflusst die Kinetiken der Reaktion.

Weitere Experimente werden die hier gesammelten Erkenntnisse über die Belastung von Reaktionszentren nutzen können. Insbesondere können Messungen mit kürzeren Anregungspulsen (~ 50 fs) die schnellen kohärenten Oszillationen bei niedriger Belastung aufklären. Dadurch wird es möglich sein die Kinetiken vor dem Elektronentransfer zu untersuchen und das Reaktionsmodell zu früheren Zeiten zu erweitern.

Nomenclature

μs :	microsecond = $1 \cdot 10^{-6} \text{ s}$
B :	accessory bacteriochlorophyll cofactor
$BChl$:	bacteriochlorophyll
$BPhe$:	bacteriopheophytin
BBO :	beta barium borate
$DADS$:	decay associated difference spectra
$DMSO$:	di-methyl sulfoxide
ESA :	excited state absorption
ET :	electron transfer
fs :	femtosecond = $1 \cdot 10^{-15} \text{ s}$
GVM :	group velocity mismatch
GSE :	ground state bleaching
H :	bacteriopheophytin cofactor
kDa :	kilodalton = $1.66 \cdot 10^{-24} \text{ kg}$
LH :	light harvesting complex
MAD :	median absolute deviation
NIR :	near-infrared
$NOPA$:	non-collinear parametric amplifier
ns :	nanosecond = $1 \cdot 10^{-9} \text{ s}$
OD :	optical density
OPA :	optical parametric amplifier
P :	special pair cofactor
ps :	picosecond = $1 \cdot 10^{-12} \text{ s}$
Q :	ubiquinone cofactor
RC :	reaction center
RSD :	residual standard deviation

Sa: sapphire crystal
SADS: species associated difference spectra
SE: stimulated emission
SF: fused silica
SV: singular value
SVD: singular value decomposition
Ti : Sa: titan sapphire crystal
TRIS: 2-Amino-2-hydroxymethyl-propane-1,3-diol
VIS: visible
WT: wild type
YAG: yttrium-aluminium-granat

List of Figures

1.1	Sequential reaction scheme with four charge transfer states. The short lifetime of the accessory bacteriochlorophyll B_A avoids recombination losses.	2
2.1	Schematic representation of a pump-probe experiment.	7
2.2	Generated signal field after a pump probe experiment. Only the component propagating in the \mathbf{k}_t direction is detected.	9
2.3	Calculated contribution from coherent artifacts in pump-probe signal for $\tau = \infty$ (a) and $\tau = 0.9$ ps (b) within a time resolution $t_{corr} = 100$ fs. The strong deformation of the total signal makes the detection of fast kinetics more difficult.	11
2.4	Schematic representation of the parametric amplification process (a) and the non-collinear angle Ω necessary to reduce the negative effects of the GVM (b). During the parametric process the pump photons are absorbed and the number of seed photons is increased. In same amount the idler photons are generated. The non-linear crystal BBO has an inclined optical axis (o.a.) to ensure the phase matching condition.	15
2.5	Evolution of the charge transfer states for a sequential model. The time scale is linear in the range $[0,1]$ ps and logarithmic afterward. The population of the first intermediate $P^+B_A^-$ is very small, thus very difficult to detect.	19
2.6	Schematic representation of the singular value decomposition (SVD). The data matrix may be decomposed as a linear combination of columns from U and rows from transposed V. The gray regions correspond to elements which have no relevant information and thus may be considered as noise.	22
2.7	Schematic representation of the MAD-test. The histogram of computed $\sigma_{rsd}(i)$ is shown for the case $k \geq p$ (left) and $k = p - 1$ (right). First 20 singular values are plotted as inset. This analysis is well suited to identify outliers in the distribution.	24
2.8	Non-adiabatic transfer between two potential energy surfaces after photoexcitation.	25

2.9	Application of Marcus theory. The free polarization energy surfaces are assumed to be parabolas for both initial and final diabatic charge transfer states.	26
2.10	Set of functions used to fit the transient data using pure exponential decay (a) and a linear combination given by the kinetic model (b). The time constants are arranged in the order 3.5, 0.9, 200 and $1 \cdot 10^8$ ps. 30	
3.1	Electron micrograph of purple bacteria <i>Rb. sphaeroides</i> . The arrows indicate the position of the photosystem units where the reaction centers are located [Cla78].	35
3.2	Solar irradiance spectra [Ame] and absorption spectrum of purple bacteria <i>Rb. sphaeroides</i> [BP07] . These photosynthetic organisms developed protein systems which can absorb the sunlight present at the earth surface.	36
3.3	Distribution of protein complexes present in the photosynthetic unit at the intracytoplasmic membrane (a) and ribbon representation of the RC with the full protein backbone (b). The arrows show the synthesis of ATP after the absorption of two photons.	37
3.4	Molecular structure of Reaction Centers from <i>Rb. sphaeroides</i> . The cofactors involved in the charge transfer process are symmetrically distributed into two branches (A and B). In particular there are one bacteriochlorophyll dimer (P), two accessory bacteriochlorophylls (B), two bacteriopheophytins (H) and two ubiquinones (Q).	38
3.5	Absorption spectrum of reaction centers from <i>Rb. sphaeroides</i> . The contribution from different pigments can be determined.	40
3.6	Recombination rates of charge transfer states in reaction centers for the wild type strain (a) and chemical treated with ascorbate and ortho-phenanthroline (b).	50
3.7	Chemical structure of sodium-ascorbate (a) and ortho-phenanthroline (b).	51
4.1	Absorption spectrum of the calibration laser dye IR132 in DMSO. .	54
4.2	Schematic representation of the pump-probe setup. The experiment is divided into a pump branch and a probe branch.	56
4.3	Schematic representation of the NOPA setup.	57
4.4	Schematic representation of the prism compressor setup.	58
4.5	Spectrum of the excitation pulse centered at 865 nm (a) and auto-correlation after the prism compressor (b).	59
4.6	Different types of continuum generation.	61
4.7	Spectrum of different types of white light continuum (a). Measured pump-probe signal without sample, averaged over 2000 pulses (b). .	62
4.8	Focusing optic. All mirrors had silver coating.	63

4.9	Exchange mechanisms. For description see text.	64
4.10	Disposition of chopper and mechanical shutter in the pump-probe experiment.	66
4.11	Approximated efficiency curves from grating (a) and photodiode array (b).	67
4.12	Slow energy drift of the probe continuum. In a pump-probe experiment the absorption of the sample is referenced after each excitation. In this example the mean energy drift over the excitation pulses is lower than the mean energy drift over the reference pulses.	69
5.1	Dynamics of the laser dye IR132 in DMSO in a 3D-plot. The data is displayed at magic angle, computed using parallel and perpendicular dichroic measurements.	71
5.2	Time resolved data at characteristic wavelengths (a) and fit amplitudes for a three multiexponential fit (b), multiplied by 2 for wavelength below 700 nm . The data is displayed at magic angle, computed using parallel and perpendicular dichroic measurements.	72
5.3	Transient and stationary spectra (a) and time evolution at the given characteristic wavelengths (b). Black data has parallel polarization and red data perpendicular. For the absorbance changes in figure (a) the wavelengths below 760 nm and above 960 nm have been multiplied by x4.	74
5.4	Decay associated difference spectra between 480-1060 nm. The wavelengths below 760 nm and above 960 nm were multiplied by x4. If the stimulated emission with time constant 3.5 ps is modelled by a bi-exponential decay (2 ps [85%] and 7 ps [15%]), the amplitude of the 0.9 ps kinetic is slightly changed. This however has little influence in the computation of the SADS.	76
5.5	Decomposed absorbance for the first five $U \cdot S$ traces fitted with target analysis (a) and reconstructed populations vectors (b). Black points have parallel dichroism, red points perpendicular.	78
5.6	Reconstructed species associated difference spectra between 480-1060 nm. The black (red) curves correspond to parallel (perpendicular) measurements. The target model is sequential where the second intermediate state decays with the fastest time constant. Many characteristic of the state with lifetime 1.2 ps suggest a Bchl anion. The wavelengths below 780 nm were multiplied by x4.	80

5.7	Time dependence of the absorption change at some characteristic probing wavelengths for the parallel (left) and perpendicular (right) polarization. The 500 Hz data (black/red) was scaled to reach the same bleaching of the 50 Hz measurements (blue) at the excitation wavelength. The presence of strong coherent artifacts at time zero makes the identification of the fastest time constant more difficult.	83
5.8	Time evolution of the reaction centers measured with 500 Hz repetition rate at 795 nm. The fit was performed with 4 exponential decays (1, 3.5, 200, 4000 ps) and 6 exponential decays (0.6, 2, 8, 250, 1000, ∞ ps). In this spectral region the need of a further time constant in the range of ca. 10 ps is evident.	84
5.9	Decomposed time dependencies of the measurement at 500 Hz without reducing agents. Only the first five singular values are shown for the parallel (left) and perpendicular (right) measurements. The singular value decomposition was performed in the time interval [-1,1000] ps.	86
5.10	Reconstructed decay associated difference spectra (DADS) for the measurement with 500 Hz excitation rate without reducing agents. The amplitudes are shown for the parallel (black) and perpendicular (red) measurements. Data below 760 nm and above 960 nm was scaled by a factor 4.	87
5.11	Time dependence of the absorption change at some characteristic probing wavelengths for the parallel (left) and perpendicular polarization (right). The 500 Hz data of RC with reducing agents (black/red) was scaled to have the same bleaching as the 50 Hz measurements (blue) at the excitation wavelength. Both measurements have similar kinetics in the first picoseconds whereas large deviations are present at later times.	89
5.12	Decomposed time dependencies of the measurement at 500 Hz with ascorbate and ortho-phenanthroline. Only the first five singular values are shown for the parallel (left) and perpendicular (right) measurements. The singular value decomposition was performed in the time interval [-1,1000] ps.	91
5.13	Reconstructed decay associated difference spectra (DADS) for the measurement with 500 Hz excitation rate with addition of ascorbate and ortho-phenanthroline. The amplitudes are shown for the parallel (black) and perpendicular (red) measurements. Data below 760 nm and above 960 nm was scaled by a factor 4.	92

List of Tables

4.1	Absorption parameters for RC from <i>Rb. sphaeroides</i> . The photon density was set to $3.7 \cdot 10^{14} \text{ cm}^{-2}$	55
5.1	Confidence interval for each time constant evaluated using an exhaustive search algorithm for the parallel (left) and perpendicular (right) dichroic measurements. All entries are in ps.	75
5.2	Autocorrelation coefficient for the reconstructed population vector. The last component \mathcal{A}_5 corresponds to the remaining information which is not described by the targeted model.	77
5.3	Dichroic angles corresponding to the Q_y transition of the different charge transfer states, computed from dichroic measurements of reaction centers at 50 Hz.	81
5.4	Computed time constants using 6 exponential decay functions. The largest kinetics $\tau_5 = 1000 \text{ ps}$ and $\tau_6 = \infty$ were kept constant.	85
5.5	Confidence interval for the time constant evaluated using an exhaustive search algorithm for the parallel (left) and perpendicular (right) dichroic measurements. All entries are in ps.	90

Bibliography

- [All87] J. P. ALLEN, G. FEHER, T. O. YEATES, H. KOMIYA and D. C. REES. *Structure of the reaction center from Rhodobacter sphaeroides R-26: the protein subunits*. Proceedings of the National Academy of Sciences 84.17 (1987), pp. 6162–6166.
- [Ame] AMERICAN SOCIETY FOR TESTING AND MATERIALS. *Reference Solar Spectral Irradiance: Air mass 1.5*. URL: <http://rredc.nrel.gov/solar/spectra/am1.5/> (visited on 06/02/2014).
- [Arl93] T. ARLT, S. SCHMIDT, W. KAISER, C. LAUTERWASSER, M. MEYER, H. SCHEER and W. ZINTH. *The accessory bacteriochlorophyll: a real electron carrier in primary photosynthesis*. Proceedings of the National Academy of Sciences 90.24 (1993), pp. 11757–11761.
- [Bar88] J. BARBER. *Electron-transfer theory in question*. Nature 333.6169 (1988), pp. 114–114.
- [BBR09] M. BRADLER, P. BAUM and E. RIEDLE. *Femtosecond continuum generation in bulk laser host materials with sub- μ J pump pulses*. Applied Physics B 97.3 (2009), pp. 561–574.
- [Bee95] L. M. P. BEEKMAN et al. *Time-resolved and steady-state spectroscopic analysis of membrane-bound reaction centers from Rhodobacter sphaeroides. Comparisons with detergent-solubilized complexes*. Biochemistry 34.45 (1995), pp. 14712–14721.
- [Bix87] M. BIXON, J. JORTNER, M. MICHEL-BEYERLE, A. OGRODNIK and W. LERSCH. *The role of the accessory bacteriochlorophyll in reaction centers of photosynthetic bacteria: intermediate acceptor in the primary electron transfer?* Chemical Physics Letters 140.6 (1987), pp. 626–630.
- [BJM91] M. BIXON, J. JORTNER and M. MICHEL-BEYERLE. *On the mechanism of the primary charge separation in bacterial photosynthesis*. Biochimica et Biophysica Acta (BBA) - Bioenergetics 1056.3 (1991), pp. 301–315.
- [Bla02] R. E. BLANKENSHIP. *Molecular mechanisms of photosynthesis*. Oxford; Malden, MA: Blackwell Science, 2002.
- [BMJ88] M. BIXON, M. MICHEL-BEYERLE and J. JORTNER. *Formation Dynamics, Decay Kinetics, and Singlet–Triplet Splitting of the (Bacteriochlorophyll Dimer)+ (Bacteriopheophytin)- Radical Pair in Bacterial Photosynthesis*. Israel Journal of Chemistry 28.2 (1988), pp. 155–168.

- [BP07] H. BERBEROGLU and L. PILON. *Experimental measurements of the radiation characteristics of Anabaena variabilis ATCC 29413-U and Rhodobacter sphaeroides ATCC 49419*. International Journal of Hydrogen Energy 32.18 (2007), pp. 4772–4785.
- [Bre88] J. BRETON, J. L. MARTIN, G. R. FLEMING and J. C. LAMBRY. *Low-temperature femtosecond spectroscopy of the initial step of electron transfer in reaction centers from photosynthetic purple bacteria*. Biochemistry 27.21 (1988), pp. 8276–8284.
- [Bre99] M. E. v. BREDERODE, F. v. MOURIK, I. H. M. v. STOKKUM, M. R. JONES and R. v. GRONDELLE. *Multiple pathways for ultrafast transduction of light energy in the photosynthetic reaction center of Rhodobacter sphaeroides*. Proceedings of the National Academy of Sciences 96.5 (1999), pp. 2054–2059.
- [CF87] R. J. COGDELL and H. A. FRANK. *How carotenoids function in photosynthetic bacteria*. Biochimica et Biophysica Acta (BBA) - Reviews on Bioenergetics 895.2 (1987), pp. 63–79.
- [Cla78] R. K. CLAYTON. *The photosynthetic bacteria*. Plenum Press, 1978.
- [Cla80] R. K. CLAYTON. *Photosynthesis: Physical Mechanisms and Chemical Patterns*. Cambridge University Press, 1980.
- [Cre88] S. CREIGHTON, J. K. HWANG, A. WARSHEL, W. W. PARSON and J. NORRIS. *Simulating the dynamics of the primary charge separation process in bacterial photosynthesis*. Biochemistry 27.2 (1988), pp. 774–781.
- [CS03] G. CERULLO and S. D. SILVESTRI. *Ultrafast optical parametric amplifiers*. Review of Scientific Instruments 74.1 (2003), pp. 1–18.
- [Dei84] J. DEISENHOFER, O. EPP, K. MIKI, R. HUBER and H. MICHEL. *X-ray structure analysis of a membrane protein complex: Electron density map at 3 Å resolution and a model of the chromophores of the photosynthetic reaction center from Rhodospseudomonas viridis*. Journal of Molecular Biology 180.2 (1984), pp. 385–398.
- [DeV84] D. DEVAULT. *Quantum-mechanical tunnelling in biological systems*. Cambridge University Press, 1984.
- [Dom14] P. N. DOMINGUEZ, M. HIMMELSTOSS, J. MICHELMANN, F. T. LEHNER, A. T. GARDINER, R. J. COGDELL and W. ZINTH. *Primary reactions in photosynthetic reaction centers of Rhodobacter sphaeroides – Time constants of the initial electron transfer*. Chemical Physics Letters 601 (2014), pp. 103–109.

- [DP82] F. DUARTE and J. PIPER. *Dispersion theory of multiple-prism beam expanders for pulsed dye lasers*. Optics Communications 43.5 (1982), pp. 303–307.
- [Faj75] J. FAJER, D. C. BRUNE, M. S. DAVIS, A. FORMAN and L. D. SPAULDING. *Primary charge separation in bacterial photosynthesis: oxidized chlorophylls and reduced pheophytin*. Proceedings of the National Academy of Sciences 72.12 (1975), pp. 4956–4960.
- [Feh89] G. FEHER, J. P. ALLEN, M. Y. OKAMURA and D. C. REES. *Structure and function of bacterial photosynthetic reaction centres*. Nature 339.6220 (1989), pp. 111–116.
- [FS87] S. F. FISCHER and P. SCHERER. *On the early charge separation and recombination processes in bacterial reaction centers*. Chemical Physics 115.2 (1987), pp. 151–158.
- [FZV08] B. P. FINGERHUT, W. ZINTH and R. de VIVIE-RIEDLE. *Design criteria for optimal photosynthetic energy conversion*. Chemical Physics Letters 466.4 (2008), pp. 209–213.
- [FZV09] B. P. FINGERHUT, W. ZINTH and R. d. VIVIE-RIEDLE. *The detailed balance limit of photochemical energy conversion*. Physical Chemistry Chemical Physics 12.2 (2009), pp. 422–432.
- [GD89] M. R. GUNNER and P. L. DUTTON. *Temperature and ΔG dependence of the electron transfer from BPh \cdot to QA in reaction center protein from Rhodobacter sphaeroides with different quinones as QA*. Journal of the American Chemical Society 111.9 (1989), pp. 3400–3412.
- [Gou61] M. GOUTERMAN. *Spectra of porphyrins*. Journal of Molecular Spectroscopy 6 (1961), pp. 138–163.
- [Hac95] F. HACHE, A. ZÉBOULON, G. GALLOT and G. M. GALE. *Cascaded second-order effects in the femtosecond regime in β -barium borate: self-compression in a visible femtosecond optical parametric oscillator*. Optics Letters 20.14 (1995), pp. 1556–1558.
- [Ham93] P. HAMM, K. GRAY, D. OESTERHELT, R. FEICK, H. SCHEER and W. ZINTH. *Subpicosecond emission studies of bacterial reaction centers*. Biochimica et Biophysica Acta (BBA) - Bioenergetics 1142.1–2 (1993), pp. 99–105.
- [Ham95] P. HAMM, M. ZUREK, W. MÄNTELE, M. MEYER, H. SCHEER and W. ZINTH. *Femtosecond infrared spectroscopy of reaction centers from Rhodobacter sphaeroides between 1000 and 1800 cm^{-1}* . Proceedings of the National Academy of Sciences 92.6 (1995), pp. 1826–1830.

- [HB74] E. S. HSI and J. R. BOLTON. *Flash photolysis-electron spin resonance study of the effect of o-phenanthroline and temperature on the decay time of the ESR signal B1 in reaction-center preparations and chromatophores of mutant and wild strains of Rhodopseudomonas spheroides and Rhodospirillum rubrum*. Biochimica et Biophysica Acta (BBA) - Bioenergetics 347.1 (1974), pp. 126–133.
- [Him12] M. HIMMELSTOSS. *Transiente Absorptionsspektroskopie im nah-infraroten Spektralbereich: Versuchsaufbau und Charakterisierung*. Master thesis. Ludwig-Maximilians-Universität, 2012.
- [HM89] Y. HU and S. MUKAMEL. *Superexchange and electron transfer in the photosynthetic reaction center*. Chemical Physics Letters 160.4 (1989), pp. 410–416.
- [HM96] A. R. HOLZWARTH and M. G. MÜLLER. *Energetics and Kinetics of Radical Pairs in Reaction Centers from Rhodobacter sphaeroides. A Femtosecond Transient Absorption Study*^{†,‡}. Biochemistry 35.36 (1996), pp. 11820–11831.
- [Hol] W. HOLZAPFEL. *Aufklärung des ersten Schritts im Elektronentransport bei der Photosynthese von Rhodobakter sphaeroides*. PhD thesis. Technische Universität München.
- [Hol78] D. HOLTEN, M. W. WINDSOR, W. W. PARSON and J. THORNER. *Primary photochemical processes in isolated reaction centers of Rhodopseudomonas viridis*. Biochimica et Biophysica Acta (BBA) - Bioenergetics 501.1 (1978), pp. 112–126.
- [Hol80] D. HOLTEN et al. *Subpicosecond and picosecond studies of electron transfer intermediates in Rhodopseudomonas sphaeroides reaction centers*. Biochimica et Biophysica Acta (BBA) - Bioenergetics 592.3 (1980), pp. 461–477.
- [Hol89] W. HOLZAPFEL, U. FINKELE, W. KAISER, D. OESTERHELT, H. SCHEER, H. STILZ and W. ZINTH. *Observation of a bacteriochlorophyll anion radical during the primary charge separation in a reaction center*. Chemical Physics Letters 160.1 (1989), pp. 1–7.
- [Hol90] W. HOLZAPFEL, U. FINKELE, W. KAISER, D. OESTERHELT, H. SCHEER, H. U. STILZ and W. ZINTH. *Initial electron-transfer in the reaction center from Rhodobacter sphaeroides*. Proceedings of the National Academy of Sciences 87.13 (1990), pp. 5168–5172.
- [Hol96] A. R. HOLZWARTH. *Data Analysis of Time-Resolved Measurements. Biophysical techniques in photosynthesis*. Ed. by J. AMESZ and A. J. HOFF. Kluwer Academic, 1996, pp. 75–92.

- [IHL89] E. P. IPPEN, H. A. HAUS and L. Y. LIU. *Additive pulse mode locking*. Journal of the Optical Society of America B 6.9 (1989), pp. 1736–1745.
- [Jon96] D. M. JONAS, M. J. LANG, Y. NAGASAWA, T. JOO and G. R. FLEMING. *Pump-Probe Polarization Anisotropy Study of Femtosecond Energy Transfer within the Photosynthetic Reaction Center of Rhodobacter sphaeroides R26*. The Journal of Physical Chemistry 100.30 (1996), pp. 12660–12673.
- [Kak10] Y. KAKITANI, A. HOU, Y. MIYASAKO, Y. KOYAMA and H. NAGAE. *Rates of the initial two steps of electron transfer in reaction centers from Rhodobacter sphaeroides as determined by singular-value decomposition followed by global fitting*. Chemical Physics Letters 492.1–3 (2010), pp. 142–149.
- [KH88] C. KIRMAIER and D. HOLTEN. *Subpicosecond Spectroscopy of Charge Separation in Rhodobacter-Capsulatus Reaction Centers*. Israel Journal of Chemistry 28.2-3 (1988), pp. 79–85.
- [KH91] C. KIRMAIER and D. HOLTEN. *An assessment of the mechanism of initial electron transfer in bacterial reaction centers*. Biochemistry 30.3 (1991), pp. 609–613.
- [KKN06] Y. KOYAMA, Y. KAKITANI and H. NAGAE. *Mechanisms of Cis-Trans Isomerization around the Carbon–Carbon Double Bonds via the Triplet State*. C. DUGAVE. *Cis-trans Isomerization in Biochemistry*. John Wiley & Sons, 2006, pp. 15–51.
- [Kna85] E. W. KNAPP, S. F. FISCHER, W. ZINTH, M. SANDER, W. KAISER, J. DEISENHOFER and H. MICHEL. *Analysis of optical spectra from single crystals of Rhodopseudomonas viridis reaction centers*. Proceedings of the National Academy of Sciences 82.24 (1985), pp. 8463–8467.
- [Koz04] I. Z. KOZMA, P. BAUM, U. SCHMIDHAMMER, S. LOCHBRUNNER and E. RIEDLE. *Compact autocorrelator for the online measurement of tunable 10 femtosecond pulses*. Review of Scientific Instruments 75.7 (2004), pp. 2323–2327.
- [Lan32] L. LANDAU. *Zur Theorie der Energieübertragung. II*. Physikalische Zeitschrift der Sowjetunion 2 (1932), pp. 46–51.
- [Leh14] F. T. LEHNER. *Transiente Absorptionsspektroskopie an unbelasteten sowie chemisch modifizierten Reaktionszentren von Rhodobacter sphaeroides*. Master thesis. Ludwig-Maximilians-Universität, 2014.
- [Lor02] M. LORENC, M. ZIOLEK, R. NASKRECKI, J. KAROLCZAK, J. KUBICKI and A. MACIEJEWSKI. *Artifacts in femtosecond transient absorption spectroscopy*. Applied Physics B 74.1 (2002), pp. 19–27.

- [LTW96] S. LIN, A. K. W. TAGUCHI and N. W. WOODBURY. *Excitation Wavelength Dependence of Energy Transfer and Charge Separation in Reaction Centers from Rhodobacter sphaeroides: Evidence for Adiabatic Electron Transfer*. The Journal of Physical Chemistry 100.42 (1996), pp. 17067–17078.
- [Mai94] S. MAITI, G. C. WALKER, B. R. COWEN, R. PIPPENGER, C. C. MOSER, P. L. DUTTON and R. M. HOCHSTRASSER. *Femtosecond coherent transient infrared spectroscopy of reaction centers from Rhodobacter sphaeroides*. Proceedings of the National Academy of Sciences 91.22 (1994), pp. 10360–10364.
- [Mal09] E. R. MALINOWSKI. *Determination of rank by median absolute deviation (DRMAD): a simple method for determining the number of principal factors responsible for a data matrix*. Journal of Chemometrics 23.1 (2009), pp. 1–6.
- [Mar63] R. A. MARCUS. *Free Energy of Nonequilibrium Polarization Systems. III. Statistical Mechanics of Homogeneous and Electrode Systems*. The Journal of Chemical Physics 39.7 (1963), pp. 1734–1740.
- [Mar86] J.-L. MARTIN, J. BRETON, A. J. HOFF, A. MIGUS and A. ANTONETTI. *Femtosecond spectroscopy of electron transfer in the reaction center of the photosynthetic bacterium Rhodospseudomonas sphaeroides R-26: Direct electron transfer from the dimeric bacteriochlorophyll primary donor to the bacteriopheophytin acceptor with a time constant of 2.8 ± 0.2 psec*. Proceedings of the National Academy of Sciences 83.4 (1986), pp. 957–961.
- [Mar87] R. MARCUS. *Superexchange versus an intermediate BChl⁻ mechanism in reaction centers of photosynthetic bacteria*. Chemical Physics Letters 133.6 (1987), pp. 471–477.
- [Mar93] M. MARCHI, J. N. GEHLEN, D. CHANDLER and M. NEWTON. *Adiabatic surfaces and the pathway for primary electron transfer in a photosynthetic reaction center*. Journal of the American Chemical Society 115.10 (1993), pp. 4178–4190.
- [McD95] G. MCDERMOTT, S. M. PRINCE, A. A. FREER, A. M. HAWTHORNTHWAITE-LAWLESS, M. Z. PAPIZ, R. J. COGDELL and N. W. ISAACS. *Crystal structure of an integral membrane light-harvesting complex from photosynthetic bacteria*. Nature 374.6522 (1995), pp. 517–521.
- [Mic13] J. MICHELMANN. *Broadband transient absorption spectroscopy in the near infrared spectral region: Application on reaction centers of Rhodobacter sphaeroides*. Master thesis. Ludwig-Maximilians-Universität, 2013.

- [Mic88] M. MICHEL-BEYERLE, M. PLATO, J. DEISENHOFER, H. MICHEL, M. BIXON and J. JORTNER. *Unidirectionality of charge separation in reaction centers of photosynthetic bacteria*. Biochimica et Biophysica Acta (BBA) - Bioenergetics 932 (1988), pp. 52–70.
- [MOF90] P. MCPHERSON, M. OKAMURA and G. FEHER. *Electron transfer from the reaction center of Rb. sphaeroides to the quinone pool: Doubly reduced QB leaves the reaction center*. Biochimica et Biophysica Acta (BBA) - Bioenergetics 1016.2 (1990), pp. 289–292.
- [Muk95] S. MUKAMEL. *Principles of nonlinear optical spectroscopy*. New York [u.a.]: Oxford Univ. Press, 1995.
- [Nor71] J. R. NORRIS, R. A. UPHAUS, H. L. CRESPI and J. J. KATZ. *Electron Spin Resonance of Chlorophyll and the Origin of Signal I in Photosynthesis*. Proceedings of the National Academy of Sciences 68.3 (1971), pp. 625–628.
- [OIF75] M. Y. OKAMURA, R. A. ISAACSON and G. FEHER. *Primary acceptor in bacterial photosynthesis: obligatory role of ubiquinone in photoactive reaction centers of Rhodopseudomonas spheroides*. Proceedings of the National Academy of Sciences of the United States of America 72.9 (1975), pp. 3491–3495.
- [Par82] W. W. PARSON. *Photosynthetic Bacterial Reaction Centers: Interactions Among the Bacteriochlorophylls and Bacteriopheophytins*. Annual Review of Biophysics and Bioengineering 11.1 (1982), pp. 57–80.
- [Paw08] N. P. PAWLOWICZ, R. van GRONDELLE, I. H. van STOKKUM, J. BRETON, M. R. JONES and M. L. GROOT. *Identification of the First Steps in Charge Separation in Bacterial Photosynthetic Reaction Centers of Rhodobacter sphaeroides by Ultrafast Mid-Infrared Spectroscopy: Electron Transfer and Protein Dynamics*. Biophysical Journal 95.3 (2008), pp. 1268–1284.
- [Pet80] J. D. PETKE, G. M. MAGGIORA, L. L. SHIPMAN and R. E. CHRISTOFFERSEN. *Stereoelectronic properties of photosynthetic and related systems-VIII. Ab initio quantum mechanical characterization of the electronic structure and spectrum of the bacteriopheophorbide anion radical*. Photochemistry and Photobiology 32.5 (1980), pp. 661–667.
- [Pet81] J. D. PETKE, G. M. MAGGIORA, L. L. SIPMAN and R. E. CHRISTOFFERSEN. *Stereoelectronic properties of photosynthetic and related systems-IX. Ab initio quantum mechanical characterization of the electronic structure and spectrum of the bacteriochlorophyllide anion radical*. Photochemistry and Photobiology 33.5 (1981), pp. 663–671.

- [Rie00] E. RIEDLE, M. BEUTTER, S. LOCHBRUNNER, J. PIEL, S. SCHENKL, S. SPÖRLEIN and W. ZINTH. *Generation of 10 to 50 fs pulses tunable through all of the visible and the NIR*. Applied Physics B 71 (2000), pp. 457–465.
- [Sat04] H. SATZGER. *Untersuchung initialer Schritte der Peptidfaltung mit Ultrakurzzeitspektroskopie*. PhD thesis. Ludwig-Maximilians-Universität, 2004.
- [Sch94] S. SCHMIDT et al. *Energetics of the primary electron transfer reaction revealed by ultrafast spectroscopy on modified bacterial reaction centers*. Chemical Physics Letters 223.1–2 (1994), pp. 116–120.
- [Sch95] S. SCHMIDT et al. *Primary electron-transfer dynamics in modified bacterial reaction centers containing pheophytin-a instead of bacteriopheophytin-a*. Spectrochimica Acta Part A: Molecular and Biomolecular Spectroscopy 51.9 (1995), pp. 1565–1578.
- [SF86] P. SCHERER and S. F. FISCHER. *On the stark effect for bacterial photosynthetic reaction centers*. Chemical Physics Letters 131.1–2 (1986), pp. 153–159.
- [SH82] R. I. SHRAGER and R. W. HENDLER. *Titration of individual components in a mixture with resolution of difference spectra, pKs, and redox transitions*. Analytical Chemistry 54.7 (1982), pp. 1147–1152.
- [Shu78] V. SHUVALOV, A. KLEVANIK, A. SHARKOV, J. MATVEETZ and P. KRUKOV. *Picosecond detection of BChl-800 as an intermediate electron carrier between selectively-excited P870 and bacteriopheophytin in Rhodospirillum rubrum reaction centers*. FEBS Letters 91.1 (1978), pp. 135–139.
- [SLG04] I. H. van STOKKUM, D. S. LARSEN and R. van GRONDELLE. *Global and target analysis of time-resolved spectra*. Biochimica et Biophysica Acta (BBA) - Bioenergetics 1657.2–3 (2004), pp. 82–104.
- [SM85] D. STRICKLAND and G. MOUROU. *Compression of amplified chirped optical pulses*. Optics Communications 55.6 (1985), pp. 447–449.
- [Spö00] S. SPÖRLEIN, W. ZINTH, M. MEYER, H. SCHEER and J. WACHTVEITL. *Primary electron transfer in modified bacterial reaction centers: optimization of the first events in photosynthesis*. Chemical Physics Letters 322 (2000), pp. 454–464.
- [Sto97] I. H. M. van STOKKUM, L. M. P. BEEKMAN, M. R. JONES, M. E. van BREDERODE and R. van GRONDELLE. *Primary Electron Transfer Kinetics in Membrane-Bound Rhodobacter sphaeroides Reaction Centers: A Global and Target Analysis†*. Biochemistry 36.38 (1997), pp. 11360–11368.

- [Str13] J. STRÖBEL. *Degradation of Infrared Laser Dyes*. Bachelor thesis. Ludwig-Maximilians-Universität, 2013.
- [Str97] A. M. STRELTSOV, T. J. AARTSMA, A. J. HOFF and V. A. SHUVALOV. *Oscillations within the BL absorption band of Rhodobacter sphaeroides reaction centers upon 30 femtosecond excitation at 865 nm*. Chemical Physics Letters 266.3 (1997), pp. 347–352.
- [SZ03] H. SATZGER and W. ZINTH. *Visualization of transient absorption dynamics – towards a qualitative view of complex reaction kinetics*. Chemical Physics 295.3 (2003), pp. 287–295.
- [SZW98] S. SPÖRLEIN, W. ZINTH and J. WACHTVEITL. *Vibrational Coherence in Photosynthetic Reaction Centers Observed in the Bacteriochlorophyll Anion Band*. The Journal of Physical Chemistry B 102.38 (1998), pp. 7492–7496.
- [Tót09] S. Z. TÓTH, J. T. PUTHUR, V. NAGY and G. GARAB. *Experimental Evidence for Ascorbate-Dependent Electron Transport in Leaves with Inactive Oxygen-Evolving Complexes*. Plant Physiology 149.3 (2009), pp. 1568–1578.
- [Tri90] H.-W. TRISSL, J. BRETON, J. DEPREZ, A. DOBEK and W. LEIBL. *Trapping kinetics, annihilation, and quantum yield in the photosynthetic purple bacterium Rps. viridis as revealed by electric measurement of the primary charge separation*. Biochimica et Biophysica Acta (BBA) - Bioenergetics 1015.2 (1990), pp. 322–333.
- [VJM98] M. H. VOS, M. R. JONES and J.-L. MARTIN. *Vibrational coherence in bacterial reaction centers: spectroscopic characterisation of motions active during primary electron transfer*. Chemical Physics 233.2–3 (1998), pp. 179–190.
- [Vos91] M. H. VOS, J. C. LAMBRY, S. J. ROBLES, D. C. YOVAN, J. BRETON and J. L. MARTIN. *Direct observation of vibrational coherence in bacterial reaction centers using femtosecond absorption spectroscopy*. Proceedings of the National Academy of Sciences 88.20 (1991), pp. 8885–8889.
- [Vos92] M. H. VOS, J. C. LAMBRY, S. J. ROBLES, D. C. YOVAN, J. BRETON and J. L. MARTIN. *Femtosecond spectral evolution of the excited state of bacterial reaction centers at 10 K*. Proceedings of the National Academy of Sciences 89.2 (1992), pp. 613–617.
- [Vos94] M. H. VOS, M. R. JONES, C. N. HUNTER, J. BRETON and J. L. MARTIN. *Coherent nuclear dynamics at room temperature in bacterial reaction centers*. Proceedings of the National Academy of Sciences 91.26 (1994), pp. 12701–12705.

- [Wei09] A. M. WEINER. *Ultrafast optics*. Hoboken, N.J.: Wiley, 2009.
- [Woo85] N. W. WOODBURY, M. BECKER, D. MIDDENDORF and W. W. PARSON. *Picosecond kinetics of the initial photochemical electron-transfer reaction in bacterial photosynthetic reaction centers*. *Biochemistry* 24.26 (1985), pp. 7516–7521.
- [WP87] A. WARSHEL and W. W. PARSON. *Spectroscopic properties of photosynthetic reaction centers. 1. Theory*. *Journal of the American Chemical Society* 109.20 (1987), pp. 6143–6152.
- [WPR97] T. WILHELM, J. PIEL and E. RIEDLE. *Sub-20-fs pulses tunable across the visible from a blue-pumped single-pass noncollinear parametric converter*. *Optics Letters* 22.19 (1997), pp. 1494–1496.
- [Yea88] T. O. YEATES, H. KOMIYA, A. CHIRINO, D. C. REES, J. P. ALLEN and G. FEHER. *Structure of the reaction center from Rhodobacter sphaeroides R-26 and 2.4.1: protein-cofactor (bacteriochlorophyll, bacteriopheophytin, and carotenoid) interactions*. *Proceedings of the National Academy of Sciences* 85.21 (1988), pp. 7993–7997.
- [Zen32] C. ZENER. *Non-Adiabatic Crossing of Energy Levels*. *Proceedings of the Royal Society of London. Series A* 137.833 (1932), pp. 696–702.
- [Zhu13] J. ZHU, I. VAN STOKKUM, L. PAPARELLI, M. JONES and M. GROOT. *Early Bacteriopheophytin Reduction in Charge Separation in Reaction Centers of Rhodobacter sphaeroides*. *Biophysical Journal* 104.11 (2013), pp. 2493–2502.
- [ZZ11] W. ZINTH and U. ZINTH. *Optik: Lichtstrahlen, Wellen, Photonen*. German. München: Oldenbourg, 2011.

Acknowledgment

I would like to express my greatest gratitude to the people who supported me during my work at the chair for *BioMolecular Optics*. I am grateful to:

- **Prof. Dr. Wolfgang Zinth**, for offering me this exciting project together with a very enthusiastic supervision. Without your patience and decidedness it would not have been possible to study the photosynthesis in a comprehensive and systematic manner.
- **Prof. Dr. Richard Cogdell** and **Dr. Alastair Gardiner**, for the preparation of the reaction centers in excellent quality and enough quantity. They also provided me with indications regarding the sample handling and stimulated many steps of this project.
- Former students **Matthias Himmelstoß**, **Jeff Michelmann**, **Johannes Ströbel** and **Florian Lehner**, for taking part in my research and performing a very diligent work.
- **Evelyn Plötz**, for setting up a good basis for my work. I appreciate the improvements you did in our lab *Z21* which I was proud to develop further.
- **Christian Homann**, **Maximilian Bradler** and **Nils Krebs**, for teaching me a lot about non-linear optics.
- **Alexandra Michaelis** and **Marianne Widmann-Diermeier**, for helping me with my duties in the world of german bureaucracy.
- **Rudolf Schwarz**, **Alfons Stork**, **Christian Hausmann** and **Harald Hoppe**, for the very competent work at our technical office. Your fine-mechanic skills could produce most of the mechanical devices present in my experiment.
- My colleagues: **Dominik Bucher**, **Andreas Deeg**, **Franziska Graupner**, **Stefan Hofmann**, **Florian Lederer**, **Lizhe Liu**, **Benjamin März**, **Bert Pilles**, **Michael Rampp**, **Anne Reiner**, **Elena Samoylova** and **Julian Schauseil**, for the nice work environment and honest attitudes. In the many years of working together I could really feel being part of the team.

- **Group of Prof. Riedle**, for their vast support in laser technologies. Without their contribution it would not have been possible to construct such a robust experiment.
- **Group of Prof. Huber**, for their vast help in electronics and bavarian dialect. Special thanks to **Wolfgang Wieser**, **Sebastian Karpf** and **Matthias Eibl** who introduced me into the world of micro-controllers.
- **Karl-Heinz Mantel** and **Florian Trommer**, for their IT-knowledge and their passion for linux systems.
- **Thomas Brust**, **Teja Herzog** and **Gerald Ryseck**, for the nice transition between the old and the new generation.
- Purple bacteria *Rhodobacter sphaeroides*, for having a wonderful photo-synthetic system.
- All my **family and friends**, for their many advices. Even if we are located far away, I could always rely on them.
- My **in-laws**, for accepting me in their family and giving me a large support in my new life.
- And finally: My new family **Carleen Kluger** and **Franka Kluger**, for the best joy of my life.

Lebenslauf

Zur Person

Name	Pablo Nahuel Dominguez
Nationalität	Argentinisch, Italienisch
Geburtstag	1. September 1986
Geburtsort	Mar del Plata
Familienstand	Ledig, 1 Kind

Ausbildung

ab 11/2010	Promotion in Physik Ludwig-Maximilians-Universität München, Deutschland
10/2008 - 07/2010	Elite Master “Theoretical and Mathematical Physics”, Ludwig-Maximilians-Universität München, Deutschland Abschluss mit Master of Science
09/2005 - 07/2008	Bachelorstudium in Physik, Università degli Studi di Pisa, Italien Abschluss mit Bachelor of Science
bis 01/2005	Instituto Industrial Pablo Tavelli, Mar del Plata, Argentinien Allgemeine Hochschulreife mit Schwerpunkt Elektromechanik

Berufserfahrung

08/2010 – 09/2010	SGL Group GmbH, Werner-von-Siemens-Straße 18, 86405 Meitingen, Deutschland
Berufsbezeichnung	Praktikum / Werkstudent
Tätigkeiten	Messung und Auswertung optischer Versuche, Raman Messungen an Kohlenstoffmaterialien

11/2008 – 05/2009 AG Nickel, Lehrstuhl Physik weicher Materie und Biophysik
Ludwig-Maximilians-Universität München, Deutschland

Berufsbezeichnung Werkstudent

Tätigkeiten Programmierung und Auswertung in C und Matlab,
Interpretation von FRAP Messungen

Lehre

Ludwig-Maximilians-Universität München, Deutschland

SoSe 2013 Tutor E4 „Atom und Molekülphysik“

WiSe 2011 Tutor E3 „Experimentelle Optik für Bachelor“

WiSe 2010 Korrektor „Mathematical quantum mechanics“

SoSe 2010 Korrektor „Funktionalanalysis“

WiSe 2009 Tutor T2 „Quantenmechanik für Bachelor“

WiSe 2009 Korrektor „Mathematical quantum mechanics“

SoSe 2009 Tutor T3p „Elektrodynamik für Bachelor plus“

Tagungen

03/2013 Leibniz Universität Hannover, Deutschland
DPG-Frühjahrstagung

03/2010 University of Arizona, USA
„Arizona School of Analysis and Applications“

10/2008 Ludwig-Maximilians-Universität München, Deutschland
„Conformal Field Theory: Introduction and Applications“

Sprachkenntnisse

Spanisch (Muttersprache)
Italienisch (Muttersprache)
Deutsch (fließend)
Englisch (fließend)